UNIVERSITY OF SOUTHAMPTON

FACULTY OF PHYSICAL SCIENCES AND ENGINEERING

Optoelectronics Research Centre

Synthesis and Regeneration of Advanced Optical Modulation Formats

by

Liam Mykel Jones

Supervisor: Dr Periklis Petropoulos

Supervisor: Dr Francesca Parmigiani

Thesis for the degree of Doctor of Philosophy

May 2016

UNIVERSITY OF SOUTHAMPTON

ABSTRACT

FACULTY OF PHYSICAL AND APPLIED SCIENCES

OPTOELECTRONICS RESEARCH CENTRE

Doctor of Philosophy

SYNTHESIS AND REGENERATION OF ADVANCED OPTICAL MODULATION FORMATS

by Liam Mykel Jones

This thesis explores all-optical regeneration techniques for advanced modulation formats with the overall aim of increasing the transmission reach of optical data links. In order to carry out this work, a number of tools were developed for the generation of advanced optical modulation formats. They included a combination of techniques involving the use of a delay line interferometer (DLI), time gating and coherent temporal superposition. A BPSK seed signal was used to generate QPSK (with a single DLI) and 16-QAM (with two concatenated DLIs) signals. The all-optical regeneration schemes studied in this thesis take several forms: phase preserving amplitude regeneration; phase only regeneration; and phase and amplitude regeneration, many of them including PSA configurations as building blocks.

Firstly, phase preserving amplitude regenerators were numerically and/or experimentally investigated. A multilevel amplitude regenerator in a PSA configuration, which was based on parametric pump-saturation, was analysed. A highly nonlinear fibre based dual-pump degenerate scheme was used to effect amplitude regeneration on a 4-level amplitude shift keying signal. Another amplitude regeneration scheme, this time based on optical injection locking, was also experimentally analysed, transmitting a BPSK signal over a 600-km long dark fibre link.

Secondly, a wavelength converting PSA-based phase regenerator for an M-PSK signal was developed by coherently summing the conjugated signal with the $(M-1)^{th}$ phase harmonic, where M is the number of modulated symbols in the signal. This regenerator offers flexibility of operating power and harmonic mixing coefficient. Both numerical and experimental studies prove the feasibility of the proposed scheme. Another proposed regenerator, operating at the gain minima in a PSA configuration and working by coherently summing the signal to the π phase shifted $(M+1)^{th}$ harmonic, offers squeezing in both the amplitude and phase of the input signal. The latter work of this thesis introduces a phase regenerator which is designed to target higher-order M-PSK signals using a (simpler) M/2-PSK PSA-based regenerator.

Contents

List of Figures

List of Tables

Declaration of Authorship

I, Liam Mykel Jones, declare that the thesis entitled *Synthesis and Regeneration of Advanced Optical Modulation Formats* and the work presented in the thesis are both my own, and have been generated by me as the result of my own original research. I confirm that:

- this work was done wholly or mainly while in candidature for a research degree at this University;
- where any part of this thesis has previously been submitted for a degree or any other qualification at this University or any other institution, this has been clearly stated;
- where I have consulted the published work of others, this is always clearly attributed;
- where I have quoted from the work of others, the source is always given. With the exception of such quotations, this thesis is entirely my own work;
- I have acknowledged all main sources of help;
- where the thesis is based on work done by myself jointly with others, I have made clear exactly what was done by others and what I have contributed myself;
- parts of this work have been published as: [See List of Publications]

Signed:.....

Date:.....

Acknowledgements

I would like to thank Prof. Periklis Petropoulos and Dr. Francesca Parmigiani for their continued support and guidance offered throughout my time spent within this PhD journey. Through thick and thin they have managed to offer inspiration to carry on and keep my eye on the prize. I thank you dearly.

I would also like to thank Prof. David Richardson whose kind and intellectual personality offered refreshing insight into many aspects of PhD work and life. What an inspirational character.

To Dr. Victor Rancaño, Dr. Mohamed Ettabib, Dr. Graham Hesketh, Kyle Bottrill and Dr. Radan Slavík for invaluable discussions, friendly advice and many laboratory hours. May your futures be ever rewarding.

Finally, I would like to thank my family for offering many hours of advice and help in keeping my head above water. Much Love.

Nomenclature

Abbreviations

1P	Single Pump
2P	Dual Pump
AOM	Acousto-optic modulator
ASE	Amplified spontaneous emission
ASK	Amplitude Shift Keying
BPSK	Binary Phase Shift Keying
DBPSK	Differential Binary Phase Shift Keying
DLI	Delay Line Interferometer
DPSK	Differential Phase Shift Keying
DQPSK	Differential Quadrature Phase Shift Keying
DS	Dispersion Slope
DSP	Digital Signal Processing
EDFA	Erbium doped fibre amplifier
EOM	Electro-optic modulator
EVM	Error Vector Magnitude
FOPA	Fibre optic parametric amplifier
FSR	Free spectral range
FWHM	Full-width at half-maximum (linewidth)
FWM	Four wave mixing
GVD	Group velocity dispersion
HNLF	Highly nonlinear fibre
IR	Infrared
LP	Linearly polarised (mode)
MLAR	Multi-Level Amplitude Regeneration
NOLM	Nonlinear Optical Loop Mirror
NALM	Nonlinear Amplifying Loop Mirror
NLSE	Nonlinear Schrödinger Equation
NOLM	Nonlinear Optical Loop Mirror
NRZ	Non Return-to-Zero
OIL	Optical Injection Locking
OOK	On-Off Keying

OSNR	Optical Signal to Noise Ratio
OMA	Optical Modulation Analyser
ORC	Optoelectronics Research Centre
OSA	Optical Spectrum Analyser
OTHG	One-third Harmonic Generation
PM	Polarisation Maintaining
PPLN	Periodically Poled Lithium Niobate
PS	Phase Shifter
PSA	Phase Sensitive Amplification or Phase Sensitive Amplifier
PSK	Phase Shift Keying
QAM	Quadrature Amplitude Modulation
QPSK	Quadrature Phase Shift Keying
RK	Runge-Kutta
RZ	Return-to-Zero
SA	Saturable absorber
SBS	Stimulated Brillouin Scattering
SHG	Second harmonic generation
SMF	Single mode fibre
SNR	Signal to Noise Ratio
SOA	Semiconductor Optical Amplifier
SPM	Self-phase modulation
SRS	Simulated Raman Scattering
TE	Transverse electric (mode)
THG	Third harmonic generation
TM	Transverse magnetic (mode)
TLS	Tunable laser source/seed
VOA	Variable Optical Attenuator
XPM	Cross Phase Modulation
ZDW	Zero Dispersion Wavelength

Chapter 1

Introduction

1.1 Research Area and Motivation

Over 3 billion people are estimated to be internet users today and as their internet experience leaves its infancy, their appetite for data increases with their anticipated use of social media (most notably Facebook); Video streaming (Youtube, Netflix); Video conferencing/telephony (Skype); music streaming (Spotify); filesharing (Dropbox) and online video gaming (Blizzard). With the ever increasing social and economic pressures made onto the internet, many countries classify it as a fundamental human necessity and support the expansion and upgrade to their network infrastructures [11]. The demands on the optical communication system to deliver a fast and reliable connection to and from peers positioned on a global scale have never been higher with data traffic speculated to grow by 30-40 % per annum [12]. This growth in data rates over optical communication systems has been made possible thanks to many technological breakthroughs within the last 60 years.

In 1960, the first continuously operating helium-neon gas laser was invented. This immediately sparked speculations about the possibility of using an optical carrier field for telecommunications. This was appealing, because much more information could be modulated onto the optical carrier due to the fact that its frequency is a factor of 100,000 greater than that of microwaves [13].

In 1961 it was observed in Ref. [14] that laser light from a ruby laser could be converted from one colour to another when passed through a crystalline quartz structure, thus marking the inception of nonlinear optics. Nonlinear optics involves the intensity dependent interplay between light and a dielectric material. A dielectric material is an electrical insulator which can be polarised with the application of an electromagnetic field. If the electromagnetic field is intense enough, the dielectric medium will exhibit a nonlinear polarisation response [15]. For example, the intensity dependence of the

refractive index of silica glass causes the exhibition of strong third order nonlinearities, such as self phase modulation (SPM), cross phase modulation (XPM) and four wave mixing (FWM). The control as well as the manipulation of these nonlinear effects became of crucial importance as the distances and speeds involved in optical communication systems evolved in the following few decades.

Much research went into finding an optimal laser source for these new telecommunication systems with the first demonstration of a semiconductor diode laser capable of emitting continuous waves at room temperature in the 1970 [16]. Similarly a vast amount of work went into finding a suitable transmission medium [17]. Key steps towards low-loss transmission media were achieved by the work conducted by Charles Kao within Ref. [18], where he demonstrated that light lost in a glass fibre can be dramatically reduced by removing the impurities from the material. In the same year, 1970, scientists (at Corning Glass Works) found that by doping silica glass with titanium it was possible to make a single mode fibre with attenuation of less than 20dB/km [19]. This immediately attracted attention worldwide with many other laboratories becoming interested in producing low loss fibres. It is definitely fair to say that the telecommunications industry has been revolutionised by the development of such low loss optical fibres alongside the development of narrow linewidth lasers, ushering in the information age.

The subsequent advent of the erbium-doped fibre amplifier (EDFA) allows for the optical amplification of the transmitted signal within the lowest loss region for silica glass at 1550 nm, and has led to a further revolution in optical telecommunications by allowing huge data transfer over inter-continental distances. Indeed the adoption of wavelength division multiplexing (WDM) and the possibility of simultaneous optical amplification of several optical channels in EDFAs permitted data signal rates exceeding 1 Tbit/s within a single fibre to be commercially deployed for high capacity backbone and long haul communications by the late 1990s [20]. The continued growth of the internet traffic has forced the consideration of more spectrally efficient means for transmitting information over an optical fibre. In the last decade or more, optical communications systems have been building on the techniques used by radio-frequency (RF) communication systems, with particular inspiration coming from techniques employed by wireless microwave communication systems. In an environment with ever increasing data traffic the desire to lower the cost of end-to-end networked information bits is of the utmost importance to sustain competitive telecommunication consumer markets [20].

The evolution of optical telecommunications networks has led to transmission speed increase from Mbit/s (in the early 1980s) through to Gbit/s (in the 1990s) to Tbit/s down a single fibre (in the 2000s), Fig. 1.1 displays the capacity of modern multi-core and/or multi-mode systems alongside single mode fibre systems against the transmission length which has been achieved in laboratories. The figure also shows the highest capacity of 2.15 Pbit/s that has recently been achieved using multi-core fibres [21]. Other works

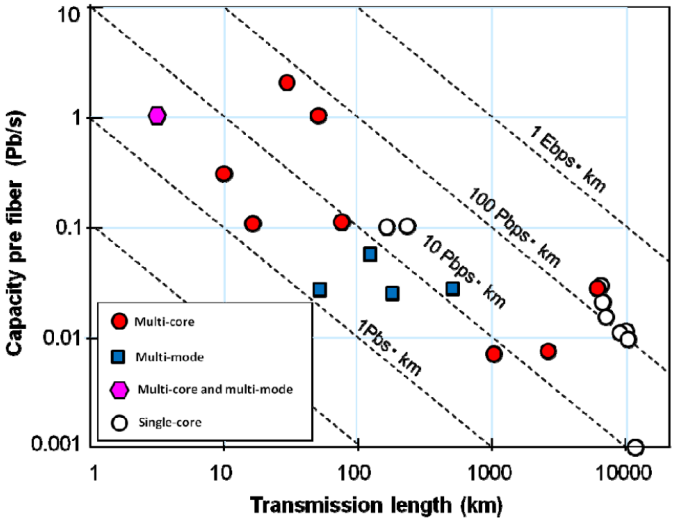

FIGURE 1.1: Capacity and transmission distance of SDM transmission experiments. Adapted from [1]

have demonstrated capacity length products over 100 Pbit/s*km using either single mode or multi-core fibres.

The growth of optical communications has been so expansive, that questions over the ultimate capacity limits of single mode fibre systems and ways to overcome these have become relevant [22].

As the next generation digital communication systems are exploiting the amplitude as well as the phase of the optical carrier in order to maximise the spectral efficiency (SE) and subsequently increase the data rates and fibre capacities [23], a detailed understanding of their nonlinear optical interactions and how they affect fibre communication systems is required.

This thesis focuses on particular aspects of telecom signal synthesis, and their corresponding all optical processing, ensuring high data transferability. Firstly this thesis covers signal degradation (as a means of experimentally introducing controlled amplitude and phase noise), and signal all-optical regeneration (using novel opto-electric methods to optically minimise the effects of noise impairment on the optical signal to noise ratio (OSNR)). Secondly, this thesis highlights linear and nonlinear optical phenomena impeding current telecommunication networks and addresses potential all-optical solutions to increased data throughput of existing fibres by increasing the spectral efficiency of the data modulation formats. The main body of this thesis contains work associated to the design and development of phase sensitive amplifier (PSA) based solutions and their ability to improve optical signal fidelity.

Phase sensitive amplifiers have been well known in the telecommunications research area for many decades and their current implementations within that research area have never been more exciting and full of potential to lead the future of certain niche disciplines of

the optical telecommunications industry, examples of which are highlighted in [2], [24] and [25].

A FWM-based PSA can be implemented in either single or dual pump configuration and in either degenerate or non-degenerate fashion. There are two main types of FWM based PSAs, that can be classified as a 'Modulation Format Transparent' and a 'Modulation Format Specific' PSAs, respectively. The former works on the premise that a conjugated copy of the signal (idler) is created within a phase insensitive amplifier (PIA) before the transmission link (usually referred to as the copier stage). This implementation inherently requires a non-degenerate scheme for the signal facilitating WDM operation, but occupies twice the bandwidth compared to the degenerate counterpart. Since the idler is at a different wavelength, the noise generated within the transmission link is uncorrelated with that of the signal. Such PSA schemes amplify the signal-idler pair which experience a 6 dB higher gain than the uncorrelated noise [26]. On the other hand, the modulation format specific PSAs require the transmission of only the signals. However, for this PSA scheme the modulation format must be known such that the correct idler can be locally generated together with the secondary pump (after the transmission link) within an initial PIA and coherently added to the original signal with the PSA. The final signal has 'squeezed' phase states allowing for phase regeneration.

Within this thesis only modulation format specific PSA regenerators will be considered. It is important to note that this thesis will only contain work related to single wavelength PSA-based regenerators.

1.2 Research Aims

The incentive for this work was to explore methods that have the potential to lighten the burden on electronics in optical communication systems. The potential of high power consuming electronics to be supported or superseded by an all-optical, high speed potentially lower power counterpart, should create a potential for a more power efficient, faster switching network. The most successful example of all-optical solution has been the advent of the EDFA and its implementation in long-haul transmission links to replace single channel optical-electrical-optical (OEO) converters and electrical amplifiers that were used at the time.

This thesis focuses primarily on phase sensitive amplification and is a continuation of the work carried out within the European project "PHase sensitive Amplifier Systems and Optical Regenerator and their applicationS" (PHASORS). The latter part of the work within this thesis has been part of the EPSRC project "Transforming the Internet Infrastructure: The Photonics HyperHighway".

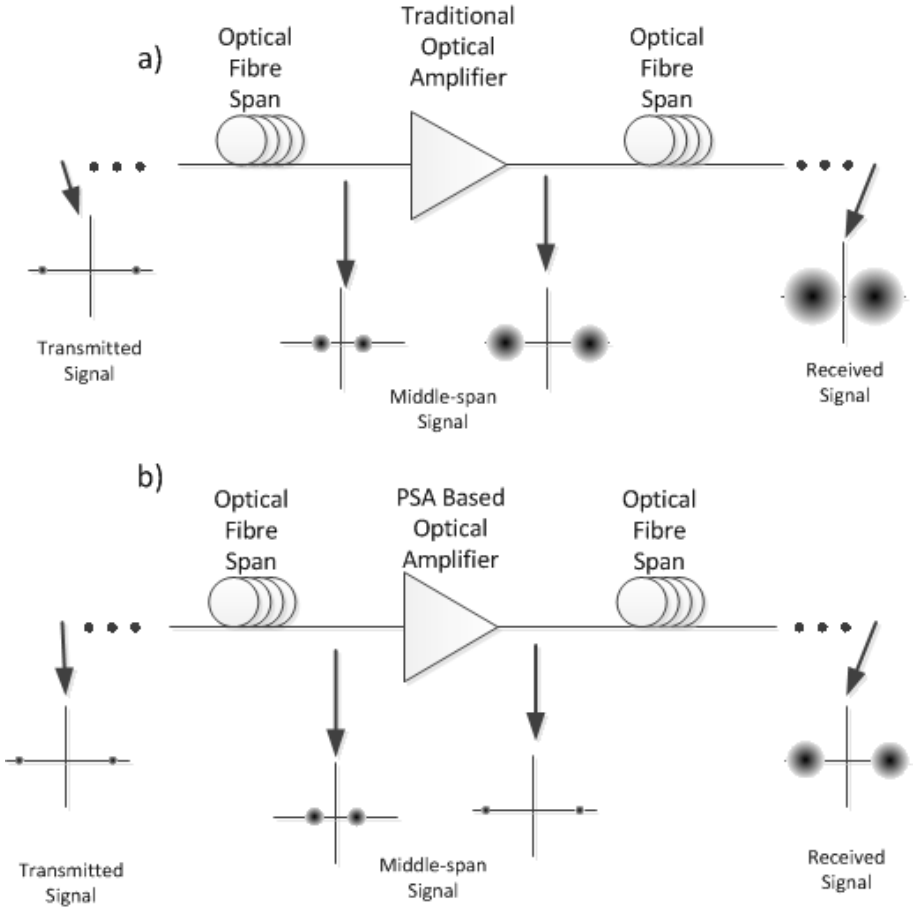

FIGURE 1.2: Conceptual scheme of a) a traditional optical amplifier vs b) a PSA based optical amplifier, with eye diagrams

Fig. 1.2 a) displays a conceptual diagram containing optical fibre links consisting of traditional optical amplifiers (such as EDFAs). Here the noise accumulated by the optical fibre spans is amplified alongside the signal. With the addition of further fibre spans the receiver at the very end of the link has to cope with accumulated noise. However if the traditional EDFAs are to be replaced by PSA-based optical amplifiers, the signals can be amplified, while at the same time regenerated, as displayed in Fig. 1.2 b) for the case of a binary phase shift keying (BPSK) signal. In this way the noise accumulated on the first part of the optical fibre span can be removed in the PSA-based amplifier such that the final signal can be properly received at the end of the link.

Below are the main results achieved during the course of this study:

- A demonstration of all-optical modulation format conversion and packet compression of signals from BPSK to 16-QAM. A method consisting of accurate time gating and coherent temporal superposition are used to achieve the packet compressed format converted signals [27]. I helped with the laboratory experimentation, where Dr. Francesca Parmigiani was the lead author.

- A demonstration of an all-optical broadband phase noise emulation which was used to generate noise in a PSA experiment consisting of a novel W-type lead silicate fibre. The broadband phase noise was generated from a novel all-optical XPM induced phase noise emulator, and applied to a DPSK signal [28].

- A demonstration of phase preserving amplitude regeneration using an optical injection locked scheme. This was demonstrated in a 600 km installed fibre link. The phase to amplitude noise redistribution of a 10Gbit/s BPSK signal was analysed [29].

- A proposition and demonstration of a novel wavelength converting phase regenerator was conducted. This regenerator operates on the principle of coherently summing the wavelength converted conjugated signal with that of the signals $(M-1)^{th}$ phase harmonic (where M is the number of symbols used within the signal). A secondary pump is in place (at the M^{th} phase harmonic) at the input to quantify the harmonic mixing coefficient, 'm'.

- A demonstration of simultaneous phase and amplitude regeneration. This regenerator works on the principle of coherently summing the π phase shifted $(M+1)^{th}$ phase harmonic with that of the original signal.

- A demonstration of a numerical study that investigates a phase regeneration technique that allows on M-PSK signal to be regenerated by using M/2-PSK (or even M/4-PSK) phase regenerator. This scheme offers an interesting method to overcome the problems inherent with today's PSA based phase regenerators. By partially regenerating (using lower pump powers and achieving a less pronounced phase transfer function plateaus) the second harmonic (or nested second harmonic) the burden to generate such high harmonics has been lifted in place of more intelligent regenerator designs [30].

1.3 Outline

In Chapter 2 a brief introduction into the classical theory of optical field propagation within a dielectric medium is described. Effects such as chromatic and polarisation mode dispersion are discussed together with various third order non-linearities. Elastic and inelastic scattering mechanisms are discussed together with their relevance to the research within other chapters of this thesis. Parametric amplification is analytically discussed with a bias placed on explaining the operating principle and benefits of phase sensitive amplification. Finally, the solution of the nonlinear Schrödinger equation is described.

Chapter 3 introduces a few techniques used within the laboratory to emulate higher order modulation formatted signals. An opto-electronic feedback stabilisation system

is designed and tested to control the delay line interferometers used within the signal emulation system. Next, a method to convert the modulation format and packet compress the size of the optical packets is investigated which encompasses much of the work within the QPSK and 16-QAM emulation sections, however, with the added complexity of time gating and coherent temporal superposition. Finally, an all-optical broadband phase noise emulation technique is experimentally investigated and applied to a PSA based experiment.

Chapter 4 includes work on phase preserving amplitude regenerators. Firstly, a multi-level amplitude regenerator based on parametric pump-saturation is analysed. A highly nonlinear fibre (HNLF) based dual-pump degenerate scheme is used to try and perform phase preserving amplitude regeneration on a 4 level amplitude shift keying signal (4-ASK). Secondly, amplitude regeneration based on optical injection locking (OIL) is analysed, whereby a binary phase shift keying (BPSK) signal is transmitted over a 600 km dark fibre link. The returned signal is then regenerated using OIL. This experiment displayed a reduction in root mean squared (rms) amplitude error by a factor of 2.4, while only exhibiting a rms phase error deterioration of 1.1. A 1 dB receiver sensitivity improvement, at a BER of $1x10^{-4}$, was achieved with the use of optical injection locking.

Chapter 5 offers a look into the applications of regenerators using high-order harmonics. Two different regenerators are analysed, the first is a wavelength converting phase only regenerator, and works by coherently summing the conjugated signal with the $(M-1)^{th}$ harmonic, where M is the number of modulated symbols in the signal. It is worth mentioning that in traditional PSA, the coherent addition between the signal and the conjugated $(M-1)^{th}$ harmonic happens at the signal wavelength. The new proposed regenerator is notable for its ease of tunability and flexible operating power. However, the regenerated output field is wavelength converted to the wavelength of the $(M-1)^{th}$ harmonic.

The second regenerator is a phase and amplitude regenerator and works by coherently summing the π phase shifted $(M+1)^{th}$ harmonic. This regenerator operates at the gain minima for a PSA and offers squeezing in both the amplitude and phase of the input signal.

Chapter 6 introduces a novel PSA based phase regeneration of high-order M-PSK signal. Here a three stage process is used to firstly produce the second and third harmonics; secondly, partially regenerate the second harmonic; and lastly, use FWM to regenerate the original signal. The benefit of this is that the regeneration process only needs occur on a lower level (usually M/2-PSK) signal. Furthermore this work highlights the technical challenges with overcoming phase locking drift associated with long lengths of HNLF. For this work to be achieved within a laboratory based experiment significant advances in nonlinear waveguide technologies have to take place.

Finally Chapter 7 offers a conclusion to the work completed within this thesis and the possible areas of research that could follow this work.

Chapter 2

Background

2.1 Introduction

This chapter covers a brief introduction to the classical theory of optical field propagation within a dielectric medium within the context of signal propagation through an optical fibre. In particular, chromatic and polarisation mode dispersion, together with descriptions of various third order nonlinearities will be discussed. Elastic and inelastic scattering mechanisms are mentioned, alongside their relevance to this research project. Parametric amplification, which is the basis for most of the experimental work described in this thesis, is discussed with close attention to phase sensitive amplification. Properties of phase sensitive amplifiers (PSAs) in terms of phase regeneration are discussed. The nonlinear Schrödinger equation is introduced alongside a method to deliver its solution, the split step Fourier method. This was used to perform numerical simulations of various parametric devices analysed in the following chapters.

2.2 Wave propagation effects in optical fibre

The induced polarisation, P, of a dielectric medium can be defined as the dipole moment per unit volume, where ϵ_0 represents the vacuum permittivity. If the polarisation is expanded using a power series in the applied electric field Eq. (2.1) can be formulated: [15]

$$P = \epsilon_0 \left(\chi^{(1)} \cdot E + \chi^{(2)} : EE + \chi^{(3)} \vdots EEE + \cdots \right) \tag{2.1}$$

Where $\chi^{(1)}$ is the linear susceptibility which relates to the frequency dependent refractive index, $n(\omega)$, and material attenuation, $\alpha(\omega)$, $\chi^{(2)}$ and $\chi^{(3)}$ are the nonlinear susceptibilities of the second and third order. The frequency dependent refractive index term can

be understood as the factor by which the propagating optical field velocity is decreased relative to the velocity of light in a vacuum.

Fibres typically have longitudinal inversion symmetric structures, thus the $\chi^{(2)}$ susceptibility is almost negligible with only a small term relating to the electric-quadrupole and magnetic dipole moments which have the ability to generate weak second-order nonlinear effects [15].

2.3 Generalised Non-Linear Schrödinger Equation (NLSE)

Generally speaking the NLSE is a universal nonlinear model that can be used to describe many physical nonlinear systems. The generalised NLSE describes how an Electromagnetic field propagates longitudinally through a fibre whilst being affected by the fibre attenuation, α, the second and third order dispersion, β_2 and β_3 respectively, and the nonlinear coefficient, γ.

$$\frac{\delta A}{\delta z}(z,T) = -\frac{\alpha}{2}A(z,T) - i\frac{\beta_2\delta^2 A}{2\delta T^2}(z,T) + \frac{\beta_3\delta^3 A}{6\delta T^3}(z,T) + i\gamma|A(z,T)|^2A(z,T) \tag{2.2}$$

Here A is slowly varying envelope of the electric field and T represents a time frame of reference related to the physical time t through $T = t - \frac{z}{v_g}$, where v_g is the group velocity, thus allowing us to neglect the β_1 term. $\beta(\omega)$ is expanded about the fundamental frequency of the wave, ω, which will be further explained in Section 2.3.2. The terms relating to self-steepening and Raman gain are neglected from Eq. 2.2 as these terms will not be relevant for the work conducted within this thesis. The first three terms on the right hand side (RHS) contain a linear representation of the optical field ($A(z,t)$), whereas the fourth term on the RHS, containing the nonlinear coefficient, is nonlinear due to the cubic representation of the optical field [15]. The NLSE can be solved numerically by using the Split step Fourier transform method that will be discussed in section 2.6.

2.3.1 Fibre losses

An important fibre parameter to consider is the loss coefficient (first term on the RHS of the NLSE) of the fibre (α). This parameter can quantify the reduction on the power of the propagating waveform whilst travelling through the optical fibre. If P_0 is the power launched into the fibre, of length L, the power seen at the output, P_T, is given by;

$$P_T = P_0 e^{-\alpha_{LIN}L} \tag{2.3}$$

Where α_{LIN} has units of $(km)^{-1}$. Eq.(2.4) links this coefficient with that of its logarithmic united counterpart.

$$\alpha_{dB} = -\frac{10}{L}\log\left(\frac{P_T}{P_0}\right) = 4.343\alpha_{LIN} \tag{2.4}$$

Where α_{dB} has units of dB/km. The dB/km units are most common for describing attenuation in an optical fibre and a typical value for current low loss commercially available optical fibres is around 0.2 dB/km [31].

2.3.2 Chromatic dispersion

Chromatic dispersion is an effect originating from the frequency dependence of the refractive index of light in a dielectric medium. A time varying electromagnetic field propagating in the z (longitudinal) direction, $E(z,t)$, can be mathematically represented in [15] Eq. (2.5):

$$E(z,t) = \frac{1}{2}[A(z,t)e^{i(\omega t-\beta z)} + c.c] \tag{2.5}$$

Where $A(z,t)$ represents the envelope of the waveform, ω represents the angular frequency of the carrier, β is the propagation constant or wavevector number which represents the change in spectral phase per unit length and c.c. is an abbreviation for complex conjugate. For chromatic dispersion of higher orders it is necessary to perform a Taylor's expansion of the propagation constant about a reference angular frequency ω_0. Thus giving Eq. (2.6):

$$\beta(\omega) = n(\omega)\frac{\omega}{c} = \beta_0 + \beta_1(\omega-\omega_0) + \frac{\beta_2}{2}(\omega-\omega_0)^2 + \frac{\beta_3}{6}(\omega-\omega_0)^3 + \frac{\beta_4}{24}(\omega-\omega_0)^4\ldots \tag{2.6}$$

Where c represents the speed of light in a vacuum. The zero order term, β_0, describes a common phase shift. The first order term, β_1, contains the inverse group velocity (or group delay per unit length) such that:

$$v_g = \frac{d\omega}{d\beta} = \frac{1}{\beta_1} \tag{2.7}$$

The parameter β_2 is often referred to as the group velocity dispersion (GVD) coefficient. A more common fibre dispersion parameter is used in fibre characterisation, which is dispersion (D), and relates to β_2 as follows:

$$D = -\frac{2\pi c}{\lambda^2}\beta_2 \tag{2.8}$$

Typically there is another important fibre parameter which relates to the wavelength at which the GVD coefficient (β_2) vanishes. This is called the zero dispersion wavelength (λ_{ZDW}). There is an increasing interest within some fibre manufacturers to be able to shift the ZDW to selected telecoms wavelengths (such as 1550nm) to increase nonlinear

interactions for applications involving all-optical switches/devices. This can be achieved through fibre core doping alongside waveguide engineering such that the waveguide contribution to the β_2 negates the fibre's material dispersion [32]. On the other hand, Corning's SMF-28 (widely used telecommunications single mode fibre) has a ZDW in the region between 1300 nm and 1320 nm [33]. This implies that the waveguide contribution to the fibre dispersion is minimal (the fibre's ZDW coincides with that of silica), and is made so to ensure that nonlinear effects in transmission at 1550 nm are minimised. Conventionally, a fibre is said to exhibit normal dispersion when $\beta_2 > 0 (D < 0)$ and anomalous dispersion when $\beta_2 < 0 (D > 0)$.

The third order dispersion term (β_3) can be considered as the rate of change of β_2 with respect to its frequency components. Again a more common fibre dispersion parameter is used in fibre characterisation, which is the dispersion slope (DS), and relates to β_3 as follows:

$$DS = -\frac{2\pi c}{\lambda^3}\left[\frac{2\pi c \beta_3}{\lambda} + 2\beta_2\right] \tag{2.9}$$

Higher order dispersion terms can usually be neglected due to their insignificant proportion in relation to prior order dispersion terms.

2.3.3 Polarisation mode dispersion

Random imperfections and asymmetries within optical fibre can cause the stochastic spreading of optical pulses within two different polarisations of light. Fibres that exhibit birefringence will have a refractive index differential between orthogonal polarisation states. This differential will cause pulses propagating within a fibre at two different polarisation states to incur differing delays. The fibres used in modern day optical communication systems have been specially designed to substantially reduce the effects of PMD. This phenomenon occurs as a result of variable propagation characteristics in relation to the polarisation of the incident optical fields. PMD can lead to some level of pulse broadening which in turn can lead to inter symbol interference (ISI) and increase the bit error ratio. PMD can be subject to the longitudinal bend of the fibre, temperature fluctuations or any mechanical stress induced on the fibre, which all affect the birefringence of the fibre. This is important to understand when conducting laboratory work [34]. To completely nullify the effects of PMD a fibre type that, once aligned, can maintain the state of polarisation on the optical fields along its length is necessary. These fibres are aptly named polarisation maintaining (PM) fibres. PM fibres are achieved by straining the fibres'core axially throughout its length by introducing stress elements made from different types of glass, positioned at opposite ends of the fibre core (considering cross-sectional appearance) [35]. These stress elements introduce two orthogonal fundamental polarisation mode components (fast-axis and slow-axis) which

experience different propagation constants. The first demonstration of PM fibres was in 1981 [36]. PM fibres are desirable, or even necessary in certain applications, due to their inherent polarisation stability. This stability is often utilised for the generation of nonlinear effects, most notably four-wave mixing since co-polarisation between incident optical fields can be achieved and maintained more easily.

2.3.4 Nonlinear refraction

Due to the high transversal confinement that the fibre core has on the electric field it is possible for the intensity (power per unit area) to reach very high values (up to MW/cm^2). At these high optical intensity values the refractive index of the fibre is affected by the presence of the optical field through the optical Kerr effect. The nonlinear refraction is expressed in Eq. (2.10):

$$n(I) = n_0 + n_2 I \tag{2.10}$$

Where n_0 is the linear refractive index, n_2 is the nonlinear refractive index, and I is the local intensity of the electrical field [15]. The intensity induced refractive index change can manifest as a fluctuation in the signal's optical phase as a result of the optical Kerr effect, shown in Eq. 2.11.

$$\phi = (n_0 + n_2 I)\frac{2\pi L}{\lambda} \tag{2.11}$$

Where L is the length of the fibre and λ is the wavelength of the light. The intensity dependence of the refractive index is responsible for nonlinear phenomena, such as self-phase modulation (SPM) and cross phase modulation (XPM), described in the following subsections [15]. The nonlinear coefficient is a function of the nonlinear refractive index and the effective modal propagation area (A_{eff}), and is described in Eq. (2.12):

$$\gamma = \frac{2\pi n_2}{\lambda A_{eff}} \tag{2.12}$$

Eq. (2.10) highlights the importance of the electric field intensity within the fibre to induce the Kerr effect, similar relationships between the intensity and induced scattering can be made, one such scattering mechanism is Stimulated Brillouin Scattering (SBS), as will be discussed in Section 2.5.2. Its significance to our laboratory work will become evident later in the thesis.

2.3.4.1 Self phase modulation (SPM)

The propagating electric field can experience a nonlinear phase shift induced by its own power which can be quantified as: [15]

$$\phi_{SPM}(t) = \gamma P(t) L_{eff} \tag{2.13}$$

Here L_{eff} is the effective length of the interaction region and takes into account the losses of the fibre such that $L_{eff} = \frac{1-e^{\alpha_{LIN}L}}{\alpha_{LIN}}$. $P(t)$ is the instantaneous power of the optical field. In standard single mode fibre (SSMF) a complete phase reversal can be achieved when the power length product is in the order of 1Wkm [37].

2.3.4.2 Cross phase modulation (XPM)

Two co-propagating and temporally overlapping optical fields, of sufficiently high intensities, will also induce an intensity dependent refractive index change of the Kerr medium (fibre). The corresponding nonlinear phase shift is expressed in Eq. (2.14):

$$\phi_{XPM}(t) = \widehat{\kappa}\gamma P(t) L_{eff} \tag{2.14}$$

Where $\widehat{\kappa}$ is a polarisation dependant coefficient which is 2 for linearly co-polarised optical fields and 2/3 for orthogonally polarised optical fields. $P(t)$ is the instantaneous power of the incident optical field. XPM has been used for many different applications including all-optical switching [38] and retiming applications [39].

2.4 Parametric Amplification

2.4.1 Four wave mixing

If two waves of frequencies ω_1 and ω_2, with $\omega_2 > \omega_1$, interact inside a nonlinear medium (such as a highly nonlinear fibre, HNLF), a refractive index modulation at the difference frequency $\Delta\omega = \omega_2 - \omega_1$ occurs, generating new frequency sidebands at frequencies $\omega_3 = \omega_1 - \Delta\omega = 2\omega_1 - \omega_2$ and $\omega_4 = \omega_2 + \Delta\omega = 2\omega_2 - \omega_1$. The generation of these new frequency components must adhere to the conservation of net energy and angular momentum within the system, such that $\omega_1 + \omega_2 = \omega_3 + \omega_4$ and $\phi_1 + \phi_2 = \phi_3 + \phi_4$ where ω_j and ϕ_j are the angular frequency and phase respectively of wave j, with j=1,..4. If a pre-existing wave is present at the input of the system and is at the frequency ω_3 or ω_4 then parametric amplification will occur. Four coupled differential equations can be used to describe the power flow of the pumps, signal and idler; the corresponding solutions for a generic pump degenerate configuration ($\omega_1 = \omega_2$), as displayed in Fig. 2.1 [40, 41, 42] are described as follows:

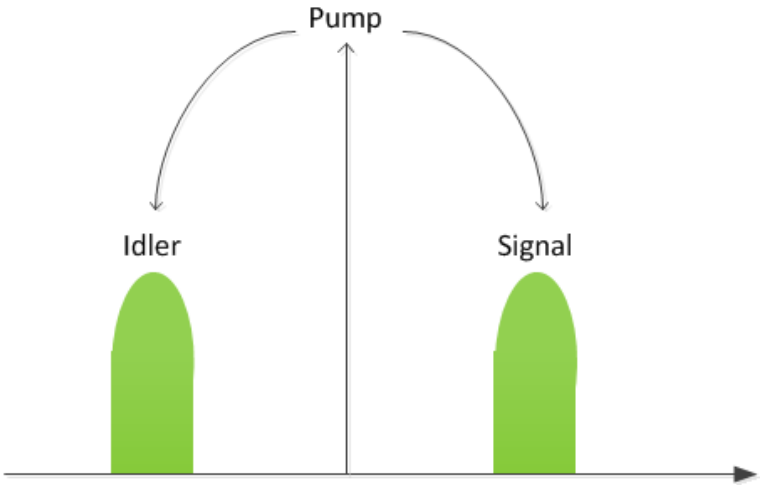

FIGURE 2.1: Pump degenerate FWM pumping scheme.

$$\begin{aligned}
\frac{dP_p}{dz} &= -\alpha P_p - 4\gamma\sqrt{(P_p^2 P_s P_i)}\sin\theta \\
\frac{dP_s}{dz} &= -\alpha P_s + 2\gamma\sqrt{(P_p^2 P_s P_i)}\sin\theta \\
\frac{dP_i}{dz} &= -\alpha P_i + 2\gamma\sqrt{(P_p^2 P_s P_i)}\sin\theta \\
\frac{d\theta}{dz} &= \Delta\beta + \gamma\left(2P_p - P_s - P_i + \left[\sqrt{\left(\frac{P_p^2 P_s}{P_i}\right)} + \sqrt{\left(\frac{P_p^2 P_i}{P_s}\right)} - 4\sqrt{(P_s P_i)}\right]\cos\theta\right)
\end{aligned} \tag{2.15}$$

Where P_p, P_s and P_i are the optical powers of the pump, signal and idler, respectively. The overall relative phase, $(\theta(z))$, can be described as:

$$\theta(z) = \phi_s(z) + \phi_i(z) - 2\phi_p(z) \tag{2.16}$$

Where ϕ_s, ϕ_i, ϕ_p are the phases of the signal, idler and pump, respectively.

The total phase mismatch term, $\Delta\beta$, is defined as:

$$\kappa = \Delta\beta = \Delta\beta_L + \Delta\beta_{NL} \tag{2.17}$$

Where,

$$\Delta\beta_L = \beta_s + \beta_i - 2\beta_p \tag{2.18}$$

Which is described as the linear phase mismatch per unit length, attributed to the dispersion of the fibre, between the signal (β_s), idler (β_i) and pump (β_p). Whereas $(\Delta\beta_{NL})$ is the nonlinear phase mismatch, which can be attributed to nonlinear pump

induced XPM, and can be defined as,

$$\Delta\beta_{NL} = 2\gamma P_p \tag{2.19}$$

where P_p is the pump(s) power. The relative phase contributions of the signal, idler and pump after propagating down the fibre can be termed together with the introduction of the phase mismatch term. Now considering the initial launched optical fields, the relative phase between the signal, idler and pump phases can be defined as follows in Eqs. (2.20)(2.21),

$$\theta(z) = \Delta\beta z + \phi_s(0) + \phi_i(0) - 2\phi_p(0) \tag{2.20}$$

Expanding to

$$\theta(z) = (\Delta\beta_L + \Delta\beta_{NL})z + \phi_s(0) + \phi_i(0) - 2\phi_p(0) \tag{2.21}$$

This relative phase is shown to vary linearly with propagation distance by a rate determined by the total phase mismatch ($\Delta\beta$). To create an effective fibre optic parametric amplifier (FOPA) the total phase mismatch will need to be minimised and the signal gain maximised. If $\theta(z) > 0$ the energy transfer is from the pump(s) to the signal-idler pair, whereas if $\theta(z) < 0$ the energy transfer is from the signal-idler pair to the pump(s). This offers the ability to create an amplifier which has a gain dependence on the input signal phase. This amplifier is called a PSA.

2.4.2 Fibre optic parametric amplification gain characterisation

This subsection will extend the solution found in Eq. 2.15 to fit the analytical solution to the generic non degenerate dual pump FWM-based configuration shown in Fig. 2.2. This includes the assumption that pump depletion is not considered since the launched Signal and Idler powers are usually much smaller than those of the Pumps, hence $P_{1,2}(z) = P_{1,2}(0)$, where subscripts 1 and 2 refer to Pump 1 and 2 respectively. The pump power, P_p can be replaced with the two individual pumps, P_1 and P_2, where their sum is given by $P_0 = P_1 + P_2$. Here the electric fields of the pumps will be defined as A_1 and A_2 for pumps 1 and 2 respectively and A_s and A_i of the signal and idler fields respectively.

The parametric gain coefficient is defined as $g = \sqrt{r^2 - \left(\frac{\kappa}{2}\right)^2}$, where $r = 2\gamma A_1 A_2$ is the FWM coupling coefficient, and $\kappa = \Delta\beta$ as shown in Eq. (2.17). The gain of the signal at the end of the fibre of length L can be derived as follows [42]:

$$h_3(L) = \frac{A_s(L)}{A_s(0)} = \left[\cosh(gL) + i\frac{\kappa}{2g}\sinh(gL)\right] e^{i\left(2\gamma P_0 - \frac{\kappa}{2}\right)L} \tag{2.22}$$

Initially assuming that there is no idler field launched into the fibre, the gain of the idler is expressed by:

$$h_4(L) = \frac{A_i(L)}{A_s^*(0)} = i\frac{r}{g}\sinh(gL)e^{i\left(2\gamma P_0 - \frac{\kappa}{2}\right)L} \tag{2.23}$$

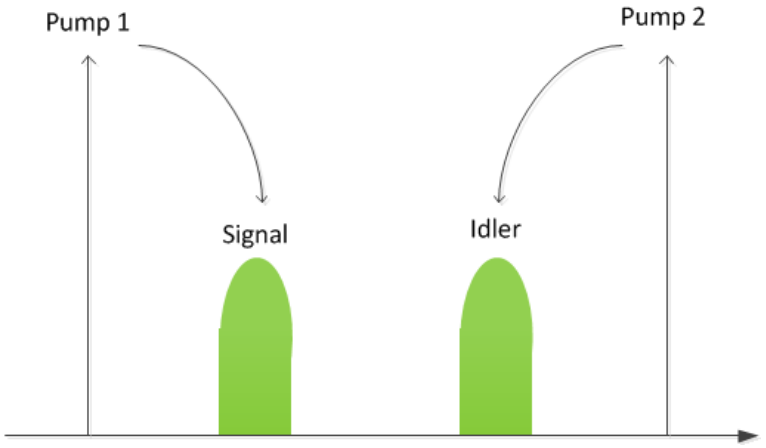

FIGURE 2.2: Non-degenerate dual pump FWM pumping scheme.

The signal-to-idler conversion efficiency $G_i(L) = |h_4(L)|^2$ is solved to

$$G_i(L) = \left| \frac{r}{L} \sinh(Lz) \right|^2 \tag{2.24}$$

The signal power gain $G_s(L) = |h_3(L)|^2$ is related to $G_i(L)$ through

$$G_s(L) = G_i(L) + 1 \tag{2.25}$$

The maximum value that the parametric gain coefficient, g, can take is equal to the FWM coupling coefficient, r. In this case, it can be calculated that $G_s(L)$ and $G_i(L)$ are approximately equal and when the gain values are large their value is:

$$G_s(L)_{max} \approx G_i(L)_{max} \approx \frac{e^{2rL}}{4} \tag{2.26}$$

Represented in decibels is

$$G_s(L)^{dB}_{max} \approx G_i(L)^{dB}_{max} \approx 8.64\gamma P_0 L - 6 \tag{2.27}$$

Where $\gamma P_0 L$ is the pump nonlinear phase shift which resembles Eq. (2.14). This analytical solution allows us to quickly estimate the maximum gain of the FOPA (i.e. under conditions when $\kappa = 0$)if the relevant fibre parameters are known.

2.4.3 Phase sensitive amplification

Generally speaking amplification is needed to overcome physical limitations of the optical fibre link, most notably signal attenuation. This subsection will explain diagrammatically the concept of phase sensitive amplification. When a signal and pump field are launched into the input of a HNLF, the gain experienced by the signal is independent

of the relative phase between the incident signal and pump. This is termed phase insensitive amplifier (PIA). However, when the pump, signal and idler fields are input into a HNLF, Eq. (2.15) show how the power flow depends on the relative phase between the three incident fields. Parametric amplification occurs when the relative phase satisfies ($\theta = \pi/2$), here the pump gives power to the signal and idler. Conversely, parametric de-amplification occurs when the relative phase satisfies ($\theta = -\pi/2$), here the signal and idler fields give power to the pump. Amplification of a coherent signal can be represented diagrammatically as separate amplification of that signal in the in-phase axis and in the quadrature-phase axis. If we consider that the PSA's amplification axis is equal to the in phase axis a PSA will amplify a signal in the in-phase axis but deamplify the signal in the quadrature axis. Fig. 2.3 displays the amplification process of both a PIA (A) and PSA (B), including the constructive and destructive interference equations (C). PSAs use the coherent addition of a conjugated (or unconjugated) phase harmonic to effectively 'squeeze' the phase of the output optical field. The coherent addition of the phase conjugated first harmonic will result in a PSA configuration as shown in Fig. 2.3 b). However it is possible to realise more complex (higher order) PSAs which have more 'squeeze' axes by coherently adding a conjugated $(M-1)^{th}$ harmonic, where M/2 is the number of 'squeeze' axes. In general the potential advantages of PSAs include, noise reduction, the reduction of noise-induced frequency and phase fluctuations and the suppression of modulation instability [43].

2.5 Inelastic Scattering Effects

2.5.1 Simulated Raman scattering (SRS)

The non-instantaneous nonlinear response of an optical medium to an optical field can produce an inelastic scattering mechanism called SRS. In the case of SRS this non-instantaneous response is caused by high frequency vibrational modes in the glass lattice structure of the transmission medium associated to optical phonons. The scattered light is down-shifted by the energy of the optical phonon, which in silica glass result in a frequency shift typically of 13 THz while the molecules of the transmission medium make transition to a higher energy vibrational state [15]. Raman effects will largely be ignored during the analytical work presented in this thesis as the powers used are generally much lower than the Raman threshold [44].

2.5.2 Stimulated Brillouin scattering (SBS)

In principle SBS is created through interactions between the incident pump field and acoustic waves. The pump field generates acoustic waves through the process of electrostriction (electric field induced fibre structure distortions). The acoustic waves cause

a modulation of the refractive index of the fibre. These fluctuations in the refractive index generate a Bragg diffraction grating. The back scattered light is frequency down-shifted from the pump field (by an amount of approximately 10 GHz, typically) as a result of the diffraction grating propagating at the acoustic wave velocity (Doppler shift), in the same direction as the pump field. The Doppler Effect downshifts the energy of the incident light, translating it to a back scattered wave with a higher wavelength. SBS effects become apparent when the SBS backscattering power becomes larger than the

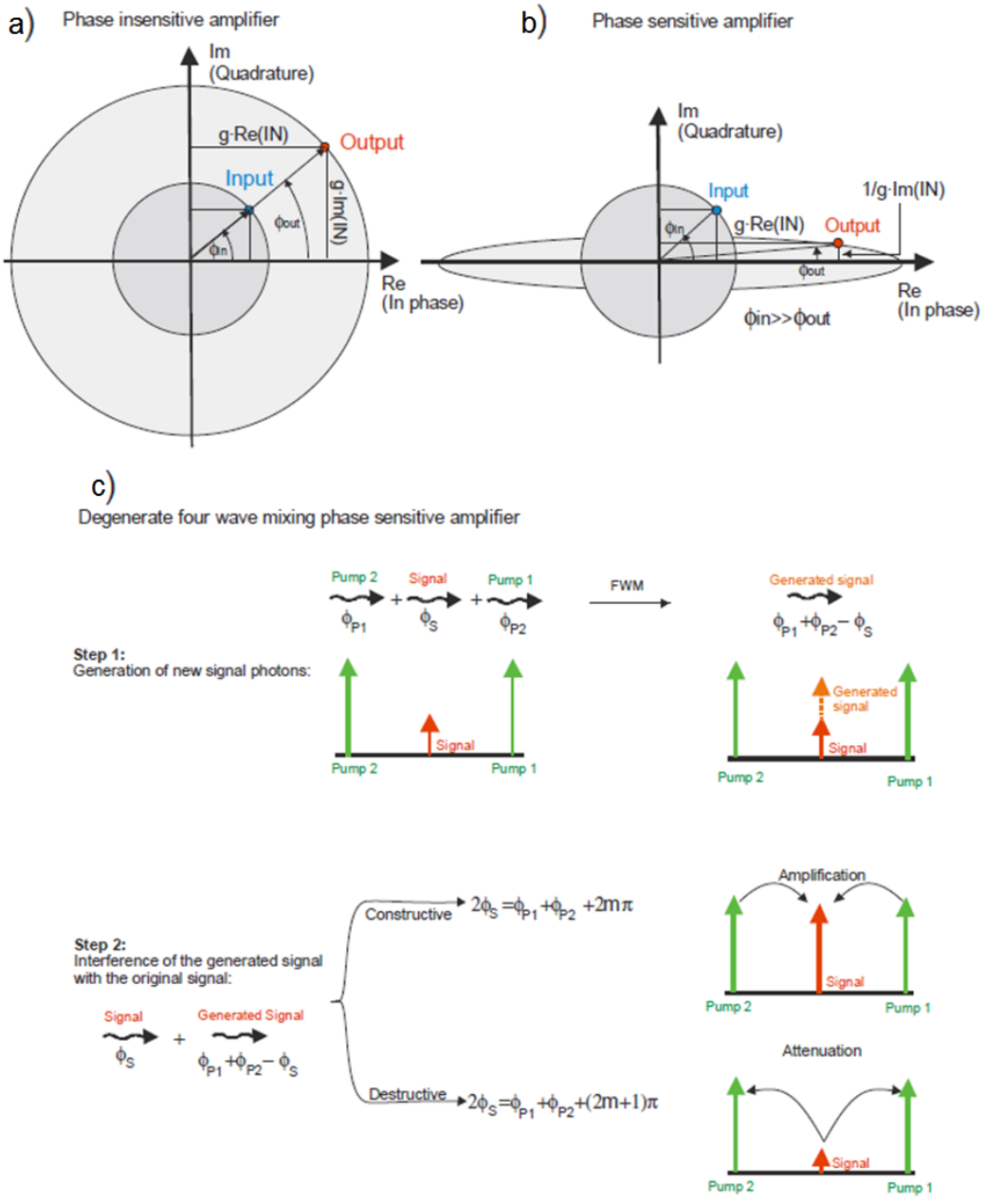

FIGURE 2.3: Subfigure a) Shows the phase-amplitude space representation of the amplification of a PIA, whereas subfigure b) displays the alternative amplification characteristics of a PSA. Here, the output phase has been squeezed to the In-phase axis. c) Diagrammatically explains the relative phase sensitive (de)amplification introduced at the end of section 2.4.1. Taken from [2]

spontaneous Rayleigh backscattering [45]. SBS is a problem within the telecommunications industry, when dealing with narrow linewidth input signals. SBS effectively limits the amount of power that can be launched into a fibre. In the context of parametric amplifiers the problem arises when the required power (of the pump(s), typically) is higher than the SBS threshold of the fibre. There are two main methods to alleviating the effects of SBS. Firstly, increasing the spectral width of the signal under test to an amount greater than the typical SBS bandwidth which is of the order of 10 MHz, through data modulation or other means, alleviates a lot of the issues with SBS as its bandwidth is of the order of 50-100 MHz. Secondly, the fibre itself can be linearly strained which can cause a longitudinal variation in the fibre parameters that increase the SBS threshold or different dopants can be used to increase the SBS threshold.

2.6 Split-Step Fourier Method

The NLSE can be solved numerically using the Split-Step Fourier Method (SS-FM). The propagating electric field described in the NLSE can be solved by using calculations of short step size such that the linear and nonlinear terms can be independently approximated. Eq. 2.2 can be re-expressed in the form:

$$\frac{\delta}{\delta z}A(z,t) = [D+N]A(z,t) \tag{2.28}$$

Where $D = \left(-\frac{\alpha}{2} - i\frac{\beta_2\delta^2}{2\delta^2} + \frac{\beta_3\delta^3}{6\delta^3}\right)$ and $N = \left(i\gamma|A(z,T)|^2\right)$ are the dispersive and nonlinear operators, respectively. The longitudinal distance of the fibre is split into small discrete evenly spaced steps. For each sequential step only one part of the NLSE is solved at a time dealing with the dispersive and nonlinear terms sequentially. Each step is solved with complete independence from the other steps. The nonlinear portion of the NLSE is solved in the temporal domain whereas the linear portion of the NLSE is solved in the spectral domain. A Fourier transform is used to convert the NLSE from one domain to the other which can be implemented for example, using a fast-Fourier transform algorithm in Matlab® that has a faster resolving time than conventional Fourier transform algorithms. Firstly the nonlinear contribution to the NLSE is solved for the first step (longitudinally through the fibre) whist the linear contribution is ignored. Before the second iteration, the result to the first step is Fourier transformed to convert it into the spectral domain. Here the nonlinear contribution is ignored and the linear contribution is solved. Then, before the process repeats itself the result to the second step undergoes an inverse Fourier transform bringing the result back into the temporal domain. There is a good reason that the two contributions are computed in the spectral and temporal domain separately. A Fourier transform of a time derivative can be solved arithmetically, i.e. the Fourier transform can be simplified to an integral (summation of points between two limits) with the result being able to be multiplied by a frequency

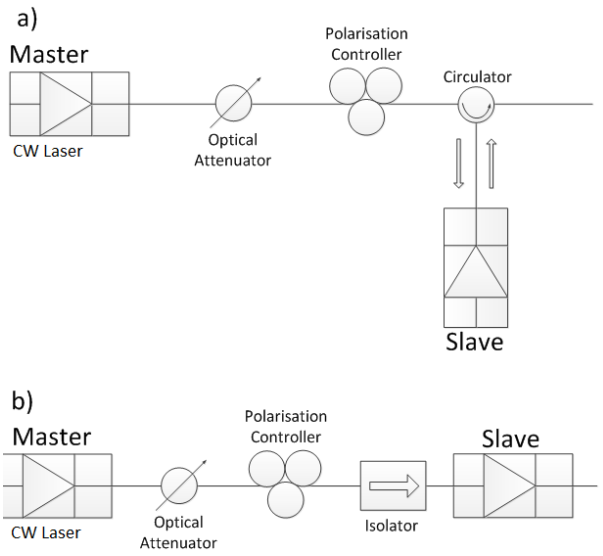

FIGURE 2.4: Optical injection locking a) Reflection, b) Transmission.

dependant coefficient. The sum and product is a lot easier for a computer to perform than a derivation. For simplicity the nonlinear term that contains no derivative can be solved in the time domain. The SS-FM divides the length of the fibre into a large number of small segments, of length h. The SS-FM is accurate to the second order of the step size h. However if the symmetrized SS-FM is used the accuracy can be increased to the third order of the step size h [15].

2.7 Optical injection locking

Optical injection locking (OIL) refers to a technique where the frequency and phase of a laser, known as the slave, are forced to follow those of another laser, known as the master, by injecting some of the light from the master to the slave [46]. Fig. 2.4 displays the two different methods in which OIL can be implemented. Fig. 2.4 a) displays OIL in reflection. Here the master light is coupled into the slave laser from the same interface as the slave light is coupled out. A circulator is used to ensure that the light in and out of the slave laser proceeds in the correct direction. Fig. 2.4 b) displays OIL in transmission. Here the master light enters the slave laser through one interface and the slave laser light leaves through another. An isolator is used to ensure that there are no back reflections to the master laser. In both cases the polarisation of the master light has to be aligned to that of the fundamental polarisation axis of the slave laser. The technique used in Chapter 4 will employ OIL in reflection, in order to demonstrate OIL based phase preserving amplitude regeneration.

Fig. 2.5 displays the analytically calculated master to slave laser ratio response, obtained by [3], for the phase a) and amplitude b) response as a function of the modulation frequency. The phase-to-phase response is given by $m_{PM-PM} = \Delta\phi_{slave}/\Delta\phi_{inj}$ where

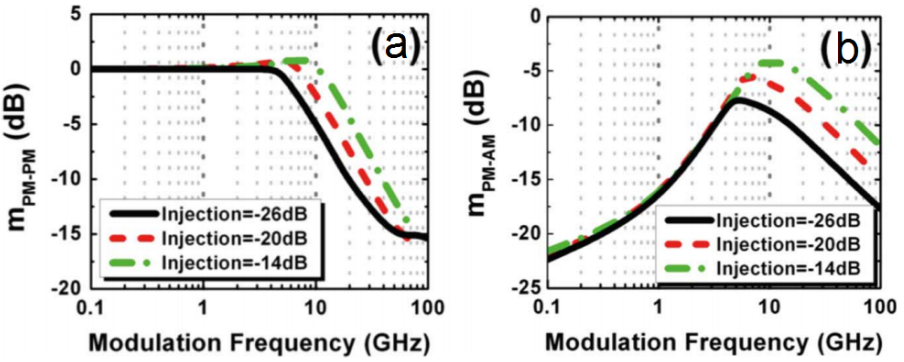

FIGURE 2.5: Analytical slave laser response for a) phase response and b) amplitude response as a function of the modulation frequency. For black solid line is -26 dB, dashed red is -20 dB and dashed-dotted green line is for -14 dB of injection level. Taken from [3]

$\Delta\phi_{slave}$ and $\Delta\phi_{inj}$ are the modulation depth of the phase content of the slave output and injected signal, respectively. The phase-to-amplitude response is given by $m_{PM-AM} = \frac{(\pi/2)/\Delta\phi_{inj}}{P_{slave}/\Delta P_{slave}}$ where P_{slave} is the mean value of the slave power while ΔP_{slave} is its standard deviation. The black solid line is -26 dB, dashed red is -20 dB and dashed-dotted green line is for -14 dB of injection level, where the injection level is the ratio of master optical field to slave optical field. Here Fig. 2.5 a) displays a constant phase response up until approximately 10 GHz. Fig. 2.5 b) displays an increase in phase to amplitude conversion up until the frequency of around 10 GHz, after which the phase to amplitude conversion decreases.

Fig. 2.6 displays the analytical master to slave laser ratio response, obtained by [3], for amplitude suppression a) and amplitude to phase conversion b) as a function of the modulation frequency, for a constant bias current of 40 mA. Here the normalised amplitude to amplitude transfer ratio is given by $m_{AM-AM} = \frac{P_{inj}/\Delta P_{inj}}{P_{slave}/\Delta P_{slave}}$ where P_{inj} is the mean value of the injected power while ΔP_{inj} is its standard deviation. The normalised amplitude to phase transfer ratio is given by $m_{AM-PM} = \frac{P_{inj}/\Delta P_{inj}}{\phi_{slave}/\Delta\phi_{slave}}$ where ϕ_{slave} is the mean value of the slave phase. The injection level varies for the black solid line at -20 dB, dashed red at -14 dB and dashed-dotted green line at -8 dB. Fig. 2.6 a) displays the amplitude response of the slave laser. For each injection level the amplitude conversion starts low at low modulation frequency and reaches its maximum at the resonance of approximately 10 GHz, after which it decreases. Fig. 2.6 b) displays the three curves for various injection levels for amplitude to phase conversion. Here, with higher injection levels the amplitude to phase conversion swing from low to high modulation frequency is greater, with the lowest injection level (-20 dB) only having an amplitude to phase noise conversion swing of approximately 5 dB. All injection levels exhibit the highest amplitude to phase conversion at around 10 GHz, after which the conversion level drops.

OIL is a complimentary tool which is used for cleaning the signal from its noise. This

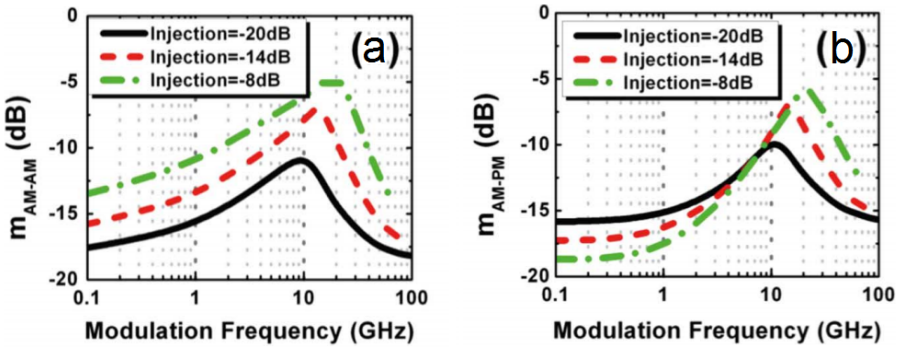

FIGURE 2.6: Analytical slave laser response for a) amplitude suppression and b) amplitude to phase conversion as a function of the modulation frequency for a constant bias current of 40 mA. For black solid line is -20 dB, dashed red is -14 dB and dashed-dotted green line is for -8 dB of injection level. Taken from [3]

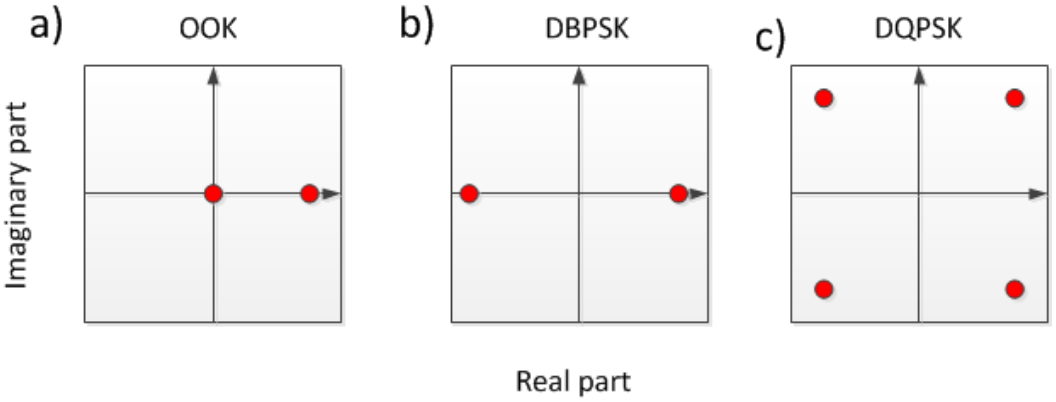

FIGURE 2.7: Optical modulation formats, a) OOK b) DBPSK and c) DQPSK

aspect of OIL is highlighted in Section 4.3 where it is used to perform phase preserving amplitude regeneration within a 600 km dark fibre transmission experiment.

2.8 Modulated Optical Signals

There are four main properties of an optical field that can be modulated with data, the amplitude, the phase, the frequency and the polarisation. Within this thesis we will be partly using amplitude modulated (in the form of On-Off keying (OOK)) and mainly using phase modulated (in the form of Phase-shift keying (PSK)) signals. Fig 2.7 displays example constellation diagrams of a) OOK, b) DBPSK and c) DQPSK signals. A mixture of multiple amplitude and phase modulations can be imagined, such as 4 level amplitude shift keying (4-ASK), which is used in Chapter 4 [20].

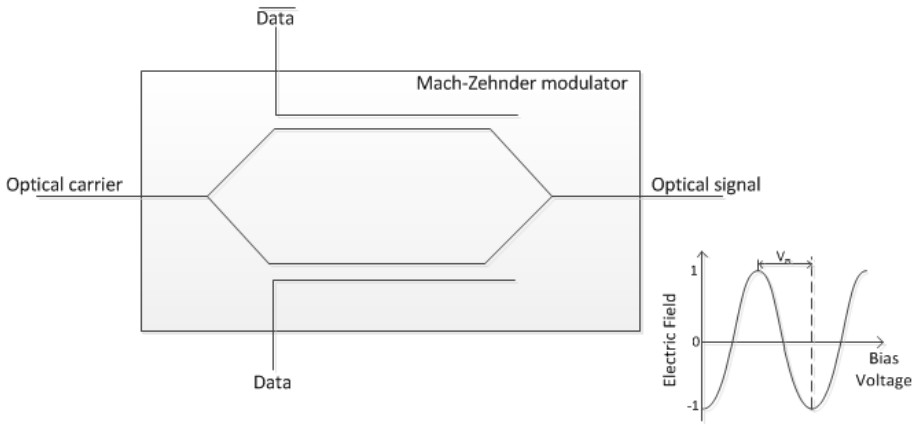

FIGURE 2.8: Description of a Mach-Zehnder modulator.

2.8.1 Optical amplitude and phase encoding

Encoding phase information onto an optical carrier can be achieved using an electro-optic modulator. Fig. 2.8 displays how a Mach-Zehnder modulator (MZM) works. A phase modulator can be placed in one or both arms of the MZM such that when an electrical signal is applied to it the effective length is changed through changing the refractive index of the medium. This in turn causes a variation of the interference at the output of the MZM which appears as the inset in the bottom right of Fig. 2.8. The term V_π is the voltage necessary to apply a π phase shift within the output optical power from the output of the MZM. Depending on the bias point and the bias voltage swing a MZM can be used to generate an OOK signal or a BPSK signal.

To detect OOK encoded signals direct detection is used, this can be schematically seen in Fig. 2.9 a) where the optical signal is detected using a photodiode. To detect BPSK or QPSK it is possible to use differential detection, however for more advanced modulation formats coherent demodulation has to be used. Fig. 2.9 displays a method to differentially b) and coherently c) detect a phase encoded signal. Fig. 2.9 b) displays the schematic of a DPSK demodulation scheme using a delay line interferometer (DLI). This DLI coherently sums a delayed (by one bit duration) signal to itself thus registering a change in phase between the adjacent symbols by an intensity increase. A balanced photodetector is used to retrieve the whole information. Differential detection can be used up to DQPSK signals, however the complexity of the scheme will increase.

Fig. 2.9 c) displays the coherent detector, where in this case the full signal can be reconstructed. Here the signal (S) is combined with a local oscillator (LO) in a 90^o optical hybrid assuming homodyne detection (S and LO have identical frequencies) and same polarisation state for both waves. Two electrical outputs I_I and I_Q at the output of the coherent detector are given by Eq. 2.29.

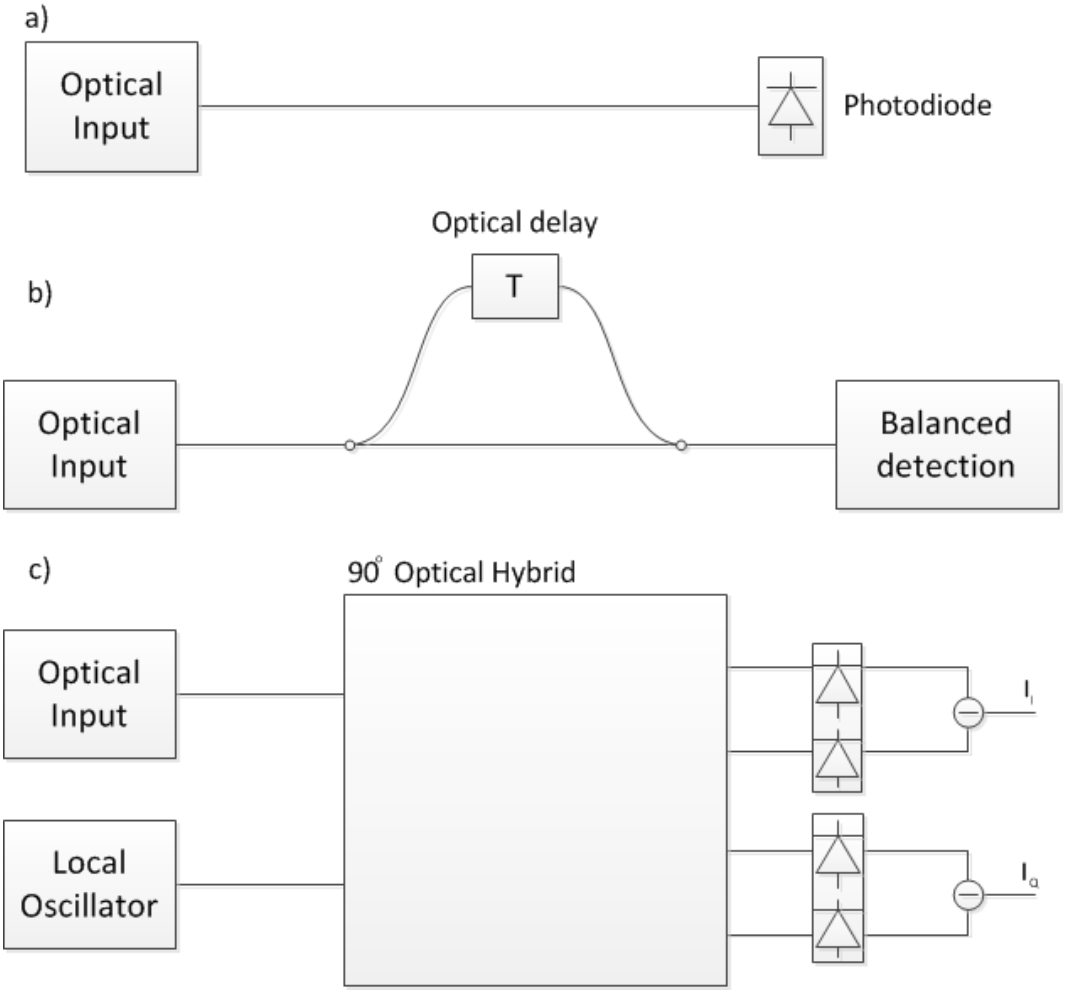

FIGURE 2.9: a) Direct detection using photodiode, b) Differential detection using a Delay Line Interferometer, c) Coherent detection using a 90 degree hybrid.

$$\begin{aligned} I_I &\propto \sqrt{P_S(t)P_{LO}(t)}\cos(\phi_s(t) - \phi_{LO}) \\ I_Q &\propto \sqrt{P_S(t)P_{LO}(t)}\sin(\phi_s(t) - \phi_{LO}) \end{aligned} \tag{2.29}$$

Where $P_S(t)$ is the electrical power of the signal, $P_{LO}(t)$ is the local oscillator power, $\phi_s(t)$ is the phase of the signal and ϕ_{LO} is the phase of the local oscillator. From Eq. 2.29 it is possible to calculate the phase and power of the input signal, with the phase being $\tan^{-1}(I_i/I_Q)$ and the power being proportional to $\sqrt{I_i^2 + I_Q^2}$.

Advanced modulation format signals are usually assessed by their Error Vector Magnitude (EVM). The EVM is a way to quantify the displacement of the measured constellation point from that of the correctly positioned reference point. The length of the vector between these two points (reference and measured) gives the EVM and can be calculated as the hypotenuse of the right angled triangle created by considering the separate magnitude of the quadrature error and in-phase error to be the other sides of the triangle, as shown in Fig. 2.10.

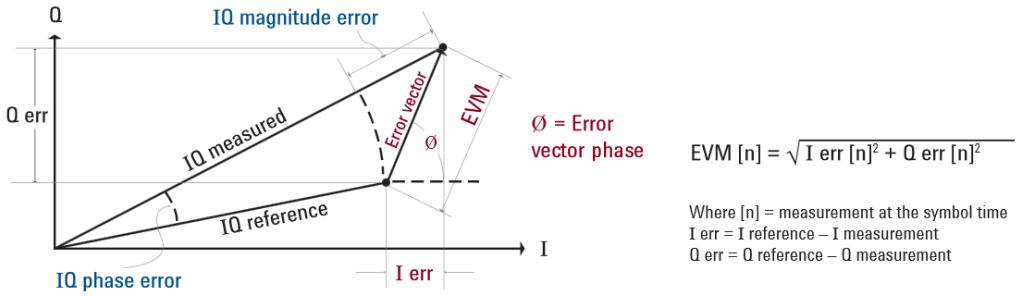

FIGURE 2.10: EVM calculation, taken from [4].

Another important tool to assess a signal is the Bit Error Ratio (BER) measurement. The BER is assessed at a certain optical signal to noise ratio. The BER is the ratio between the measured error bits and the total number of bits over a certain time period. For instance, if a BER of $1\text{x}10^{-6}$ is shown then that would equate to 1 bit error for every million measured bits.

2.9 Noise degradation within communication systems

Within a long-haul optical fibre telecommunications link there will be many in-line amplifiers (most commonly Erbium doped fibre amplifiers (EDFA)). Each amplifier has a noise figure, defined as:

$$F_N(dB) = SNR_{IN}(dB) - SNR_{OUT}(dB) \tag{2.30}$$

Where, $SNR_{IN}(dB)$ represents the signal to noise ratio (SNR) at the input of the amplifier and $SNR_{OUT}(dB)$ represents the SNR of the amplified signal at its output, all are in the logarithmic scale. Here the optical SNR (OSNR) corresponds to the average optical signal power divided by the optical noise power. The OSNR differs from the SNR (or electrical SNR) as the SNR corresponds to the average signal voltage divided by the root-mean squared (RMS) noise voltage. In optical systems it is often more relevant to define the OSNR. In a cascaded chain the amplified spontaneous emissions (ASE), created by the amplifiers, increases and eventually begins to saturate the successive amplifiers in the chain resulting in a subsequent reduction in their gain, and output OSNR. The amplifier noise can also induce timing jitter onto the binary bit stream. This problem introduces a fundamental limit to the maximum length of a transmission link. The typical noise figure of commercial erbium doped fibre amplifiers (EDFA) ranges between 3.5 dB to 5 dB depending on manufacturer. Dispersive and nonlinear effects are another limiting factor in long-haul transmission links. Due to the very long nature of long-haul transmission links the accumulation of nonlinear effects, most notably SPM, XPM and FWM, becomes a limiting factor for the length of the optical link. The Gordon-Mollenauer effect [47] describes the interaction of signal with noise in

transmission. Optical modulation formats that encode their signals onto the phase of a carrier field are subject to amplitude-to-phase noise conversion, due to the nonlinear Kerr effect in the transmission fibre.

2.10 Optical regeneration

One of the first all-optical regenerators was the Mamyshev regenerator, [48], here a signal is amplified and passed through a nonlinear element. Here spectral broadening occurs (due to SPM). At the output an optical bandpass filter is used, which is spectrally offset by an amount $\Delta\lambda$ with respect to the input signal carrier wavelength. Thus the signal that represents a binary 1 is equalised by being allowed to pass through a spectrally offset filter. If a signal is not powerful enough to produce significant SPM based spectral broadening, i.e. a binary '0', then nothing will pass through the spectrally offset filter creating a nonlinear amplitude response. One problem with the Mamyshev regenerator is that the phase of the signal is not preserved, which is adequate for OOK signals but not for more advanced modulation formats such as BPSK and QPSK signals. There are two main types of regenerators for advanced modulation formatted signals: amplitude regenerators and phase regenerators. For amplitude regenerators it is important that the phase is preserved, similarly for phase regenerators it is important that the amplitude is preserved. Phase preserving amplitude regenerators have been observed with the use of vertical microcavity saturable absorbers [49]. Similarly phase preserving amplitude regeneration has been observed using optical injection locking of a discrete mode semiconductor laser [29]. Work reported in [50] presented the numerical model of a system that can regenerate up to 256-QAM using cascaded regenerative Fourier transformation based on a novel nonlinear oscillating loop mirror (NOLM) PSA and MZM design. Alternatively both phase and amplitude regeneration have been observed using periodically poled lithium niobate (PPLN) [51]. For more advanced PSK signals PSAs are used to perform regeneration of the phase in an all optical manner. Reference [52] contains work done to regenerate the phase and amplitude of a DPSK signal using a Sagnac interferometer based PSA. Work has also been done to produce a black box all optical regenerator for a BPSK signal, shown in [2]. Here FWM within the two HNLFs are used to produce the spectral and phase harmonics before entering the PSA where the signal and its conjugate are mixed. A similar technique as used within [2] was used to demonstrate all optical regeneration of a QPSK signal, shown in [9]. Recently, a gain variation suppression version of the regenerator shown in [9] has been demonstrated. This regenerator operates by way of introducing another phase harmonic which negates the majority of the phase to amplitude noise conversion that impedes these types of FWM based regenerators [10]. Further work has been conducted using nonlinear amplifying loop mirrors (NALMs) to regenerate an 8-QAM signal [53]. Here a signal is split and sent in counter-propagating ways around a NALM before being amplified by

differing degrees. The highly nonlinear fibre (HNLF) within the NALM is used to perform FWM and apply specific phase shifts to the counter-propagating signals in order to achieve a nonlinear amplitude and phase response required for the regeneration of an input 8-QAM signal.

There have been several published reports of optical regenerators for complex modulation formats. They are based on a variety of technologies, ranging from vertical microcavity based saturable absorbers [49] to PSAs based on HNLFs [9, 54, 55]. A vertical microcavity based saturable absorber (SA) regenerator was published in 2012 [49], which was used in an experimental demonstration to achieve amplitude regeneration for a RZ-DQPSK signal at a repetition rate of 42.6 Gb/s. The regenerating SA was combined with a demultiplexer and fibre array arrangement, which allowed eight WDM channels to be processed at the same time. The SA was tested in a 100 km long recirculating loop where a nonzero dispersion shifted fibre was compensated by a dispersion compensating fibre. The regenerator provided a Q factor improvement of 1.4 dB. In transmission, a 3 dB or better distance improvement ratio (at a BER of 10^{-4}) was observed for a bandwidth of 13 nm, between 1540 nm and 1553 nm.

Amplitude regenerators relying on fibre-based loop mirrors have also been reported in the literature. The nonlinear optical loop mirror (NOLM) and the nonlinear amplifying loop mirror (NALM) both rely on an asymmetric coupler to split the incoming optical field into two counter-propagating waves. These two counter-propagating waves propagate around a loop containing a nonlinear fibre. Whereas the NOLM relies solely in the asymmetric coupler in order to excite more nonlinear effects on one direction of the propagation than in the other, the NALM includes a bi-directional fibre amplifier that is placed asymmetrically inside the loop. The amplifier amplifies the weaker signal of the two which eventually experiences stronger SPM within the nonlinear fibre. SPM and FWM (using injected pumps) can be used within the nonlinear fibre in order to achieve relative phase changes between the counter-propagating waves. Once these waves have completed a full circuit of the loop and reach the input coupler they are combined and any phase differences accumulated within the loop manifest themselves as constructive or destructive interference. A NALM/NOLM based regenerator was studied both numerically and experimentally in [56]. This paper demonstrated amplitude regeneration of a 10 Gb/s DQPSK signal, offering a 5 dB receiver power penalty improvement at a BER of $1\text{x}10^{-6}$. The NOLM/NALM configurations are often combined with a (unidirectional) PSA, also implemented inside the loop, so that simultaneous phase and amplitude regeneration can be achieved. However, because of the complexity of the required components incorporated in these configurations, most of the publications studying these solutions rely on numerical simulations rather than experimental demonstrations. In a paper published in 2014, the NALM based regenerator [53] was applied to achieve both amplitude and phase regeneration on a star 8-QAM modulation format. Through numerical simulations, it was shown that up to a 5 dB EVM improvement could be

observed for the low power states. A numerical study on a different NOLM based regenerator [57] showed the potential for amplitude regeneration of circular 16-, 64-, and 256-QAM signals. Decreases in the symbol error rate from $1.3\text{x}10^{-4}$ to $1.4\text{x}10^{-6}$, from $4\text{x}10^{-3}$ to $2.6\text{x}10^{-5}$ and from $1\text{x}10^{-2}$ to $1.4\text{x}10^{-4}$ were calculated for circular 16-, 64- and 256-QAM, respectively. In a following publication, the same authors published another NOLM based regenerator [50] offering both amplitude and phase regeneration for 4-, 16-, 64- and 256-QAM signals using two orthogonal regenerative Fourier transformations. Most notably, a 7.5 dB SNR improvement at a symbol error rate of $1\text{x}10^{-3}$ for 16-QAM was numerically predicted.

Phase-sensitive amplification implementations have attracted considerable attention for their potential for phase regeneration. In one of the earlier publications, a PSA based on a Sagnac interferometer [58] was used in an experiment to demonstrate phase and amplitude regeneration of a 10 Gb/s (N)RZ-DPSK signal. With a pump power at 922 mW, a SNR improvement of 8.4 dB was achieved. This idea was further developed both by these authors and other groups [2, 59, 60], resulting in a number of successful experimental demonstrations of phase and amplitude regeneration for DPSK signals. This principle was subsequently applied on semiconductor optical amplifiers (SOA) and extended to accommodate two BPSK channels at the same time [61]. This regenerator achieved a 2 dB receiver sensitivity improvement between the SNRs of 6 and 12 dB. Using second-order nonlinearities, a PSA based on PPLN waveguide [62] demonstrated experimentally phase regeneration of a 28 Gb/s BPSK signal. A breakthrough was achieved in 2010, when a fibre-based PSA based HNLF regenerator was shown to be capable of achieving regeneration of QPSK signals in experiments involving 10Gbaud signals [9]. This regenerator achieved a phase noise reduction by a factor of 2. Extending the number of channels accommodated in regenerators is generally challenging, because of the impact of competing nonlinear effects on the cross-talk experienced by the various channels. A recent publication has relied on (i) pumping on orthogonal polarisations and (ii) bi-directional propagation in the same HNLF to demonstrate simultaneous phase regeneration of six WDM channels carrying 10 Gb/s NRZ-BPSK signals [54]. In a different work, another PSA based HNLF regenerator [55] demonstrated experimentally phase regeneration of four 10 Gb/s DPSK signals. Table 2.1 tabulates and compares the above mentioned regenerators.

Within this thesis, novel methods for all optical regeneration will be explored with the focus of producing methods that are simpler and which can regenerate more complex modulation formats.

2.11 Conclusion

This chapter gives an overview of the main topics that need to be understood for the comprehension of the work performed within this thesis. This chapter offers a description of the fundamentals of wave propagation in an optical fibre followed by different effects of dispersion. Nonlinear refraction is discussed alongside self and cross phase modulation. An analytical explanation of FWM and FOPA gain characterisation are offered such that phase sensitive amplification can be more understood. This is followed by the description of some of the inelastic scattering mechanisms in optical fibre, namely SRS and SBS. The NLSE is introduced and its solution using the SSFM is described, which is used within this thesis to perform simulations of parametric devices used for regeneration. Optical injection locking is briefly introduced within this chapter. A number of optical modulated signals are introduced and described. Noise degradation within a communication system is discussed as this will be of importance in the transmission experiments conducted. Finally, a literature review in optical regeneration is reported.

Ref	Tech. Base	Amp/ Phase Regen.	Rep Rate	Mod. Format	Experi/ Numeri	Year of Pub.	Performance Improvement
[49]	Vertical microcavity based saturable absorber	A	42.6Gb/s	RZ-DQPSK	E	2012	Q factor improvement of 1.4 dB
[53]	NALM	A+P	N.A.	Star 8-QAM	N	2014	up to a 5 dB EVM improvement
[56]	NOLM, NALM	A	10 Gb/s	DQPSK	E+N	2012	5 dB receiver power penalty improvement at a BER of $1x10^{-6}$
[57]	NOLM	A	N.A.	up to circular 256-QAM	N	2014	A decrease in symbol error rate from $1x10^{-2}$ to $1.4x10^{-4}$ for circ 256-QAM
[50]	NOLM	A+P	N.A.	up to square 256-QAM	N	2015	7.5 dB SNR improvement @ BER of $1x10^{-3}$ for 16-AQAM
[58]	PSA based on Sagnac interferometer	A+P	10Gb/s	NRZ-DPSK + RZ-DPSK	E	2008	8.4dB SNR improvement @ pump power of 922mW
[62]	PPLN based PSA	P	28Gb/s	BPSK	E	2013	2600 km transmission improvement @ BER of 10^{-4}
[61]	SOA based PSA	A+P	N.A.	BPSK	E	2013	2 dB receiver sensitivity improvement between SNR of 6-12 dB
[9]	PSA based on HNLF	P	10GBaud	QPSK	E	2010	Phase noise reduction by a factor of 2
[54]	PSA based on HNLF	P	10Gb/s	NRZ-BPSK	E	2015	Simultaneous 6 channel phase regeneration
[55]	PSA based on HNLF	P	10Gb/s	DPSK	E	2015	Simultaneous 4 channel phase regeneration

TABLE 2.1: All-optical regenerative technology comparison.

Chapter 3

Signal and Noise synthesis

3.1 Introduction

With a lot of the work performed within this thesis dedicated towards the realisation of all-optical regenerators, a number of tools for generating and assessing the performance of signals needed to be developed. There are five main sections to this chapter. Firstly, a method to emulate a QPSK signal from a BPSK signal, through the use of a delay line interferometer (DLI), is described. Secondly, an opto-electronic feedback system is designed, implemented and tested which allows the automatic phase bias control of the DLI, ensuring stabilisation against thermal variations, this work was conducted my me but was envisaged by Dr. Joseph Kakande. Thirdly, the technique used to emulate a QPSK signal is expanded to allow emulation up to 16-QAM starting from a BPSK signal. Next, a method to convert the modulation format and compress the size of the optical packets is investigated which encompasses much of the work within the QPSK and 16-QAM emulation sections, however, with the added complexity of timing gating and coherent temporal superposition, all work within this section was primarily conducted by Dr. Francesca Parmigiani, I offered a supporting role in the laboratory. Finally, the development of a broadband phase noise emulation technique, which relies on the transfer of amplitude noise (present on a amplifier spontaneous emissions (ASE) noise source) to phase noise (manifested onto the signal) through XPM effects within a HNLF is discussed followed by an example application that used this broadband phase noise generation system, again the work within this subsection was conducted by myself but envisaged by Dr. Joseph Kakande.

3.2 QPSK Emulation

A technique for experimentally emulating a QPSK signal from a BPSK signal had already been developed in our lab before the start of this project. For completeness, this section

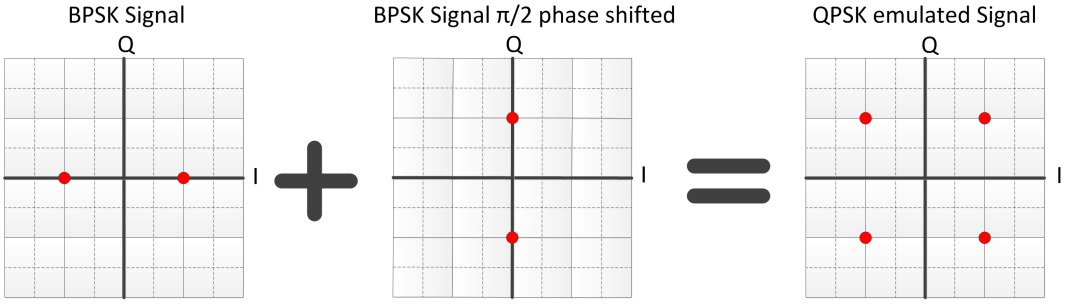

FIGURE 3.1: QPSK signal emulation

will describe this technique and present its characterisation. In general QPSK is of interest to telecommunications because it potentially allows a doubling of the spectral efficiency over any given OOK or BPSK signal system. The significance of this is twofold. Firstly, for laboratory experiments, this QPSK emulation offers a method to test device applications without the need for a typically expensive QPSK transmitter. Secondly, this method allows further scaling to even more complex modulation formats, such as 16-QAM, as will be discussed in section 3.3. Normally, QPSK signals are generated using an IQ (in-phase and quadrature phase) modulator driven by two fast electrical signals. The IQ modulator contains two separate Mach-Zehnder modulators (most commonly constructed from Lithium Niobate) in the same device, where one modulator is driven by an electrical signal which is associated to the In-phase information and is located in one arm of the device. Conversely, the other modulator is driven by an electrical field which is associated to the Quadrature-phase information and is located on the other arm. The arm containing the Quadrature-phase modulator will have a 90^o optical phase shift with respect to the In-phase arm. The two independent optical signals from each arm are coherently combined at the output of the IQ modulator, thus generating the QPSK signal with two bits per symbol. In contrast, the method that has been implemented for this research project used a DLI to emulate the optical transmission characteristics of QPSK, using one BPSK signal as its starting point. Using this technique, a signal resembling a QPSK format was generated, even though each symbol was not independently encoded, as one is simply a delayed replica of the other.

3.2.1 Operation principle

Fig. 3.1 sketches the operation principle of the technique through constellation diagrams. A constellation diagram represents the amplitude (magnitude between the origin of the Cartesian axis and the symbol of interest) and phase (angle of turn in an anticlockwise direction from a reference axis, usually the In-phase axis, and the symbol of interest) of the electric field of the signal under consideration. As mentioned earlier a signal with QPSK characteristics can be obtained by coherently adding a BPSK signal with a copy of itself which has been delayed and phase-shifted, so that its phase has been rotated by 90^o with respect to its original phase, as shown in Fig. 3.1. In the actual

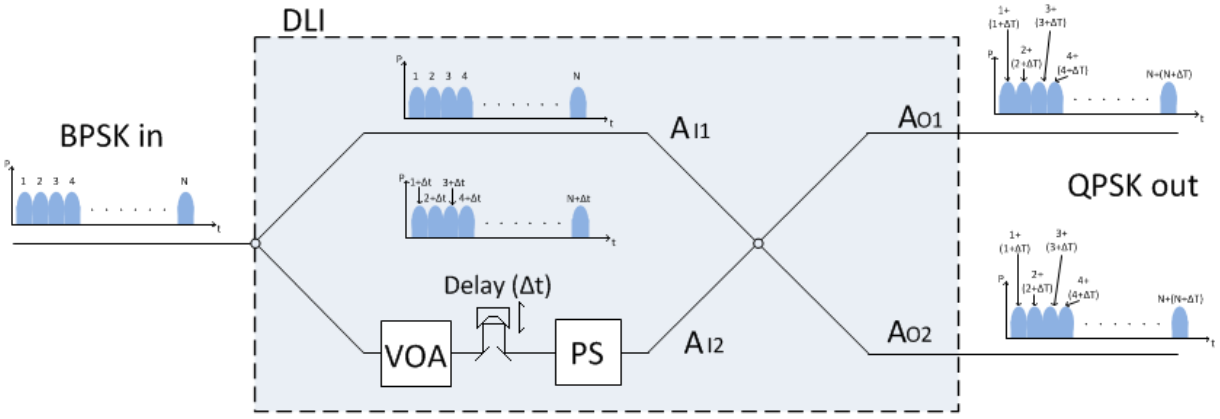

FIGURE 3.2: DLI schematic, adapted from [5]. VOA-Variable optical attenuator, PS - phase shifter

implementation the BPSK copy is also temporally delayed by a few bits (Δt), such that $\Delta t = nT$, where n is an integer number and T is the bit period, with respect to the original, so that decorrelation between the two BPSK signals can occur. Fig. 3.2 presents a schematic of the implementation set-up of the QPSK emulator. A_{I1} in the figure represents the original BPSK signal, whereas A_{I2} represents its temporally delayed and phase shifted copy. A_{O1} and A_{O2} are both emulated QPSK signals which are generated at the output of the DLI. The free spectral range (FSR) of the DLI is defined as the frequency representation of the propagation time difference between the two arms inside the DLI (delay seen in Fig. 3.2 as Δt).

$$FSR = \frac{c}{2n_g L} \tag{3.1}$$

Where c is the speed of light in a vacuum and n_g is the refractive index, which is 1 for the free space medium within the DLI and L is the length mismatch between the two arms of the interferometer.

$$bitdelay = \frac{\frac{1}{FSR}}{\frac{1}{Bitrate}} = \frac{Bitrate}{FSR} \tag{3.2}$$

Eq. 3.2, taken from [5], can be used to calculate the delay between the two BPSK signals from the FSR and original signal bitrate, where the bit delay is the number of bits that one BPSK signal can be delayed from the other.

The FSR of the DLI has to be selected so that it will produce an integer multiple temporal delay of the most common bitrates used in the laboratory experiments. Ideally, one would desire to maximise the decorrelation between the two BPSK signals by increasing the path mismatch between the two DLI arms. However, as this path mismatch increases, the device becomes more difficult to stabilise against thermal variations. The most common experimentally used bitrates within the laboratory are 10, 20 and 40 Gbps.

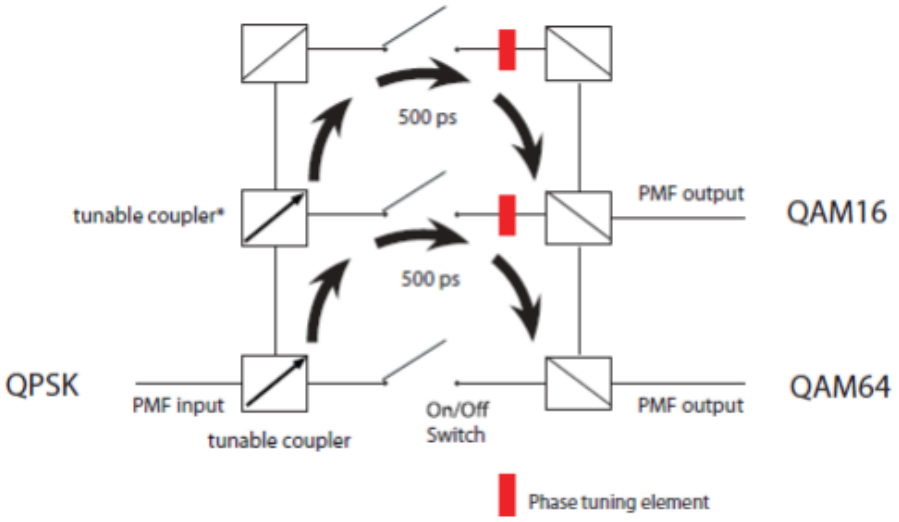

FIGURE 3.3: Block diagram of 64-QAM emulator, taken from [6]

The FSR for the Kylia Technologies® DLI was selected at 2.5GHz (2.501GHz precisely measured by manufacturer, which was the largest that they could produce).

From Eq. 3.2 it follows that for signal repetition rates of 10, 20 and 40 Gbps the DLI will produce temporal bit delays of 4, 8 and 16 bits, respectively.

It is important to note that Kylia Technologies®, since this work was conducted in 2011, have developed an integrated (up to) 64-QAM emulator system. Fig. 3.3 displays a block diagrams which consists of a tunable couplers, phase shifters and switches to firstly emulate a 16-QAM signal from an input QPSK signal, then subsequently emulate a 64-QAM signal from combining the 16-QAM signal with the input QPSK signal.

By varying the possible input phase states (from 0 or π, as with a BPSK signal) it is possible to create a state table for one of the output ports of the DLI (A_{O1}). The following state table, Table. 3.1, is generated, highlighting that the output signal is indeed a QPSK signal.

A_{I1} phase IN	A_{I2} phase IN	A_{O1} phase OUT
0	0	$\pi/4$
0	π	$7\pi/4$
π	0	$3\pi/4$
π	π	$5\pi/4$

TABLE 3.1: QPSK emulation state table.

3.2.2 DLI stabilisation system

Due to the relatively long path length mismatch between the two DLI arms, temperature fluctuations can occur and will affect the performance of the QPSK emulation technique

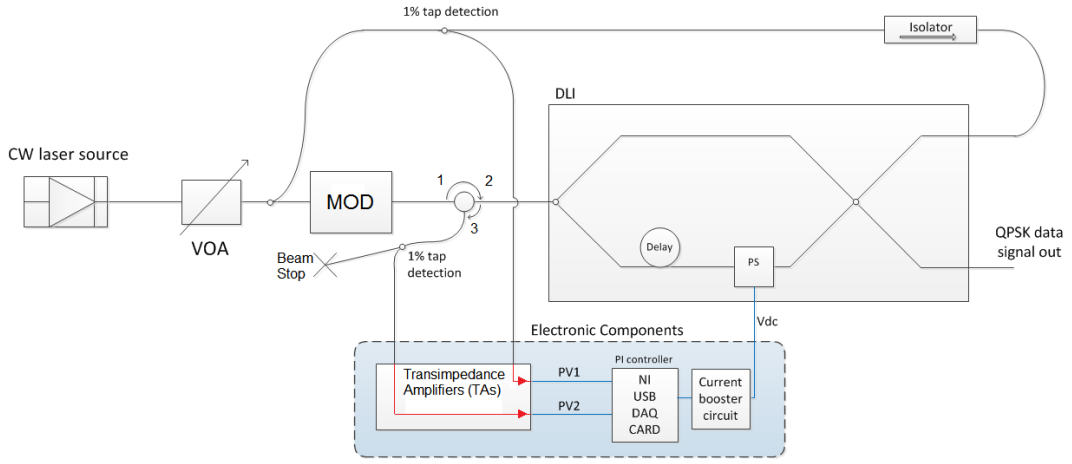

FIGURE 3.4: Full DLI stabilisation system, where MOD is Modulator and VOA is variable optical attenuator.

presented in section 3.2. In particular these temperature fluctuations will cause the $\pi/2$ phase shift between the two DLI arms to slowly drift away. A phase shifting element is placed in-line with the longer arm, whereby a bias voltage can be used to fine tune its overall propagation length. This bias voltage can be modified to compensate for the temperature induced path mismatch. This section describes an opto-electronic stabilisation feedback system that can automatically modify the bias voltage to the phase shifting element in order to maintain a stabilised path mismatch and thus a good QPSK signal, regardless of the temperature fluctuations effecting the system. The main contributing sections of this stabilisation system are: detection of the optical signal (performed using tap photodiodes); current to voltage conversion (performed using a transimpedance amplifier (TA)); signal processing (performed using a proportional-integral-derivative (PID) controller); and finally current amplification (performed using a transistor). During the implementation of the stabilisation system, particular attention was paid to the development of the signal processing section. For this purpose a National Instruments Labview® USB 6009 data acquisition (DAQ) card was used. Many parameters of the system were permitted to be adjusted in real time to ensure a fast and accurate system stabilisation debugging time. Fig. 3.4 shows the schematic of the full DLI system including the CW laser source and the BPSK modulator. An existing technique to stabilise a DLI has been described in [63], however, the implementation introduced in this section is more efficent as it uses fewer expensive components. A portion of the forward propagating CW optical field into the transmitter is tapped off and entered into one of the DLI output ports, which is not in use, in the backward (from right to left) propagating direction. The backward propagating optical field is split and sent through the two DLI arms before being coherently recombined at the input of the DLI. The optical field is sent to a circulator, to separate it properly from the BPSK signal, and detected by a 1% (power detection ratio) tap-photodiode. Another 1% tap-photodiode is used to measure the optical power of the CW light as it enters the output port of the DLI. Both detected fields are sent to independent transimpedance amplifiers where

the current produced by the photodiode is converted to a voltage signal. These voltage signals are described as process variables (PV) within the feedback system. Process variable 1 (PV1) is associated to the voltage reference of the optical field detected before the CW light has entered the DLI in the reverse direction. Process variable 2 (PV2) is associated to the voltage reference of the optical field detected at the output of the DLI in the reverse direction (DLI inout port). Both PV1 and PV2 are external inputs to the DAQ card, where the proportional difference is mathematically calculated such that $\Delta PV = (PV1 - PV2)/PV1$ will represent the optical power ratio of the various ports of the DLI. Due to the way in which the DLI is constructed, the power that is observed at one of the output ports of the DLI is determined by the phase assigned to the phase shifting element in one of its arms. Neglecting component insertion losses, the power at one of the output ports can be expressed as the power at the other output port subtracted from the power at the input of the DLI, such that the total power out of both DLI output ports is constant. The phase shifting element can be used to transfer power from one output port to the other (and vice versa). For this stabilisation system it is important to ensure that equal power is maintained at each output port (as this ensures a steady QPSK signal at the output). Every time the CW signal power is changed, a new calibration is required, where a setpoint (SP) value (a desired output power, where the signal is shared equally between the two output ports) needs to be acquired. The PID controller requires the values of ΔPV, SP and the output of the PID controller (initially zero) known as the common output (CO). The PID algorithm generates an error signal, which is the difference between the values of ΔPV and the SP. The error signal acts as a linear stepper term which sums with the CO to produce the next iteration of the CO, such that CO = CO + error. The CO is fed into a current booster circuit before directly acting on the phase shifting element in the DLI. The PID controller repeats this process until the error term has been minimised and the SP value is reached. The DAQ card operates at 48K samples per second. The gain values for the proportional, integral and derivative error terms can be modified such that the system responds stably to external thermo-acoustic perturbations.

Appendix A goes into more detail about the electronic components in the DLI stabilisation system as well as the calibration of the DAQ.

3.2.2.1 Testing

There were two main ways in which the stabilisation system was tested. Firstly, a localised (and fast) temperature change was introduced turning on and off an incandescent lamp next to the DLI (test 1). Secondly, the wavelength of the CW laser was varied during the system stabilisation (test 2).

Test 1 - Local temperature change using lamp (impulse test)

Heating up the DLI will cause microscopic increases in size and hence relative path length mismatch between the two arms. Even though this relative path length increase is small, compared to the wavelength of the signal (1550 nm) the change can be seen as significant. Fig. 3.5 shows a graphical measurement of voltage versus time of the CO (green); PV1(red); PV2(black) and ΔPV (blue) with insets of the constellation diagrams at particular times of the measurement with and without the stabilisation system. Following the x-axis (time in minutes) of Fig. 3.5, going from left to right, the initialisation of the stabilisation system is shown. This took approximately two minutes but could be sped up by changing the proportional coefficient. Next, the lamp was placed over the DLI and turned on at approximately 12.5 minutes. The lamp was turned off at approximately 20 minutes. The test concluded at around 24 minutes. Fig. 3.5 shows five constellation diagrams relating to the test with the stabilisation system on and three constellation diagrams relating to the test without the stabilisation system (a constant bias voltage of 1.94V was used, which corresponds to the optimum value at the beginning of the test). The arrows show which constellations are associated to each other. It is clearly shown that without stabilisation the constellation diagram after the lamp has been turned on, at approximately 18 minutes, appears to be skewed to a rhomboidal shape. Whereas the constellation diagram for the stabilisation system appears as the desired square shape after stabilisation. This is due to the fact that the voltage of the CO has dropped to compensate for the additional phase shift that is introduced from the change in relative path length.

The error vector magnitude (EVM), as described in Section 2.8.1, was used to quantify the displacement of the measured constellation point from that of the correctly positioned reference point. Figs. 3.6, 3.7 and 3.8 show the EVM, Magnitude Error and Phase Error versus time for each constellation trace shown in Fig. 3.5.

Test 2 - Laser frequency shift by 12.5 GHz

The laser wavelength was then shifted by 0.1nm, from 1555.64 nm to 1555.74 nm. At the 1550 nm wavelength region this equates to approximately 12.5 GHz frequency shift. Fig. 3.9 shows the graphical measurements of the stabilisation system with the CO (green), PV1(red), PV2(black), ΔPV(blue), setpoint(cyan) voltages against time in minutes. The violent fluctuations shown in Fig. 3.9 are due to the ringing inside the laser cavity while it stabilises at the new wavelength. This ringing ceases once the laser has stabilised at the new wavelength (seen at approximately 6 and 14 minutes for both laser wavelength shifts). Fig. 3.9 shows the difference between the constellation diagrams as the CW wavelength was varied. It is shown that there is a slight skewing of the constellation diagram without stabilisation at 1555.74 nm. The manual system was stabilised at 1555.64 nm and that is why the constellation appears acceptable without feedback at this wavelength.

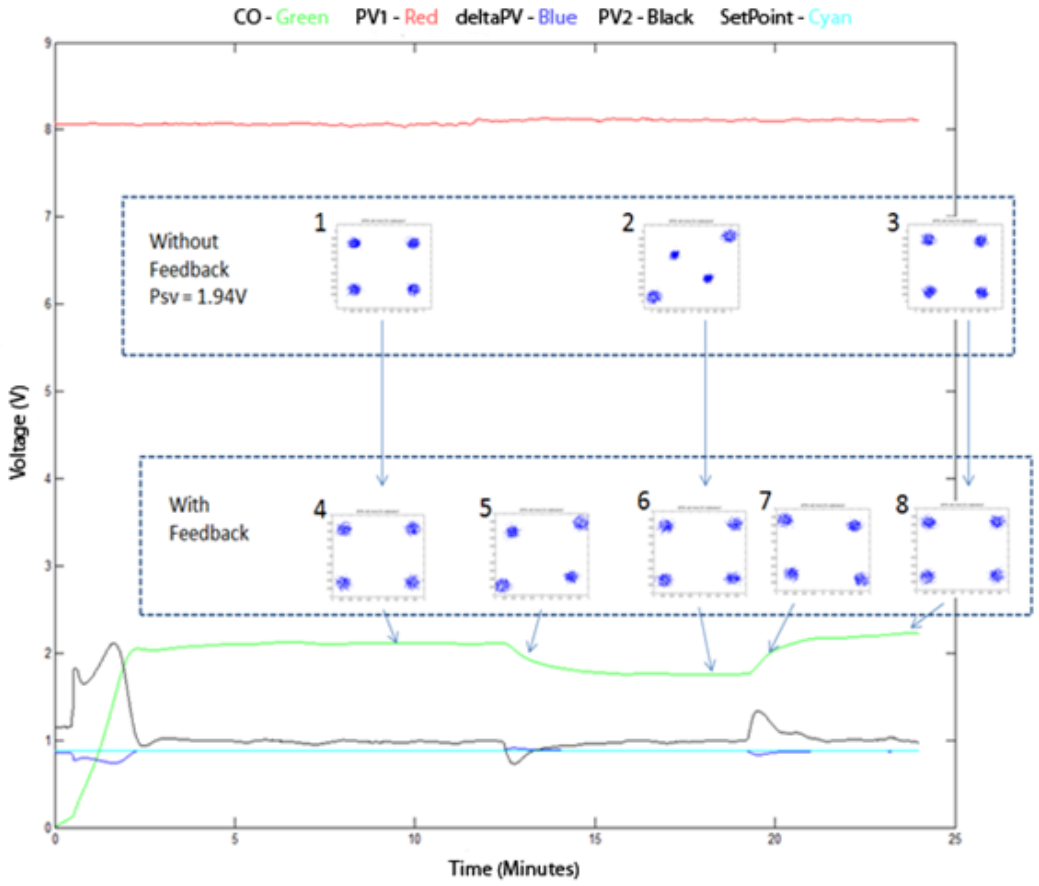

FIGURE 3.5: Lamp impulse test graph with inset QPSK constellation diagrams for with and without feedback stabilisation system.

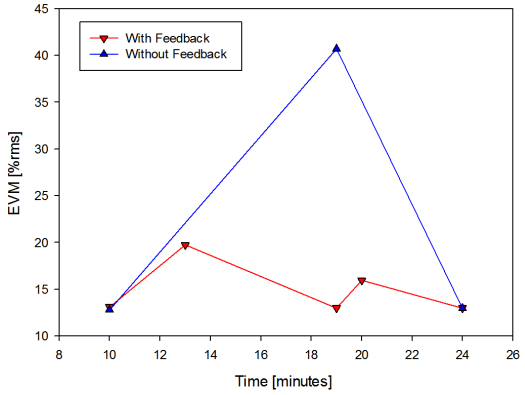

FIGURE 3.6: EVM [%rms] vs time [minutes] with (red) and without (blue) the feedback system.

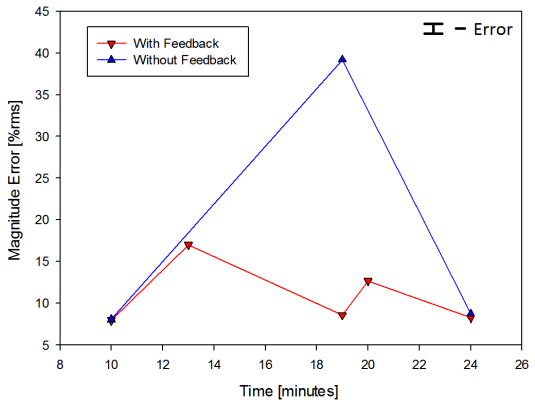

FIGURE 3.7: Magnitude Error [%rms] vs time [minutes] with (red) and without (blue) the feedback system.

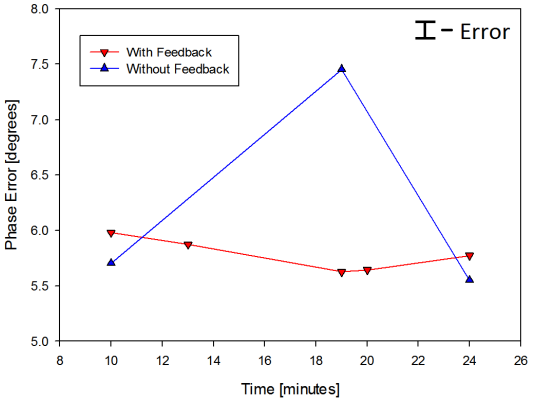

FIGURE 3.8: Phase Error [degrees] vs time [minutes] with (red) and without (blue) the feedback system.

Figs. 3.10, 3.11 and 3.12 show the EVM, Magnitude Error and Phase Error versus time for each constellation trace shown in Fig. 3.9. The figures show that there is an overall performance improvement with the use of the stabilisation feedback as opposed to operation without feedback. The best improvement is shown at 19 minutes, after the 12.5 GHz frequency shift and stabilisation of the lasers, where all values of EVM, magnitude and phase error are lower with feedback than without. Fig. 3.12 at 10 minutes displays a greater phase error value with feedback than without. This variation seen is within the error of the measurement.

3.3 16-QAM emulation

3.3.1 Operation Principle

Following the operation principle used in section 3.2 to emulate a QPSK signal from a BPSK signal using coherent combinations of optical signals, this section extends the

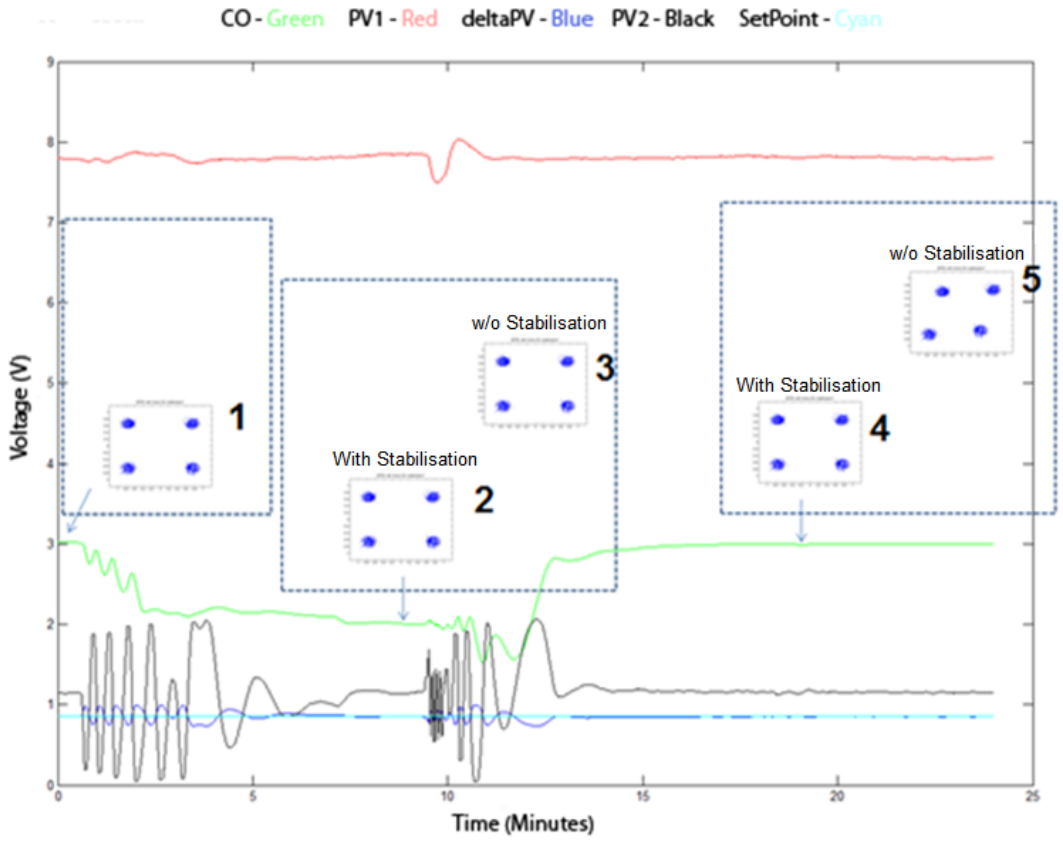

FIGURE 3.9: voltage vs. time graphical measurement with stabilisation feedback control. Insets show constellation diagrams for with and without feedback control stabilisation system.

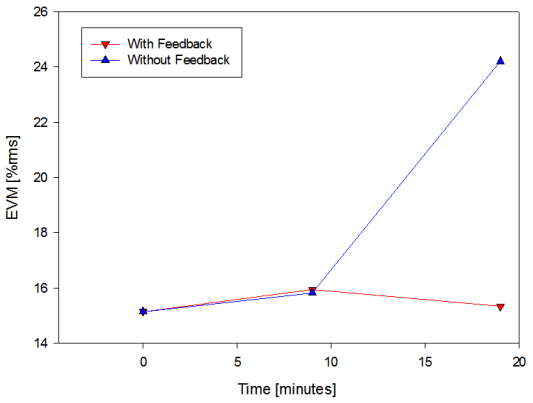

FIGURE 3.10: EVM [%rms] vs time [minutes] with (red) and without (blue) the feedback system.

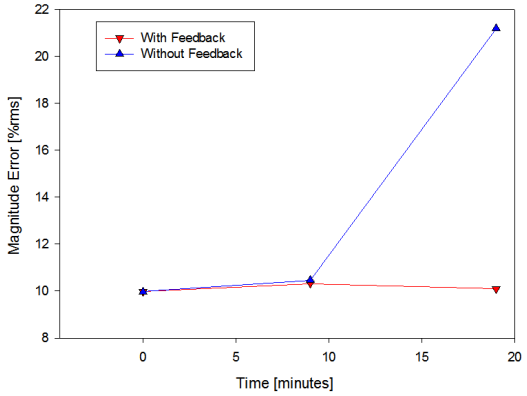

FIGURE 3.11: Magnitude error [%rms] vs time [minutes] with (red) and without (blue) the feedback system.

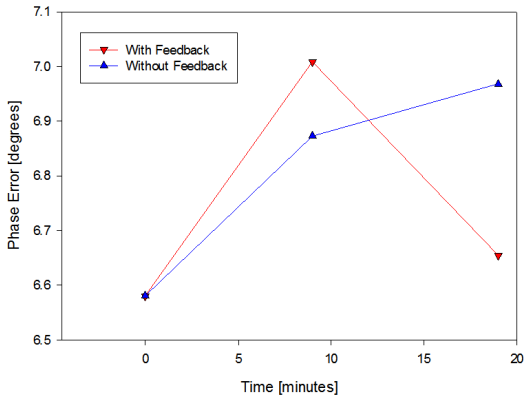

FIGURE 3.12: Phase error [degrees] vs time [minutes] with (red) and without (blue) the feedback system.

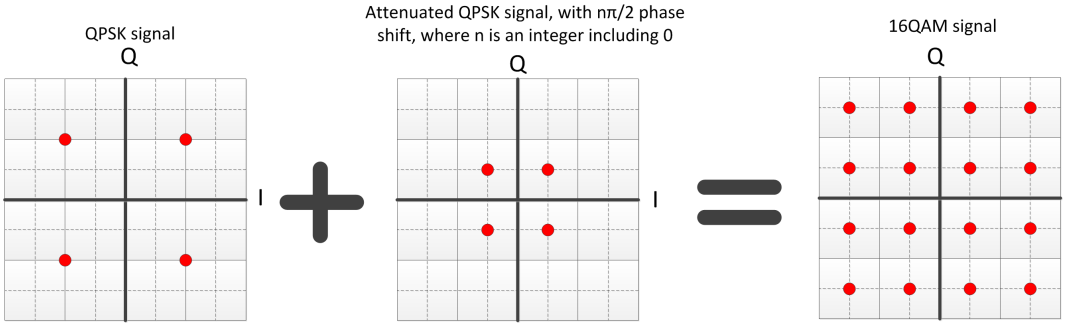

FIGURE 3.13: Emulation of 16QAM signal from a QPSK signal.

principle to 16-QAM signals starting from BPSK signals. Fig. 3.13 shows a diagrammatic representation of the 16-QAM generation technique from a QPSK seed signal.

If starting from a BPSK signal, then two DLIs (two stages) are required, the first one will be used to emulate a QPSK signal (as discussed in Section 3.2) and the second one to emulate a 16-QAM signal. The second DLI, however, will require one of the two arms to be attenuated by 6 dB (1/4 power in the linear domain) for the emulation to work as shown through the constellation diagram examples of Fig. 3.13. The phase

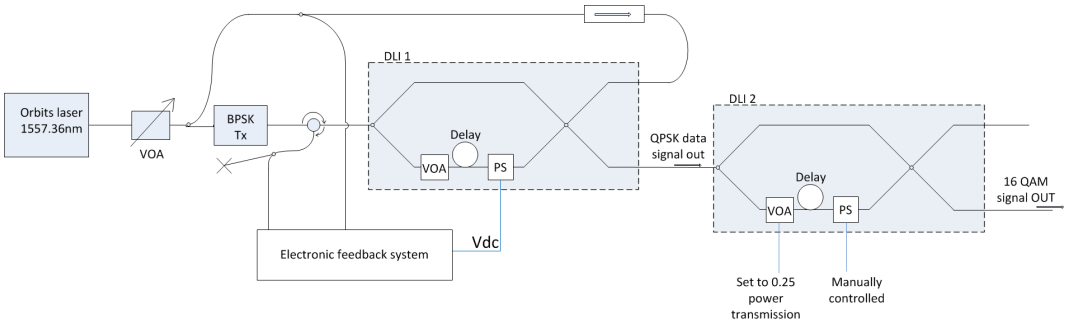

FIGURE 3.14: Full schematic of the 16QAM emulation system.

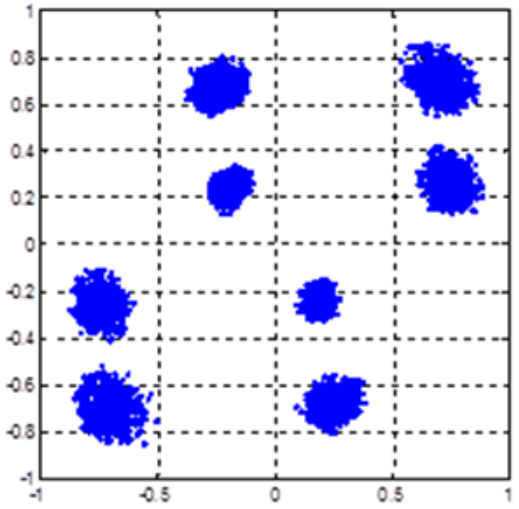

FIGURE 3.15: First attempt at examples of 16-QAM emulation using two DLIs with the same FSR.

shifter of this DLI will have to satisfy $^{n\pi}/_{2}$ where n is an integer value including 0. The value of n will be important for any future experiments to perform BER measurement with the 16-QAM signal as it changes the symbol position. The complete schematic of the two concatenated DLIs is shown in Fig. 3.14. An example of the corresponding constellation diagram is shown in Fig. 3.15. This was the first attempt to generate a 16-QAM signal with both DLIs having the same FSR of 2.5 GHz. Fig. 3.15 does not show a 16-QAM constellation but only eight symbols, implying that only these bit sequences were generated by the concatenated DLIs.

Fig. 3.16 displays the mathematical explanation of the generated bits at each stage in the 16-QAM setup, where the M term represents the binary value of the M^{th} bit in the sequence. Note that for a BPSK signal at 10 Gb/s, the delay that is achieved is of 4 bits as previously discussed. The A6 term is a mathematical representation of the output of the system and is calculated through the summation of the previous terms including the delay induced by each DLI. From the constellation diagram displayed in Fig. 3.15 it is necessary to understand that there are only 8 of the 16 constellation points generated when the induced temporal delay in each DLI is exactly the same. Consider

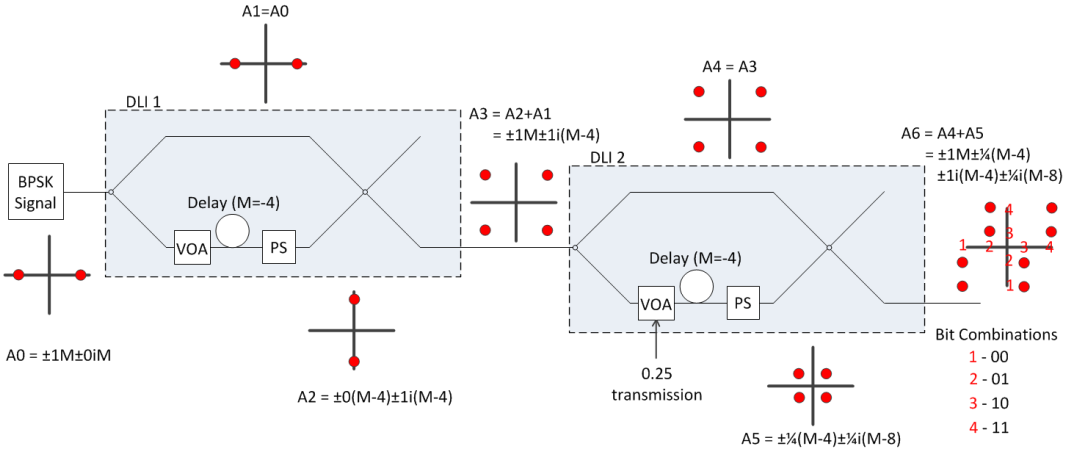

FIGURE 3.16: Reason for 16-QAM constellation truncation.

the output equation for A6. It has been broken into two separate parts, the in-phase axis portion and the quadrature-phase axis portion. For the above example it is possible to generate constellation points at each in-phase point and separately each quadrature point. However, the problem lies when not each point on the in-phase axis can generate all points on the quadrature-phase axis. When the in-phase axis generates a 01 (8th bit 0, 4th bit 1) or 11 (9th bit 1, 5th bit 1) bit combination, the resulting quadrature-phase combination will always be either a 10 or 11 (i.e. the 1st bit is always 1, the 2nd bit can be either 0 or 1) bit combination. In summary, the second bit of the in-phase axis is the same bit as the first of the quadrature-phase axis (shown in the A6 equation as the M-4 bit). This means that half the points on the constellation are missing (as seen in the system output constellation diagram of Fig. 3.16). To ensure this problem is solved these overlapping bits must be separated. This translates into making the FSR of each DLI different, while ensuring an integer multiple of the fixed 2.501 GHz FSR to guarantee complete integer bit jumps. A DLI with a tuneable FSR will now replace the first DLI in Fig. 3.14. The FSR will be set to 10.004 GHz (four times the FSR of the second DLI) to allow a delay length of 1 bit at a repetition rate of 10 GHz. The same step-by-step symbol generation process is shown in Fig. 3.16, incorporating the 1 bit delay of the first DLI and is shown in Fig. 3.17.

Table 3.2 below displays the state table for the output phase and amplitude of the 16-QAM emulator.

Using these different path delays in the two DLIs it was possible to generate the constellation diagram that is displayed in Fig. 3.18 at 40 GBd and 80 GBd, indicating that all 16 points of the QAM signal have been emulated.

A closer observation reveals that not all the symbol transitions occur. For example, the constellation point that represents bit sequence 1100 (singled out as the symbol within the red circle in Fig. 3.19 (left)) appears to have a significantly higher population density over the other constellation points. This would lead to the conclusion that a 11

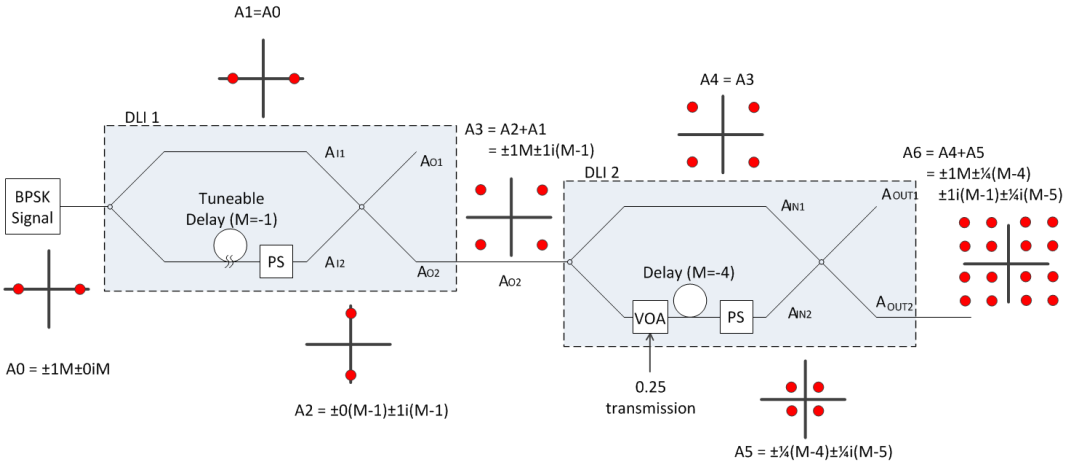

FIGURE 3.17: 16 QAM constellation corrections with tunable DLI (Set to a FSR so M = -1).

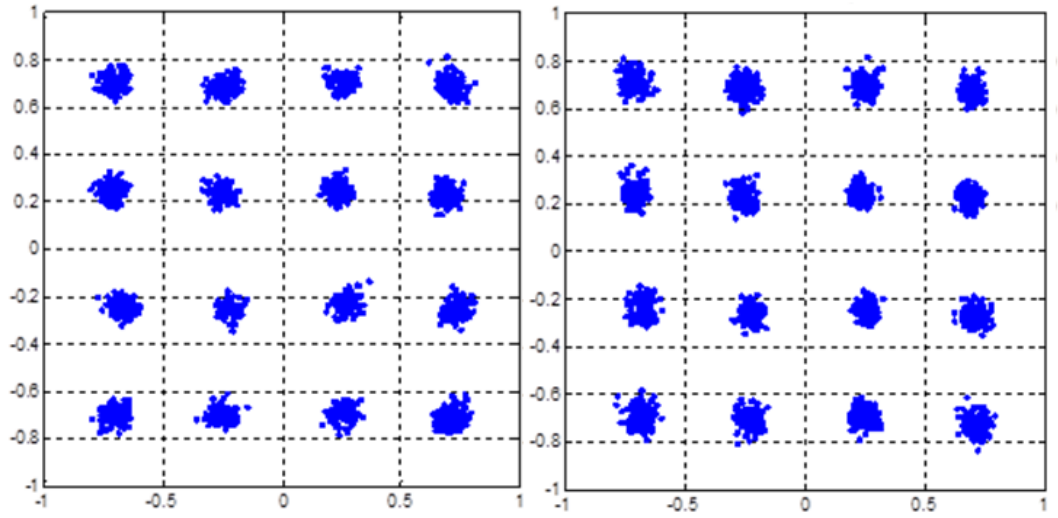

FIGURE 3.18: Emulated 16-QAM constellation at 40 GBd(left) and 80 GBd (right) transitions.

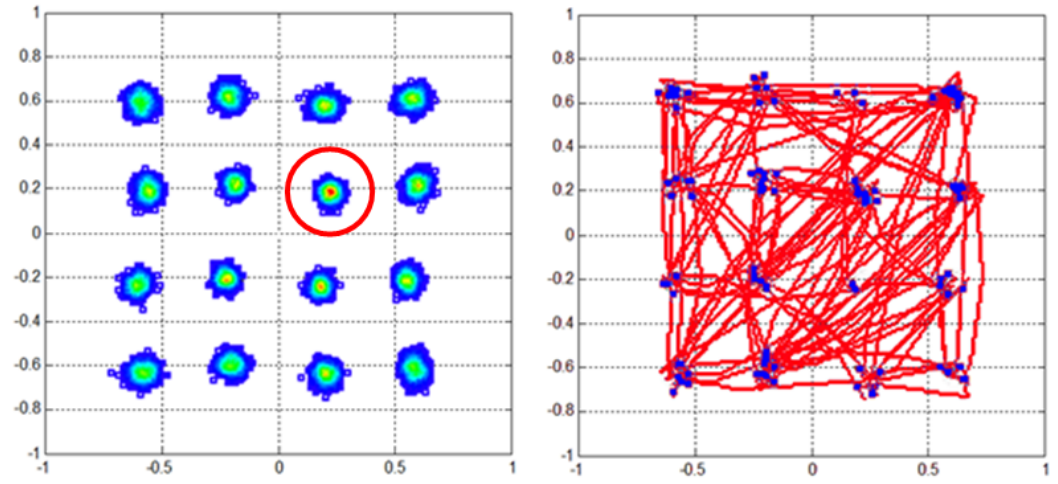

FIGURE 3.19: left, accumulative data and, right, sparse data with transitions for 16-QAM at 40 GBd.

A_{in1} Phase (Rads)	A_{in2} Phase (Rads)	A_{OUT1} Phase Out (Rads)	A_{OUT1} Amplitude Out (referencing input QPSK amplitude as 1)
$\pi\pi$	$\pi\pi$	$^{5\pi}/_{4}$	1.5
$\pi\pi$	$\pi 0$	$\pi + \sin^{-1}(^{1}/_{\sqrt{5}})$	$^{\sqrt{5}}/_{2}$
$\pi\pi$	0π	$^{3\pi}/_{2} - \sin^{-1}(^{1}/_{\sqrt{5}})$	$^{\sqrt{5}}/_{2}$
$\pi\pi$	00	$^{5\pi}/_{4}$	0.5
$\pi 0$	$\pi\pi$	$\pi - \sin^{-1}(^{1}/_{\sqrt{5}})$	$^{\sqrt{5}}/_{2}$
$\pi 0$	$\pi 0$	$^{3\pi}/_{4}$	1.5
$\pi 0$	0π	$^{3\pi}/_{4}$	0.5
$\pi 0$	00	$^{\pi}/_{2} + \sin^{-1}(^{1}/_{\sqrt{5}})$	$^{\sqrt{5}}/_{2}$
0π	$\pi\pi$	$^{3\pi}/_{2} + \sin^{-1}(^{1}/_{\sqrt{5}})$	$^{\sqrt{5}}/_{2}$
0π	$\pi 0$	$^{7\pi}/_{4}$	0.5
0π	0π	$^{7\pi}/_{4}$	1.5
0π	00	$2\pi - \sin^{-1}(^{1}/_{\sqrt{5}})$	$^{\sqrt{5}}/_{2}$
00	$\pi\pi$	$^{\pi}/_{4}$	0.5
00	$\pi 0$	$\sin^{-1}(^{1}/_{\sqrt{5}})$	$^{\sqrt{5}}/_{2}$
00	0π	$^{pi}/_{2} - \sin^{-1}(^{1}/_{\sqrt{5}})$	$^{\sqrt{5}}/_{2}$
00	00	$^{\pi}/_{4}$	1.5

TABLE 3.2: 16-QAM phase and amplitude states.

bit sequence generated from the DLI stage will most often give a 00 bit sequence in the second DLI over any other. To ensure that this was not just a solitary outcome, the test was ran several times with this low symbol count. The same outcome was present with the 1100 constellation point showing the same increased population density compared to other constellation points. The reason that point '1100' appears to have a higher population compared to that of the other symbols could be down to the decorrelation length between the interfered signals. The decorrelation length is only 5 bits, for an adequate pseudo-random bit sequence emulation the decorrelation length would have to half the pseudo-random bit sequence length (at $2^{31} - 1$).

Fig. 3.20 shows the corresponding spectra of the emulated 16-QAM signals for 10 Gb/s, 20 Gb/s and 40 Gb/s, respectively, clearly showing a spectral beating produced by the FSRs of the DLIs. The FSR of the first DLI is 2.501 GHz and can be seen as the small power spectral density variation on the peak of the spectral traces shown in Fig. 3.20. Similarly the FSR of the second DLI, set to 10.004 GHz, can be seen as the sharper, and more pronounced, power spectral density periodic pattern appearing at 10.004 GHz separation intervals.

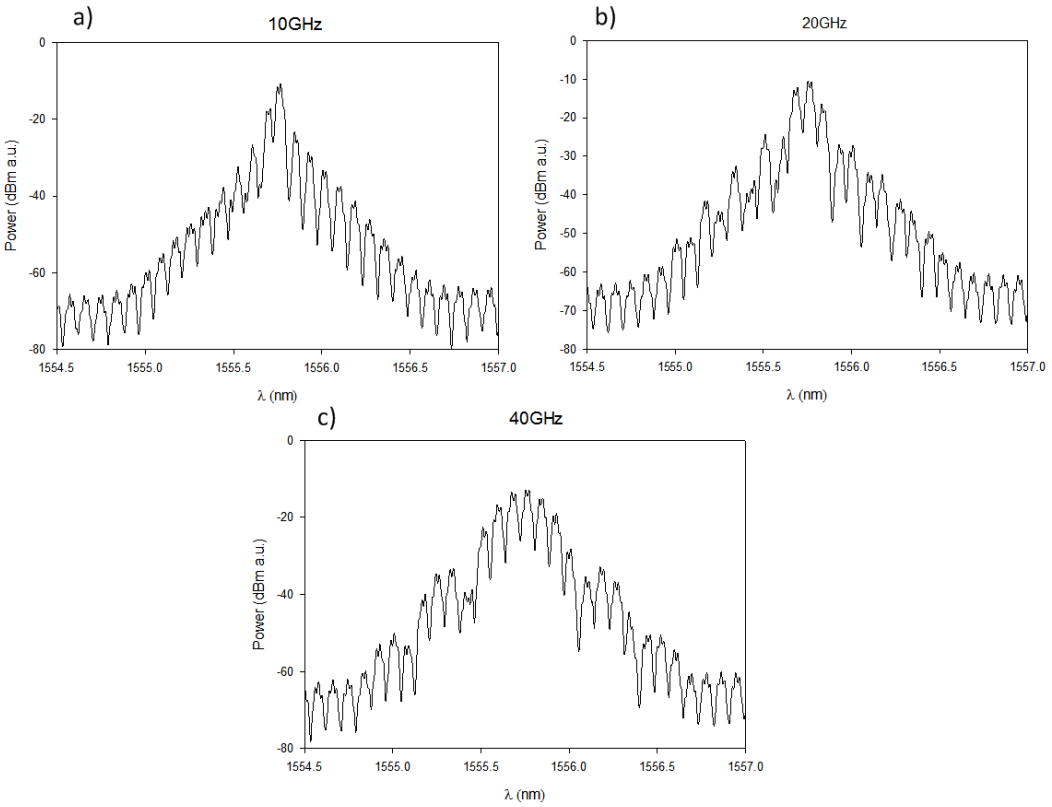

FIGURE 3.20: Spectral traces of 16-QAM signal at a) 10Gb/s, b) 20Gb/s and c) 40Gb/s repetition rates.

3.4 Modulation format conversion employing coherent optical superposition

This section expands on the ideas provided in sections 3.2 and 3.3, where it was shown that a DLI (or concatenation of DLIs) can be used to convert a BPSK signal into a QPSK (or 16-QAM) signal. The main difference highlighted by this section is that following the DLI(s) a temporal gating mechanism is used to remove the redundant overlapping information. Depending on the decorrelation length of the DLI(s) either modulation format conversion or packet compression can be envisaged as two possible applications. It is then possible to interlace two (or more) gated signals and produce an overall signal with higher spectral efficiency.

3.4.1 Operation principle

The operation principle of the passive coherent optical superpositioning scheme is displayed in Fig. 3.21a). A phase and/or amplitude encoded signal with repetition rate $1/\Delta T$ enters a DLI. One of the arms of the DLI has a variable optical attenuator (VOA) the other has a fixed delay of $m\Delta T$, where m is an integer value and depends on the specific application under consideration, followed by a phase shifter (PS). Considering a

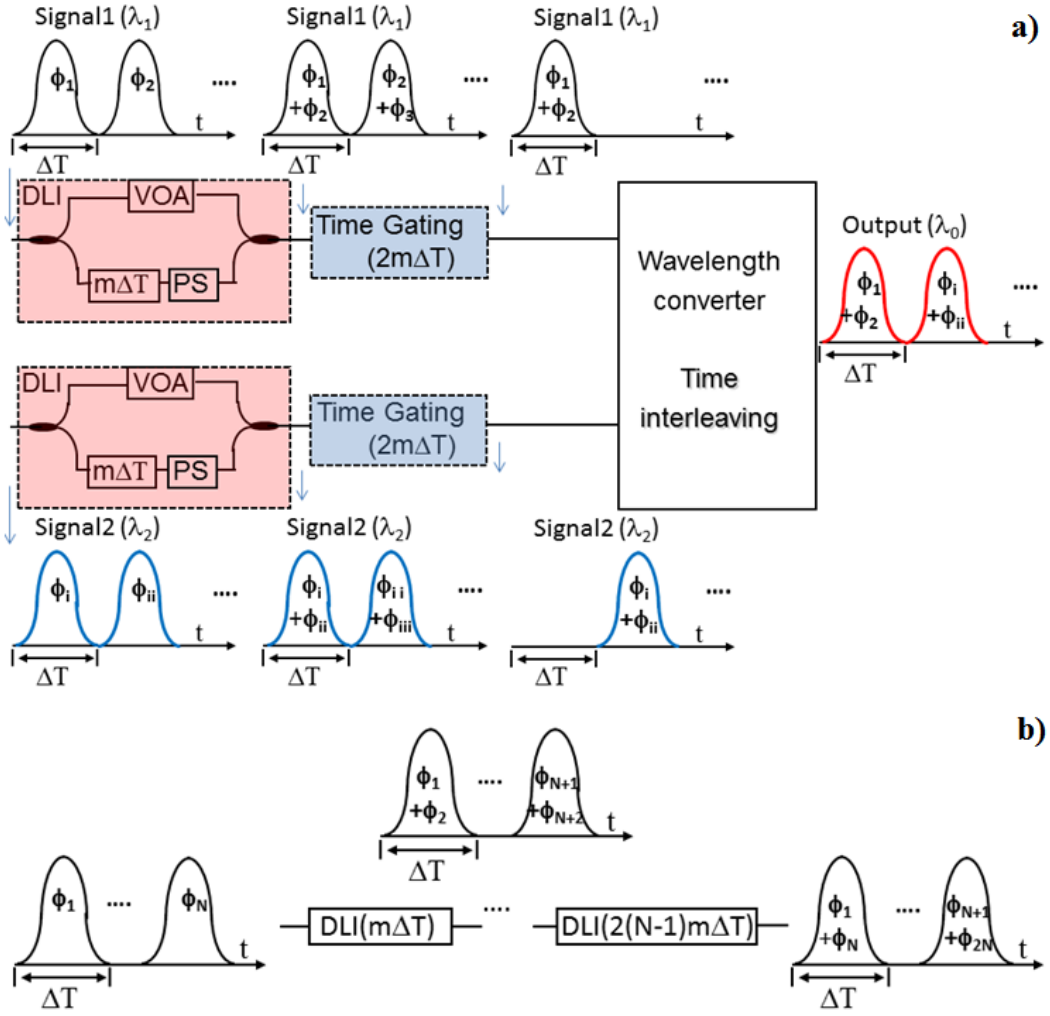

FIGURE 3.21: a)Generalized passive coherent optical superposition operation using DLIs and time gating function, b) Extension to higher spectral efficiencies, higher compression factors and more complex modulation formats.

repetition rate of 10 GBd, for the two cases of format conversion and packet compression the value of m in the fixed delay should be chosen to be of the order of a few bits (hundreds of ps) or in the order of a few hundred bits (hundreds of ns), respectively. The PS and VOA are set according to the modulation format of the input signal. Sections 3.2 and 3.3 describe how, with the correct attenuation and phase shift, it is possible to achieve more complex modulation formats, as reiterated in Fig. 3.21b). In principle, by converting to a more complex modulation format in this manner it is possible to increase the spectral efficiency (SE) of a signal without broadening its spectral content.

A by-product of the coherent addition, required in this technique, is the periodic generation of redundant information. This redundant information needs to be removed to truly achieve an improvement in SE. The generation of the redundant information can be visualised in Signal 1 within Fig. 3.21a), where the second input bit ϕ_2 is contained in both output bits $(\phi_1+\phi_2)$ and $(\phi_2+\phi_3)$. The removal of this redundant information can be performed using a rectangular time-gating function with a period that is two times

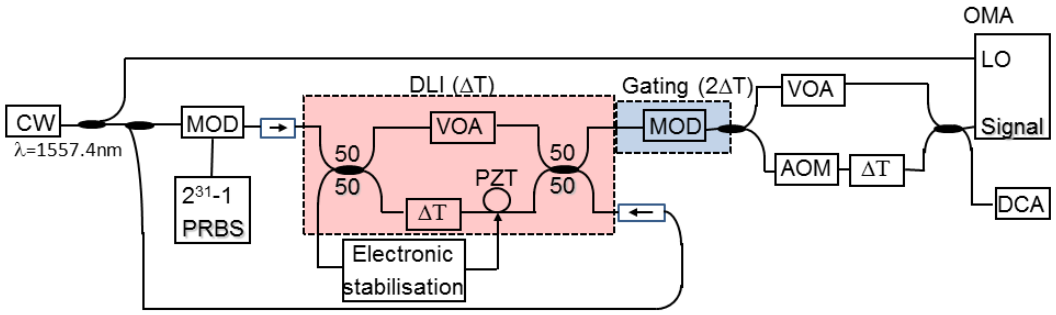

FIGURE 3.22: Experimental set-up of the passive coherent optical superposition scheme. Mod: Intensity modulator, LO: local oscillator.

that of the time delay between the arms of the DLI ($m\Delta T$). After the time gating, the output signal contains all of the information of the input signal however it now occupies half of its space in time. The empty space can be occupied by another signal which has been properly temporally interleaved and wavelength shifted to a common carrier, as shown in Fig. 3.21a). After the empty time slots are correctly filled the combined signals effectively increase the SE and overall transmission capacity. If multiple DLIs are concatenated, for instance to achieve conversion from BPSK to 16-QAM, a single time-gating function can be used at the end. To remove the redundant information the time-gating period has to be two times that of the sum of the various time delays between the two arms of the concatenated DLIs, as a higher temporal compression factor has to be achieved. Multiple signals can then be temporally interleaved (and wavelength converted) to fill the empty time slots. Four BPSK signals, converted to four temporally gated 16-QAM signals, would be required to fully temporally fill a single 16-QAM signal.

3.4.2 Experimental setup and results

The experimental set-up of the passive optical superposition scheme is shown in Fig. 3.22. A narrow-linewidth (<1kHz) CW laser centred at 1557.4 nm was modulated by a Mach-Zehnder modulator, driven by a $2^{31}-1$ pseudorandom bit sequence (PRBS) to obtain a NRZ BPSK (or QPSK) signal. The signal was then inserted into a DLI to generate a QPSK (or 16-QAM) signal at the output. For the format conversion experiment a free-space 400ps (4 symbol) delay between the two arms was used. For the packet compression experiment a fiberized DLI was used which had a 12.8ns (128 symbol) delay between the two arms. Perturbations introduced by thermo-acoustic vibrations were stabilised by a backward propagating stabilisation system similar to that described in section 3.2.2. A synchronously driven amplitude modulator, with repetition rate of $2\Delta T$, was used to provide the rectangular temporal gating function. To effectively emulate the second independent signal the signal after temporal gating was split in two. One portion was delayed and frequency offset from the other. The delay was the same as

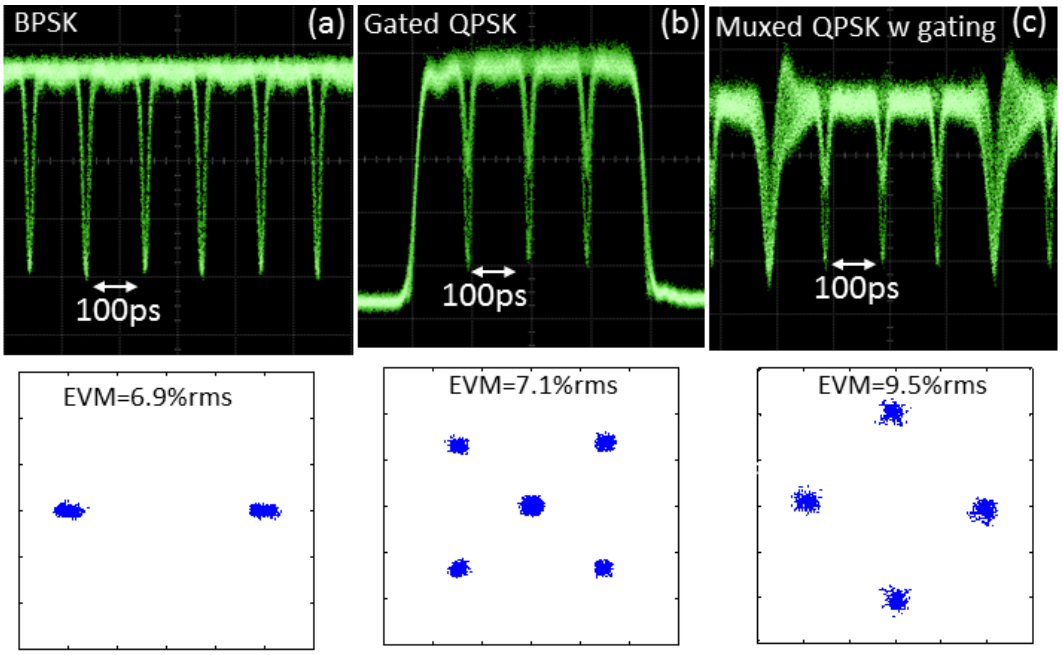

FIGURE 3.23: Eye diagrams and constellation diagrams at various points of the format converter for BPSK as input signals. Scale: 100ps/div.

that used within the DLI (ΔT) and a 30MHz frequency offset was induced by an acousto-optic modulator (AOM), thus ensuring the decorrelation of the two signals before the two portions of the signal were recombined together. For the analysis of the signals a digital communication analyser (DCA) and a homodyne coherent optical receiver were used to observe the eye and constellation diagrams, respectively.

Fig. 3.23 displays the eye and constellation diagrams for various positions through the format conversion process for an input BPSK signal. Fig. 3.23a) displays the input BPSK signal with an EVM of 6.9% rms. Following the temporal multiplexing of the BPSK signal into a QPSK, and after the temporal gating of the redundant symbols the EVM of the gated QPSK signal has marginally increased to 7.1% rms. This rise in EVM can be attributed to the rise/fall time of the gating device, seen best in Fig. 3.23c) as the overshoot at the start of the 4-bit packet lasting for approximately 50ps. The temporally gated sections are represented by the zero point on the constellation diagram in Fig. 3.23b). This empty space can be filled with another temporally gated QPSK signal, as seen in Fig. 3.23c). Again a small increase in EVM to 9.5% rms is observed due to the non-optimal temporal gating which can be observed in the eye diagram as interference between the temporally adjacent packets.

Similar measurements were taken with QPSK as the input optical modulation format, shown in Fig. 3.24. Here the input QPSK signal has an EVM of 6.9% rms, seen in Fig. 3.24a). Fig. 3.24b) displays the temporal multiplexed and gated 16-QAM signal having an EVM increased to 7.3% rms. Again, the input QPSK signal and gated 16-QAM signal contain the same information, however the gated 16-QAM signal occupies half of

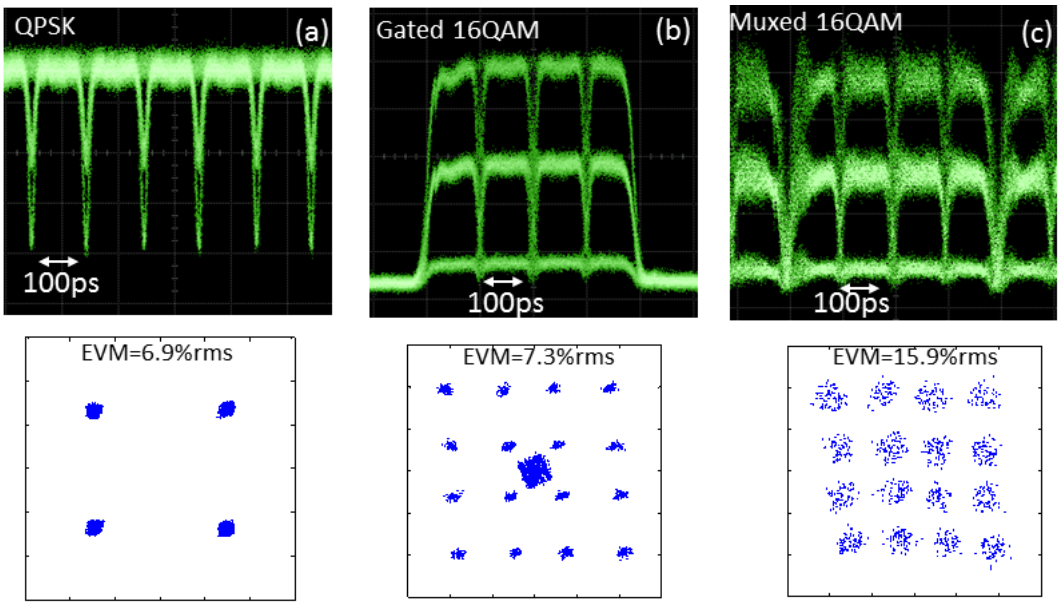

FIGURE 3.24: Eye diagrams and constellation diagrams at various points of the format converter for QPSK as input signals. Scale: 100ps/div.

the time slot of the original input QPSK signal. Another gated 16-QAM signal can be temporally aligned and added to the empty time slots, shown in Fig. 3.24c). Here the subsequent EVM has increased to 15.9% rms.

It is possible to combine these two modulation format conversion processes highlighted in Fig. 3.23 and Fig. 3.24 and convert a BPSK signal into a 16-QAM signal. In this case however four independent signals, each requiring a 1:4 temporal gating, would have to be temporally aligned and added.

By increasing the time delay within the DLI, from 4 symbol to 128 symbol duration, a packet compression scheme was implemented. The optical packet is the fundamental element used within the packet-switched optical network demonstration, where the optical packets are only converted into the electrical domain when they finally reach their destination, thus avoiding the latency inherent to electrical switching methods. Similar measurements to the format conversion case were taken. Fig. 3.25 displays the eye and constellation diagrams of the input BPSK signal, a), the temporally multiplexed QPSK signal, c), the QPSK signal after gating, b), and the gated 16-QAM signal, d), each with an EVM of 6.9% rms, 6.9% rms, 8.9% rms and 10.8% rms, respectively. Again, the time gating response is responsible for the slight compromise in the performance of the system, observable in the increase in EVM after temporal gating.

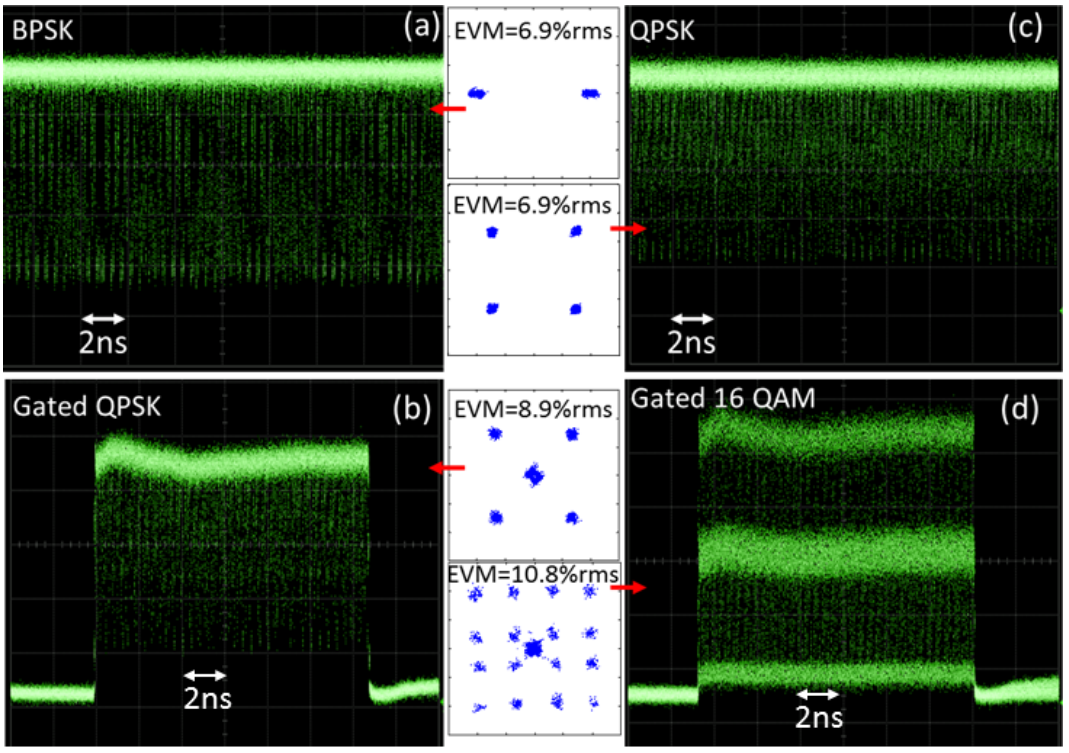

FIGURE 3.25: Eye diagrams and constellation diagrams at various points of the format converter for BPSK and QPSK as input signals. Scale: 2nm/div.

3.5 Broadband phase noise emulation

Phase noise introduced during transmission both from amplified spontaneous emission (ASE) in optical amplifiers and nonlinear interactions among the various transmitted channels and between signal and noise, mainly as a result of Kerr nonlinearity [47, 64], may seriously impair modern telecommunications systems, where the signals modulate both the amplitude and phase of the optical carrier. To mimic real transmission amplitude and phase noise and thus study the performance of processing systems, such as optical regenerators, laboratory experiments have used various noise emulation techniques. The most common one is to use ASE noise coupled with the optical signal to be characterized [65], where both (linear) amplitude and phase noise is generated simultaneously. However, the ability to emulate amplitude and phase noise separately would prove valuable when analyzing the performance of signal processing elements. This has been achieved in the past using phase and/or amplitude modulators driven with sinusoidal waveforms [2], pseudo random bit sequence data patterns [66] or fast-photodetectors detecting ASE at their inputs [24]. The main drawback in using these techniques is that they are inherently limited by the bandwidth of optoelectronic devices, which is typically narrower than the ultrafast processes present in an optical transmission line. In this work, following [67], the detailed characterization of an all-optical technique that mimics the broadband phase noise generated during transmission is presented, by artificially introducing phase noise onto the signal through cross phase modulation in a

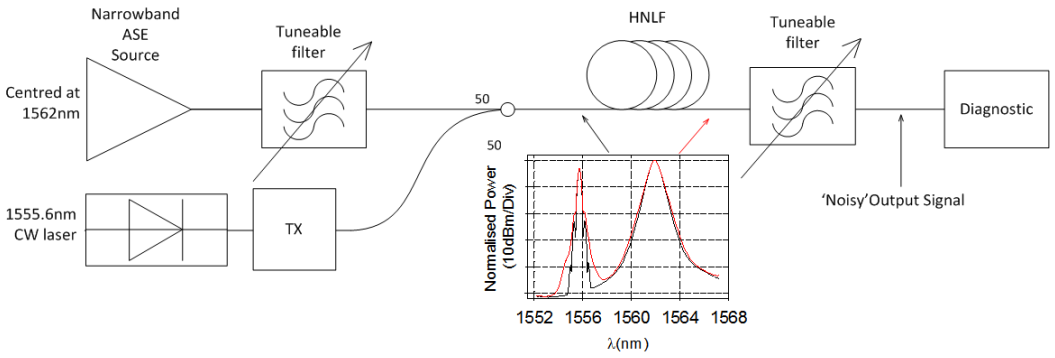

FIGURE 3.26: Experimental setup of the all-optical ASE XPM phase noise emulator. Inset: Optical spectra of 10Gbps DPSK signal and ASE pump at 11dBm at the input (black) and output (red) of the HNLF.

highly nonlinear fibre (HNLF) using an ASE noise source as the pump. This broadband phase noise emulator was used in an all-optical phase regenerator based on a dual pump PSA as described in section 3.5.2.

3.5.1 Experimental setup and results

The experimental setup for the all-optical XPM induced phase noise emulator is shown in Fig. 3.26. A CW laser source at 1555.6 nm was used as a carrier for a 10 Gbps differential phase shift keying (DPSK) signal and amplified up to 8 dBm before being combined with a narrowband ASE source, centered at 1562 nm and with a full width at half maximum (FWHM) of 1 nm. Note that the ASE bandwidth can be easily scaled to accommodate any repetition rate. The signals then co-propagated through 1 km length of HNLF with dispersion, dispersion slope, nonlinear coefficient and attenuation of -17 ps/nm/km, 0.23 ps/nm^2/km, 18 W^{-1}km^{-1} and 2.13 dB/km, respectively. XPM causes the ASE pump amplitude variations, in the temporal domain, to be transferred onto the phase of the signal, manifested as spectral broadening. The inset of Fig. 3.26 shows this spectral broadening of the signal with traces displayed before (black) and after (red) the HNLF. The signal is subsequently filtered and characterized using an OMA. Firstly, as a frame of reference, the DPSK signal was characterized without any ASE noise present (referred to as transmitter floor hereafter). Subsequently, different levels of ASE were considered and some examples of constellation diagrams are plotted in the upper portion of Fig. 3.27.

Fig. 3.27 (bottom) displays the corresponding histograms of the relative amplitude and phase variations for the constellation diagrams represented in Fig. 3.27 (top). Fig. 3.28, shows the phase and amplitude standard deviations as a function of the ASE power levels. Relative to the transmitter output signal, the phase standard deviation increased almost up to five times, while the amplitude noise standard deviation had only doubled.

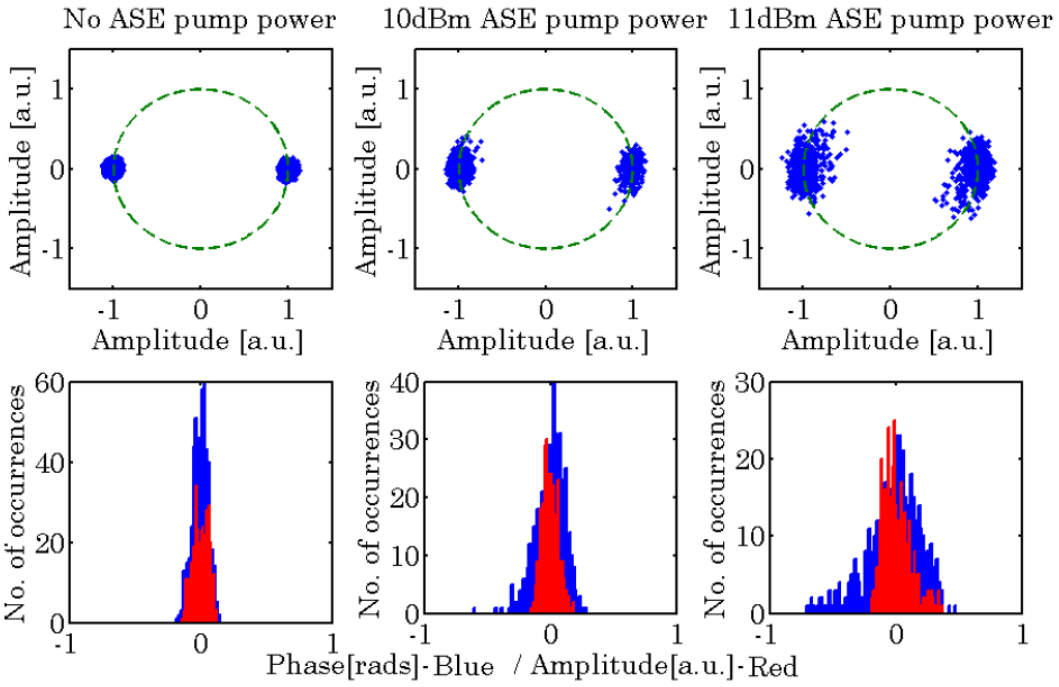

FIGURE 3.27: Upper: Constellation diagrams of the undistorted and distorted 10Gbps signal with (from left to right) two levels of ASE pump powers, respectively. Lower: Corresponding phase (blue) and amplitude (red) histograms.

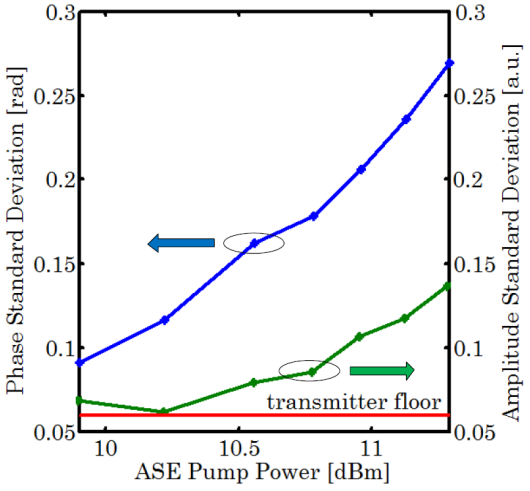

FIGURE 3.28: Standard deviations of the phase and amplitude as a function of ASE pump power, the red line corresponds to no noise added to the system.

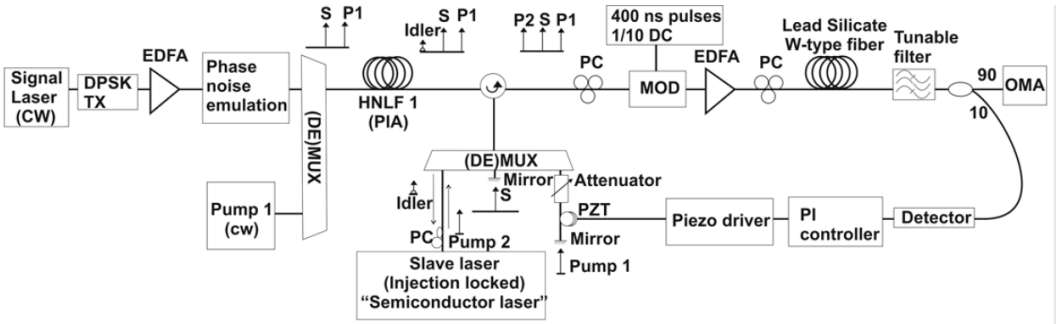

FIGURE 3.29: Experimental setup of the 40Gb/s DPSK phase regenerator, taken from [7].

3.5.2 Application example PSA based optical regenerator

The all-optical XPM induced phase noise emulator was used in an all-optical PSA based phase regenerator for DPSK signals, as described in [7] which details an experiment where the lead contributor was Dr. Mohamed Ettabib. In this experiment a novel W-type ('W' shaped refractive index profile) highly nonlinear lead-silicate fibre was used as the nonlinear material in a dual-pump PSA described in [2]. Fig. 3.29 displays the experimental setup of this DPSK phase regenerator. The data signal was a 40 Gb/s non-return to zero DPSK $2^{31} - 1$ PRBS centered at a wavelength of 1555.64 nm. The signal was coupled with the broadband phase noise emulation mechanism described in the previous section. The distorted signal was then launched into the PSA based phase regenerator, fully described in [2, 7]. I was responsible for the emulation of the phase noise onto the signal in this experiment.

Fig. 3.30 displays the regenerative performance of the W-type PSA via the constellation diagrams of the DPSK data signal before (top) and after (bottom) the regenerator for various noise levels. The signal was first assessed without noise (Fig. 3.30a)), showing similar performance as compared to the case before the regenerator. The broadband phase noise emulation system was used to introduce different amounts of (mainly) phase noise (Fig. 3.30b)-d)). These constellation diagrams clearly show phase noise regeneration with negligible phase-to-amplitude noise conversion.

3.6 Conclusion

The work within this chapter has provided experimental tools to emulate/generate more advanced modulation formats from a seed BPSK signal, which provides modulation format flexibility as an alternative to using expensive dedicated transmitters. This work includes higher modulation format emulation of both QPSK and 16-QAM signals, combined with a detailed demonstration of an opto-electric feedback system successfully used to stabilise the emulated signals. Similarly, modulation format conversion and

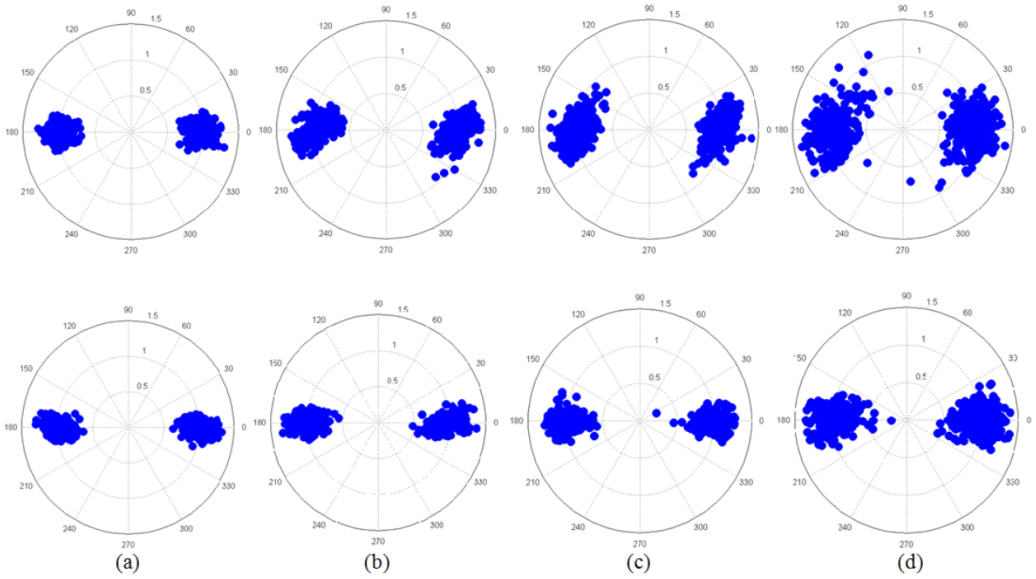

FIGURE 3.30: (a)-(d) Constellation diagrams of the DPSK signal before (top) and after (bottom) regeneration for various noise levels. (a) represents the case of no added noise, taken from [7].

packet compression where achieved, allowing a method to temporally interleave format converted signals to increase signal spectral efficiencies. A broadband phase noise source based on XPM induced in a HNLF, between an ASE noise source at variable bandwidth and a signal, has been used to apply broadband phase noise onto the designated signal. This noise source scheme was used to emulate noise in a novel W-type PSA based all-optical phase regenerator.

Chapter 4

Phase preserving amplitude regenerators

4.1 Introduction

As described in Section 2.9, phase encoded signals, such as those modulated using BPSK, will undergo linear and nonlinear phase and amplitude noise distortion as they propagate through a transmission link, inevitably limiting the transmission reach. Phase-preserving amplitude regenerators are important to process phase encoded signals as they prevent the conversion of amplitude fluctuations to phase fluctuations through the fibre nonlinearities (SPM for example) and thus are able to improve the transmission performance of the signal. Such regenerators have been experimentally demonstrated using a variety of technologies, including saturable absorbers (SAs) [49, 65], schemes using saturated FWM in fibres [68], and OIL [69]. A different technique based on nonlinear amplifying loop mirrors (NALMs) has also been numerically and experimentally demonstrated [53, 70, 71, 72]. All the amplitude regeneration techniques mentioned above must exhibit preservation of the signal phase to be relevant. In this chapter, two examples of amplitude regenerators will be presented and discussed. The first is based on pump saturation of a fibre optical parametric amplifier. A numerical study is reported that considers the feasibility of the regenerator for multi-level amplitude signals, followed by some experimental validations using 10Gbit/s 4-ASK. The second amplitude regenerator is based on OIL and the corresponding experimental results at 10Gbit/s for a BPSK signal, which is transmitted over a 600km link, are reported.

4.2 Multi-level amplitude regenerator (MLAR) based on parametric pump-saturation

In this Section, a numerical study of an amplitude regenerator for multilevel amplitude modulated signals was carried out exploiting saturation in a dual-pump degenerate FWM scheme to create a two-level power transfer function. The validity of the phase preserving nature of the regenerator was investigated through numerical results which were obtained using a split step approach to solve the Nonlinear Schrödinger equation for propagation through the HNLF. A HNLF is a selected length of fibre that has been doped with materials (such as Aluminium or Germanium) and exhibits high $\chi^{(3)}$ based nonlinear interactions. The dispersion parameters are engineered to be minimum at wavelengths near 1550nm, with a low dispersion slope. HNLFs can be also strained to mitigate SBS effects. Finally, an experimental study was conducted to validate the accuracy of the numerical work carried out. Fig. 4.1 displays the constellation diagram of the 4-ASK signal. The inner symbol is a third the electric field amplitude of the outer symbol (as indicated by the 'a' and '3a' terms). In order to achieve an amplitude transfer function that correctly 'squeezes' the inner and outer symbols simultaneously, the plateaus corresponding to these symbols will have to maintain a ratio of 3 times (in field) relative to one another, and nine times (in terms of power). The 9 times plateau separation in power in the linear scale corresponds to a ratio of 9.5 dB in the logarithmic scale and this is what the system presented below is designed to achieve.

4.2.1 Operation principle

In a HNLF based dual-pump degenerate scheme, where the power of the (frequency centred, as seen in the inset of Fig. 4.2) signal is comparable to the (frequency flanking) pumps, the system is said to be working in the pump saturation regime if sufficient nonlinear phase shifts are achieved [73]. Pump depletion is a physical mechanism that will eventually cause the signal power to saturate beyond certain pump power levels. The effects of pump depletion have been studied extensively, for example in [71, 73, 74]. The aim of this numerical study is to predict how it might be possible to achieve such desired transfer functions through four-wave mixing processes in a dual-pump degenerate configuration by varying certain fibre parameters, such as its dispersion and nonlinearity. Fig. 4.2 shows a schematic of the numerical system considered. Two pumps and the signal are coupled and launched into the test HNLF, with variable fibre parameters, before being processed and diagnosed. The input pump powers were fixed at a certain predefined power level (around 17 dBm per pump, depending on the value of the nonlinear coefficient) whereas the signal power was swept from low powers (near 10 dBm) to higher powers (near 35 dBm). For the purpose of this study the practical limitations relating to the onset of SBS were ignored. A two amplitude and two phase

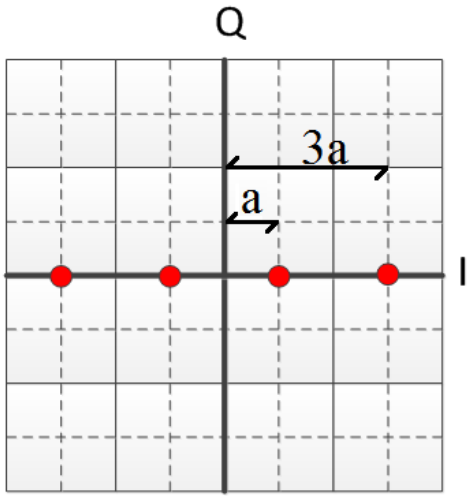

FIGURE 4.1: 4-ASK modulation format.

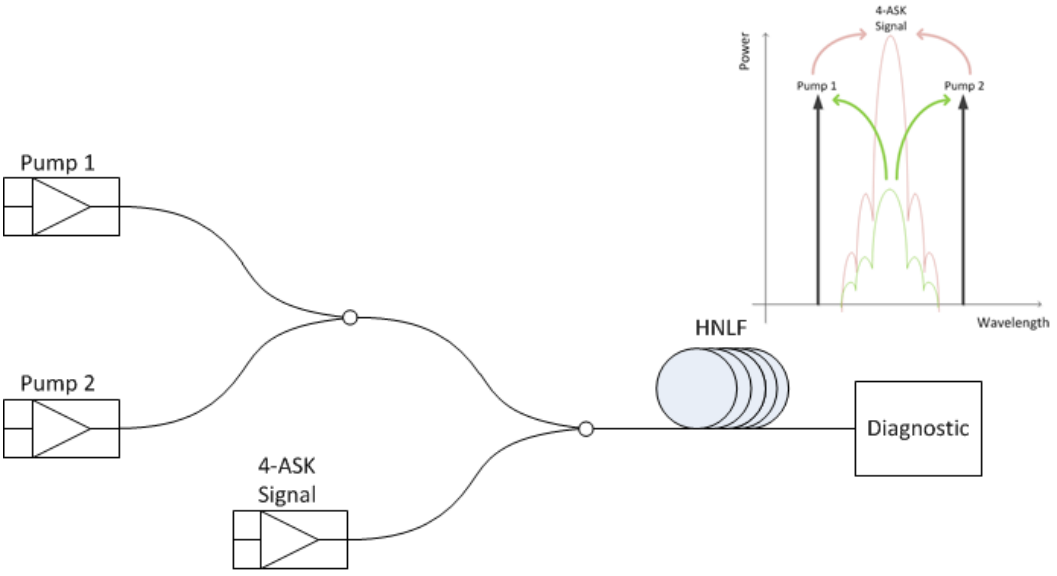

FIGURE 4.2: Numerical simulation setup, inset: Spectral cartoon of dual-pump degenerate PSA.

level signal, which will be denoted as the 4-ASK signal, is used. An example of a 4-ASK signal is shown in Fig. 4.1. An ideal amplitude regenerator should exhibit a two-step transfer function in order to suppress the noise associated to each amplitude level while maintaining the overall separation in amplitude.

Two effects have been exploited to achieve the nonlinear signal power transfer function shown by the blue curve in Fig. 4.3. These effects are: i) relative phase dependent amplification/de-amplification; and ii) pump depletion. This can be visualised in the inset of Fig. 4.2 where de-amplification of the signal is shown in green, and the energy flowing from the signal to the pumps. Conversely, amplification of the signal is shown in pink, where the energy flows from the pumps to the signal. If the signal and pumps

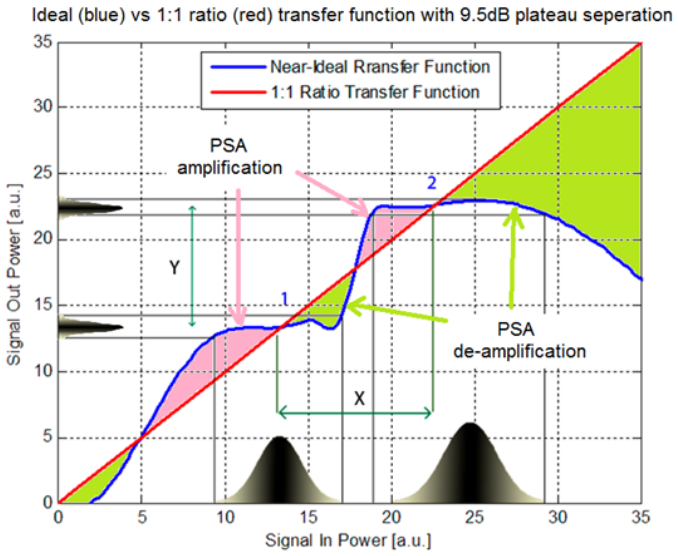

FIGURE 4.3: Quasi-ideal signal power transfer function.

are launched into a HNLF with absolute phases ϕ_s, ϕ_{p1} and ϕ_{p2}, respectively, an idler waveform will be generated at the same signal frequency through the process of FWM. The degenerate idler phase, ϕ_i, will be represented by the summation of the various phases, as displayed below:

$$\phi_i(z) = \phi_{p1}(z) + \phi_{p2}(z) - \phi_s(z) \tag{4.1}$$

Where z is the propagated fibre length. At a set relative phase, the pumps supply different amounts of energy to the signal depending on the operating regime (saturation or small-signal regimes). This translates to a signal gain profile that flattens as the signal peak power increases. Also, as the power of the pumps is reduced the nonlinear phase shift induced on the signal due to XPM is reduced. Since the system is phase sensitive, changing the phase of the signal (either by means of XPM induced phase shift or otherwise) will alter the signal amplification factor. Therefore, this process could help to generate the plateau regions necessary to create the power transfer function shown in Fig. 4.3. Fig. 4.3 displays the regions where energy is transferred from the pumps to the signal (shown in pink) and from the signal to the pumps (shown in green) through the parametric mixing process. The lower level plateau (shown as '1' in Fig. 4.3) represents the plateau for the inner symbols shown in Fig. 4.1, similarly, the higher level plateau (shown as '2' in Fig. 4.3) represents the plateau for the outer symbols shown in Fig. 4.1. The logarithmic power difference between plateau '1' and '2' in the 'signal in power' and 'signal out power' axes are represented by 'X' and 'Y', respectively. As mentioned earlier, both 'X' and 'Y' should equal 9.5 dB in order to maintain the 4-ASK signal and the corresponding differences between the inner and outer symbols. Each plateau should be as flat as possible (in the 'signal out power' axis) to maximise the overall amplitude noise regenerative ability.

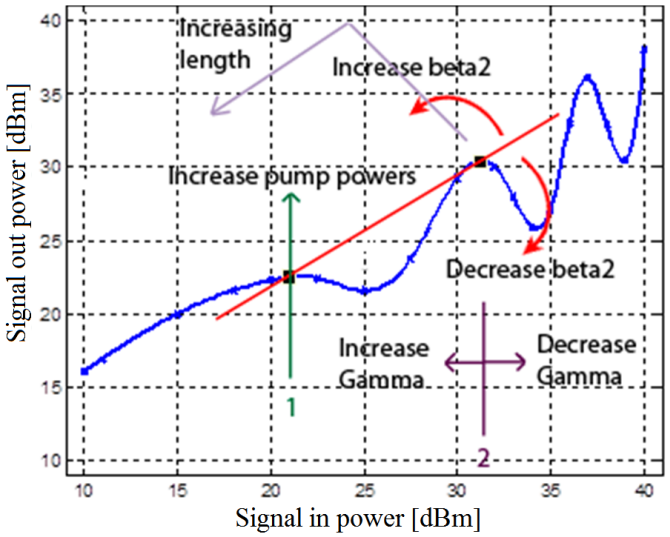

FIGURE 4.4: Visual interpretation of how the signal power transfer function changes as a function of pump power, nonlinear coefficient, dispersion and fibre length.

4.2.2 Results and discussion

A graphic description on how to manipulate the power transfer function of a dual-pump degenerate scheme, as the fibre parameters vary is shown in Fig. 4.4. While fixing all but one of the fibre parameters, the effects of a specific parameter on the overall power transfer function is highlighted, with the position of the first and second plateau regions being the areas of interest. By increasing (decreasing) the flanking pump powers the level of the output power of the first plateau region can be increased (decreased). Alternatively, the input signal power at which the second plateau region is observed can be increased (decreased) by decreasing (increasing) the nonlinear coefficient (gamma in Fig. 4.4). The relative input and output powers of both plateau regions can be skewed by manipulating the value of the group velocity dispersion coefficient (beta2 in Fig. 4.4). Finally, if the length of the HNLF is increased (decreased) the input and output power of the second plateau region can be reduced (increased).

Through a process of fibre parameter optimisation, a power transfer function that exhibits the necessary profile to regenerate a 4-ASK signal was generated. This power transfer function was generated by selectively tailoring the fibre parameters, such that the fibre nonlinear coefficient, group velocity dispersion (GVD) coefficient, length and attenuation were 15 /W/km, 0.1 ps^2/k, 0.7 km and 1 dB/km, respectively. The initial pump powers were set to 17 dBm each at the input of the HNLF. The logarithmic and linear scale power transfer functions are displayed in Fig. 4.5a) and b), respectively.

Fig. 4.5a) shows about a 9.5 dB difference between the first and second plateau regions, both in the Signal In (seen as 'X') and Signal Out (seen as 'Y') axes, while offering relatively flat regions for two broadened input signal power levels. Specifically, the plateau related to the inner symbol covers a 3.5 dB input signal power window while

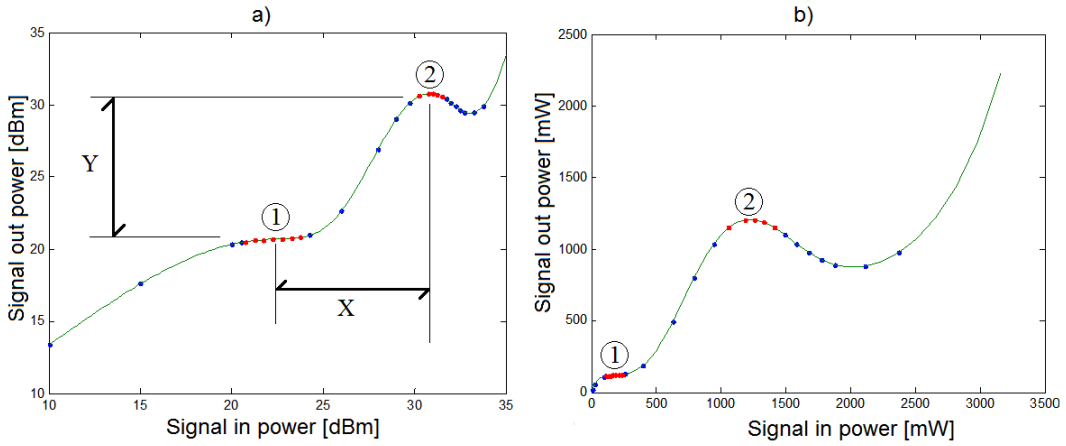

FIGURE 4.5: Signal power transfer function, with a) Logarithmic and b) Linear scales, the red dots represent the inner and outer symbol regions.

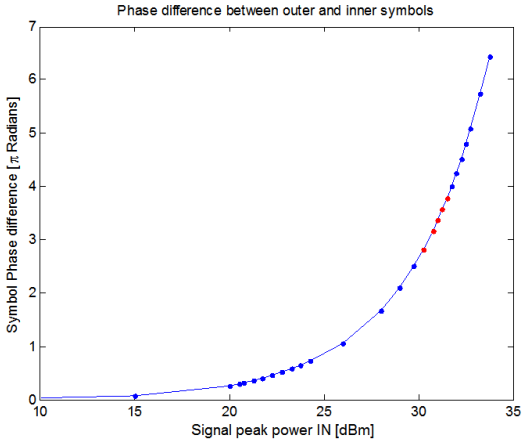

FIGURE 4.6: Inter-symbol phase difference, the red dots represent peak power at which the outer and inner symbols are positioned on the second and first plateau region, respectively.

the plateau related to the outer symbol covers a 1.1 dB input signal power window, as seen by the red dotted regions associated for each plateau region.

As mentioned in the introduction, good amplitude regenerators need to preserve the signal phase, thus, it is important to characterise the relative phase evolution of the inner and outer symbols at the input powers of interest. Considering a 4-ASK signal as the modulating signal, it is possible to test the relative phase response of the signal located on both plateaus simultaneously. If the peak power (power of the outer-most symbols) is aligned to the outermost plateau region of Fig. 4.5, the power of the inner-most symbols will be represented by the first plateau in Fig. 4.5a) (satisfying the mean 9.5 dB difference between the respective symbols). Fig. 4.6 displays the phase difference between the outer and inner symbols (inter-symbol phase difference) for the various swept input signal peak powers. The red dots represent the input power values of the two plateau regions represented in Fig. 4.5a).

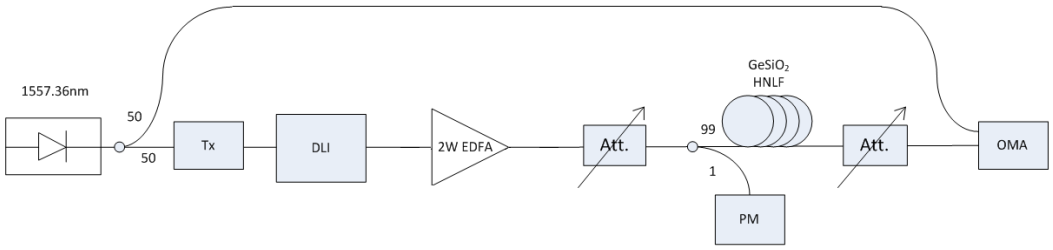

FIGURE 4.7: Experimental/numerical overlap setup

Fig. 4.6 not only shows that there is a large inter-symbol phase difference present within the area of interest (about 1π radians within a signal power change of $\sim$1.25 dB - see the red coloured symbols in the plot) but this phase difference appears to grow rapidly as the signal power increases. This fact would highlight that the proposed multilevel amplitude regenerator would induce major phase penalties causing the pre-coded phase information to be scrambled. Since the aim was to assess the feasibility of the dual-pump PSA system to regenerate the amplitude of the signal with preservation of the information held on its phase, then it is clear that this technique of multilevel amplitude regeneration is not feasible.

4.2.3 Experimental validations

In order to validate the numerical simulations conducted in section 4.2.2, an experiment was carried out. As the phase response of the signal was the main interest of this study, the setup was simplified in the actual experiment. Indeed, the effect of SPM is the contributing factor for the multilevel transfer function profile displayed in Fig. 4.5 and thus can be studied independently without involving the extra complexity of the pump effects. For this reason the pumps were ignored in the experimental setup and only the 4-ASK signal was launched into the HNLF to measure the signal inter-symbol phase difference as a function of its peak power into the fibre. Ignoring the pumps from the system, it is valid to ignore the effects of FMW. The results will be compared to those of a numerical model of the setup, which is shown in Fig. 4.7. Experimentally, an HNLF was selected which had comparable specifications (within the same order of magnitude) to the fibre used to generate the transfer function in Fig. 4.5. This fibre contained a Germanosilicate core and had nonlinear coefficient; dispersion; dispersion slope; length and attenuation of 11.6 /W/km; -0.08 ps/nm/km; 0.018 ps/nm^2/km; 0.3 km and 0.88 dB/km, respectively.

A 1557.36 nm narrow line-width laser was used as the carrier for a BPSK signal at 10 Gbit/s. A DLI was used to convert the modulation format from BSPK to 4-ASK, with a 6 dB attenuation and $k\pi$ phase shift (where k is a integer number) in one of the two DLI arms. The signal was amplified before entering the HNLF. The power of the signal entering the HNLF was measured using a power meter (PM). After the HNLF

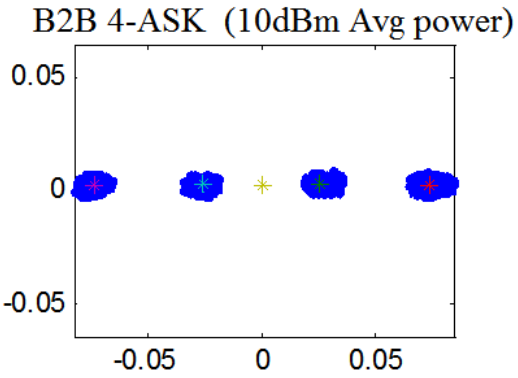

FIGURE 4.8: 4-ASK constellation diagram at 10 dBm average power into the HNLF.

the average power was adjusted to 5 dBm and the signal was launched into a coherent receiver followed by a real-time data acquisition system (Optical Modulation Analyser, OMA). The OMA was used to plot the constellation of the signal at varying levels of average power at the HNLF input. From these constellations the inter-symbol phase difference was calculated. Fig. 4.8 displays the 4-ASK signal at an average power of 10 dBm into the HNLF, where it is highlighted that no SPM-induced phase noise in the corresponding signal is present. It is clear from this figure that all four symbols align, highlighting that if there is any phase shift observed between the inner and outer symbols, at the output of the HNLF, it is a result of SPM within the HNLF.

Fig. 4.9 displays the constellation diagrams of the 4-ASK signal observed at the output of the HNLF for average power levels as detailed above each plot, varying from 15 to 27 dBm. Two effects are evident, as they can be observed on the constellation diagrams in Fig. 4.9, for an increasing signal power, i) amplitude to phase noise conversion and ii) relative misalignment of the outer and inner symbols. In order to calculate the phase difference between the outer and inner symbol phases the mean value is calculated and used. The mean points of each symbol can be seen as the coloured stars located within each symbol in Fig. 4.8. The inter-symbol phase difference was calculated as the angle created between the inner symbol (initially seen to the right of the centre in the 15 dBm trace) and the outer symbol located furthest to the right. The origin was taken as the midpoint between the two inner symbols. The "23 dBm Avg power" centre trace of Fig. 4.9 displays the inter-symbol phase difference as 'ϕ'.

Fig. 4.10 plots both the experimental (blue) and numerical (green) inter-symbol phase differences for peak powers ranging from 17 to 29 dBm, showing very good agreement between them. These experimental results confirm the non-phase preserving nature of the multilevel amplitude regenerator numerically studied in Section 4.2, so no further work was carried out on this type of regenerator.

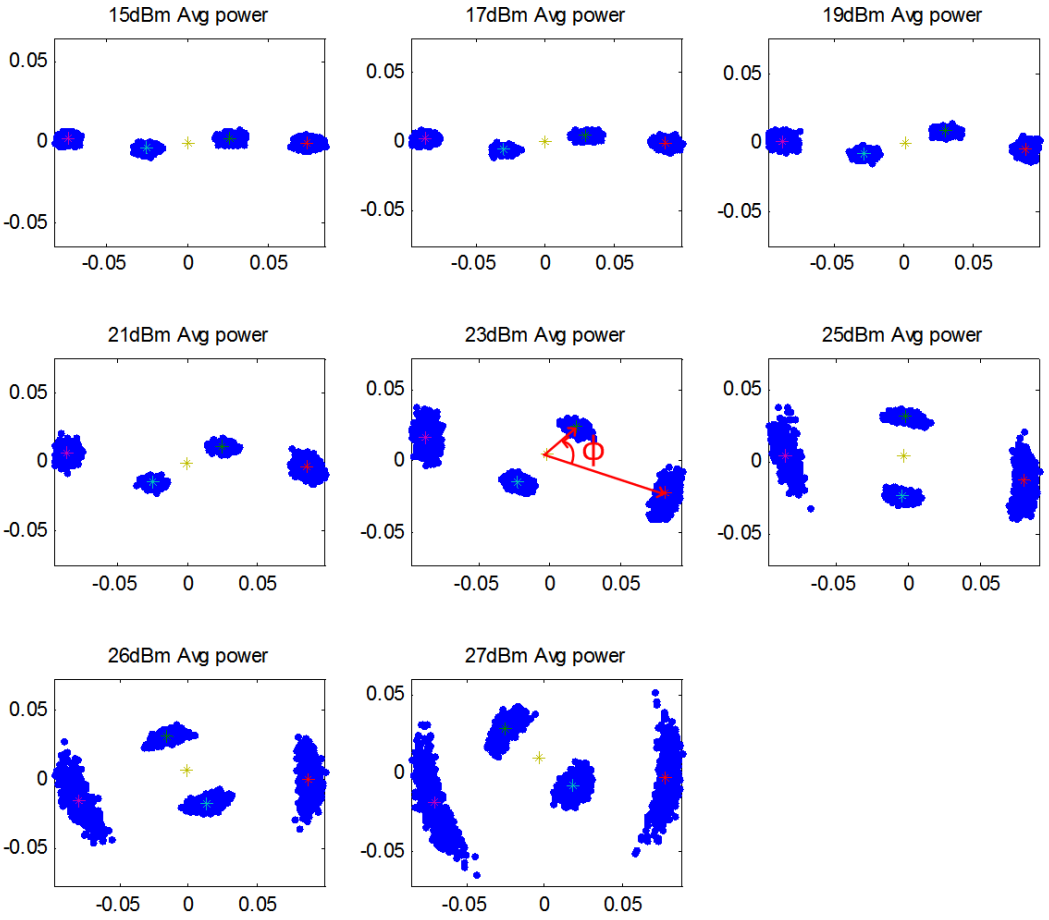

FIGURE 4.9: 4-ASK constellation diagrams for increasing average power into the HNLF.

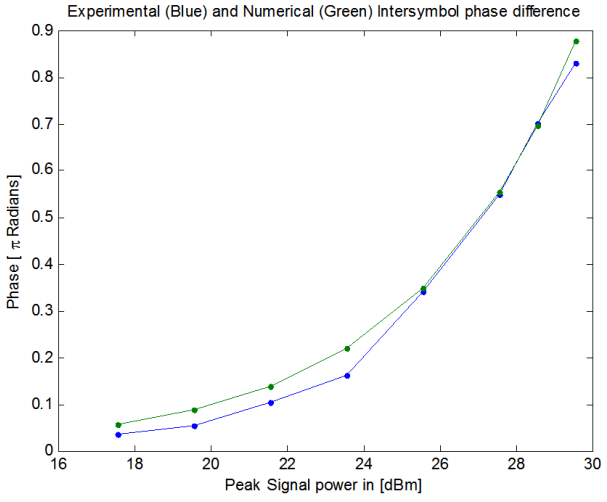

FIGURE 4.10: Correlation between experimental (blue) and numerical (green) intersymbol phase difference.

4.3 Amplitude regenerator based on optical injection locking

In this section, a phase-preserving amplitude regenerator based on an OIL scheme will be experimentally demonstrated. In general, OIL of a slave laser by a master laser allows the optical phase of the slave laser to track any changes in the phase of the master (in our case, this is the data modulation) up to a certain bandwidth, while at the same time amplitude fluctuations are not tracked by the slave laser. As the name suggests, OIL is achieved by injecting some light from the master laser into the slave. Recently, a phase-preserving limiter based on OIL of a semiconductor laser was investigated in [3], predicting that OIL can operate up to rates of 25 Gbaud or higher, thus making this technique promising for removing amplitude noise from fast phase modulated signals while preserving its phase information (data). Importantly, and in contrast to many optical regeneration techniques, OIL effectively amplifies the signal, and could therefore be used as the basis for an amplitude regenerating amplifier. Some preliminary experimental results were reported in [3], where a differential binary phase shift keyed (DBPSK) signal was characterised in terms of demodulated eye-diagrams and bit error ratio (BER) measurements. The signal was degraded either deterministically (by means of an amplitude modulator driven by a 1 GHz sinusoidal wave), or stochastically (by adding ASE noise). In the following section, the nature of the noise at the output of an OIL-based regeneration system will be closely examined and its limitations with respect to the amount of noise it can accommodate at the input will be studied. Finally, the performance of an OIL-based regenerator is used to regenerate a BPSK signal forming part of a more complex wavelength division multiplexed (WDM) system, after this has undergone transmission over 600 km through an installed transmission link.

4.3.1 Characterisation of OIL based regenerator

In the first set of experiments, the performance of the OIL-based regenerator was studied when it was placed at the output of a 10Gbit/s BPSK transmitter operating at 1555.84 nm, as shown in Fig. 4.11(top). The optical signal to noise ratio (OSNR) of the signal at the output of the transmitter could be varied between 20 dB and 12 dB by adding the input from a variable-power ASE source to its output. The resulting signal was then attenuated by a VOA down to -4.6 dBm and after careful adjustment of its polarization, it was launched via a circulator into the slave laser injection-locked through its front facet. The slave laser was a discrete-mode laser and was biased at a current of ∼122 mA, yielding an output power of ∼7 dBm. The injection ratio, defined as the ratio of the power at the output of the slave laser when the bias current was switched on and off respectively was measured as ∼25.4 dB. Fig. 4.12 shows spectral traces of the free-running laser (red curve), and the signal both before (blue curve) and after (green curve)

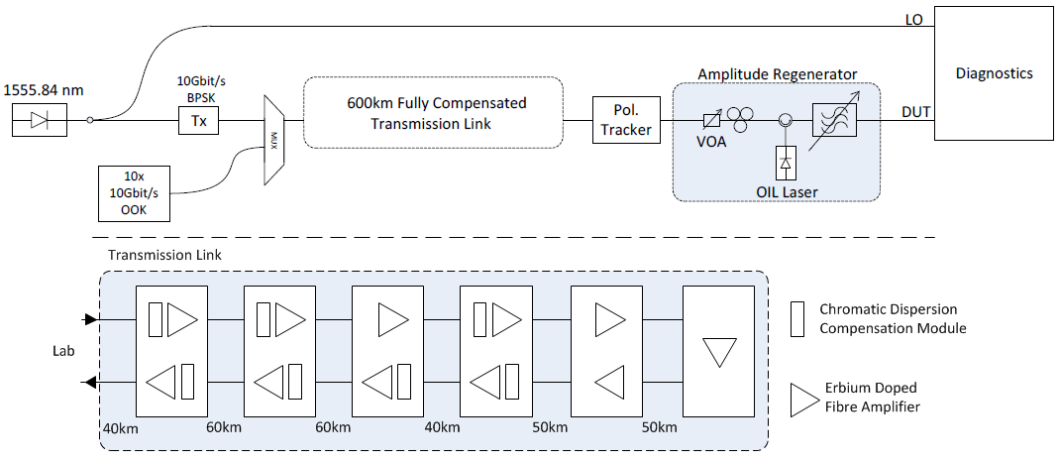

FIGURE 4.11: Transmission setup of the OIL based phase-preserving amplitude regenerator. Lower: Schematic diagram of the 600km dispersion compensated transmission link (red).

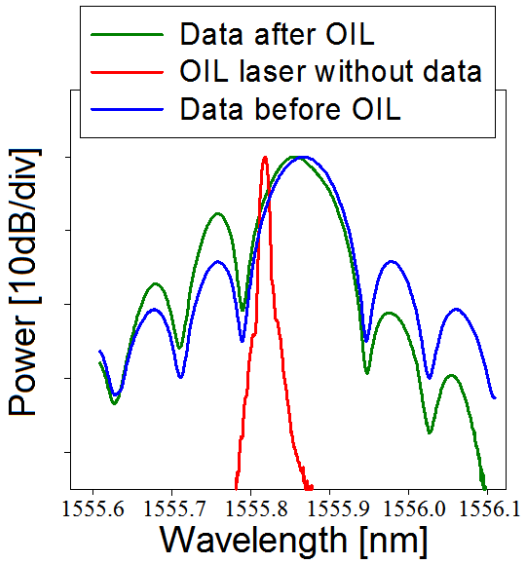

FIGURE 4.12: Normalized signal optical spectral traces of the signal before (blue) and after (green) the OIL laser and of the free-running laser (red).

the injection locked laser. In order to achieve optimal performance, the spectral peak of the free-running laser had to be detuned from the signal wavelength by approximately 6 GHz. As a consequence, the spectrum of the injection locked signal was also upshifted by approximately 2.5 GHz relative to the original signal wavelength. Additionally, the first two spectral side-lobes of the resulting modulated signal exhibited a ∼14 dB power difference, as displayed by the green curve in Fig. 4.12. A super-Gaussian filter was then used, with its central frequency offset towards longer wavelengths, to equalize the side lobes. The OIL signal at the output of the filter displayed by the blue curve in Fig. 4.13. The signals before and after OIL were characterized using an optically pre-amplified coherent receiver followed by a real-time data acquisition system.

As a result of the amplitude noise suppression of OIL, the phase noise at the output

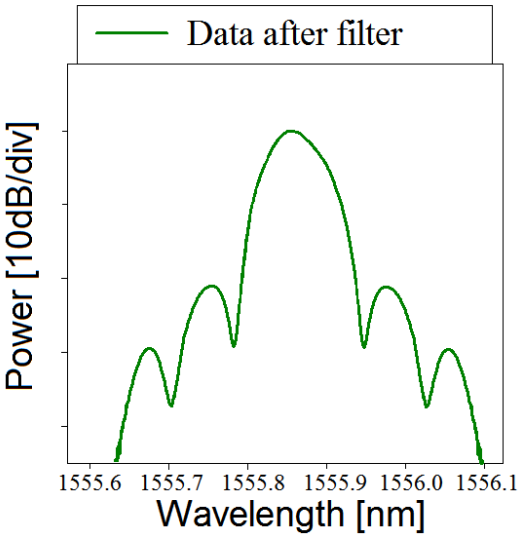

FIGURE 4.13: Normalized signal optical spectral traces of the signal after OIL and after side-lobe equalizing filter.

of the slave laser increases slightly due to an amplitude to phase noise conversion. In order to quantify this effect, the amplitude and phase noise was characterised before and after the OIL-based regenerator for various values of signal OSNR. The results of these measurements are shown in Fig. 4.14a). The performance of OIL as a phase preserving amplitude limiter is confirmed by observing that while the amplitude error (AE) of the input signal increases linearly with deteriorating OSNR, its rms value remains fairly constant after OIL, achieving an amplitude noise reduction of more than a factor of 2. With regard to the phase error (PE), both curves before and after OIL increase for decreasing OSNR. However, the phase noise at the output of the OIL system is slightly higher, due to the amplitude-to-phase noise conversion in the regenerator itself, as highlighted in [3]. Nevertheless, it is interesting to note that the ratio between the values after and before OIL remains fairly constant at ∼1.7, independently of the OSNR value. The degraded signals were also characterized in terms of bit-error ratio curves, as estimated from the real-time data acquisition system. Fig. 4.14b) shows the measured improvement in receiver sensitivity for the various OSNR values at BER=10^{-4} before and after OIL. The OIL-based regenerator consistently allows a sensitivity improvement of ∼0.8-1.1 dB down to a certain OSNR value (in our specific case up to OSNR=14 dB), beyond which point the induced noise is too high for the slave laser to be properly locked and regenerate the noisy signal.

4.3.2 Transmission experiment

The OIL-based regenerator was then placed at the end of a 600 km, fully dispersion compensated, transmission link to assess its performance. The link was an installed fibre loop extending from Southampton to Colchester, and forming part of the UK Aurora

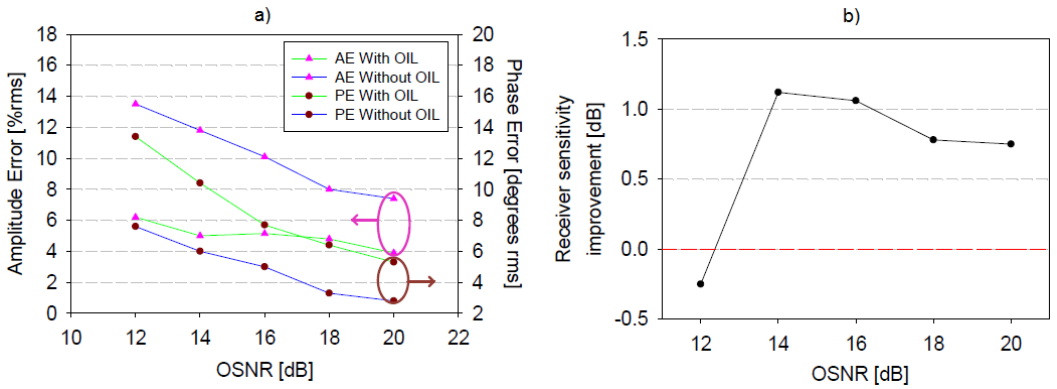

FIGURE 4.14: a) rms amplitude (triangles) and phase (circles) error noise before (blue lines) and after (green lines) the OIL regenerator against OSNR. b) Receiver sensitivity improvement at BER = 10^{-4} against OSNR before and after OIL.

dark fibre network. The link comprised twelve amplified spans, with distances ranging from 40 to 60 km each, as shown in the lower part of Fig. 4.11. The same 10 Gbit/s BPSK signal as above was coupled together with ten other OOK signals, occupying wavelengths from 1550 to 1562 nm, before being launched into the transmission link. An example of a spectral trace observed at the output of the transmission system can be seen in Fig. 4.15. At the end of the transmission link, the OSNR of the BPSK signal was ∼19 dB. To align the state of polarization of the received BPSK signal (master) to that of the discrete-mode (slave) laser a polarization tracker followed by a polarization controller was used. An in-line optical attenuator was also used to ensure the power entering the slave provided optimal performance, with the same power values as in the characterisation experiment. The performance of the OIL-based regenerator was then assessed in terms of constellation diagrams and BER curves. Fig. 4.16 compares BER curves for the signal before transmission (back-to-back (B2B), black circles), with those after 600 km transmission before (blue circles) and after transmission and regeneration (green circles). The BER performance of the signal after regeneration is seen to be similar to the B2B case, with a power penalty improvement of about 1 dB (at BER=10^{-4}) as compared to the case without the regenerator, in agreement with the previous study of ASE-noise induced degradation. The insets on Fig. 4.16 show the constellation diagrams for each case; the rms amplitude and phase error before OIL were 9% and 8.4 degrees, respectively, while after OIL the corresponding values became 3.7% and 9.6 degrees, respectively. Therefore, an amplitude noise reduction of a factor of 2.4 was achieved for a phase noise degradation of just a factor of 1.1. With the Gordon-Mollenauer effect the amplitude noise will be converted into phase noise, so seeing a reduction by a factor of 2.4 in the amplitude noise, even while slightly degrading the phase noise, is still advantageous.

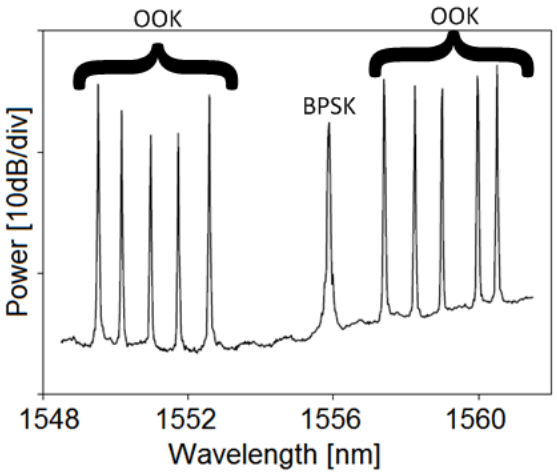

FIGURE 4.15: Example of the optical spectrum after transmission: 10 Gb/s BPSK signal flanked each side by five 10Gb/s OOK signals.

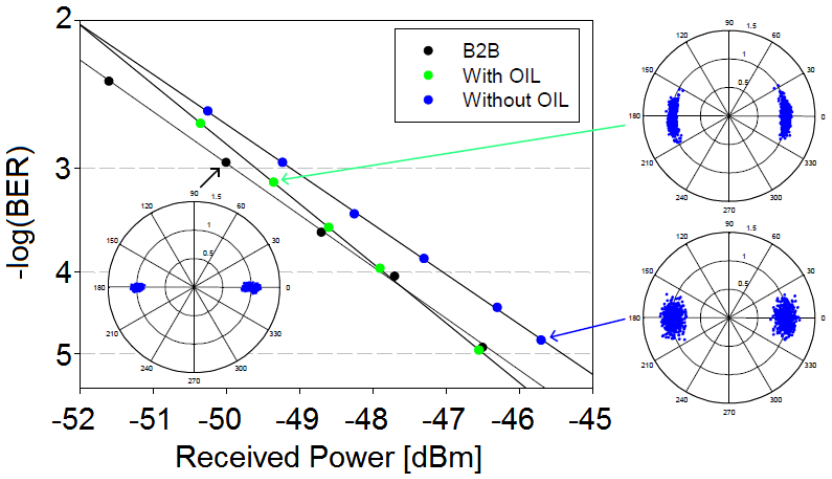

FIGURE 4.16: BER curves for back-to-back (black circles), with (green circles) and without (blue circles) OIL, respectively. Insets show constellation diagrams for each case.

4.4 Conclusion

In this chapter, two phase-preserving amplitude regenerators were discussed and studied. Firstly, a dual pump degenerate PSA configuration has been used to generate a nonlinear signal power transfer function that exhibits a multilevel profile suitable to regenerate the amplitude of a 4-ASK signal. This is achieved by a combination of effects from SPM and XPM induced phase dependent amplification/de-amplification along with the effects of pump depletion. The inter-symbol phase difference of the 4-ASK signal was characterised with the understanding that phase preservation is a requirement. Due to the influence of both SPM and XPM on the signal field, there was an unacceptable degree of inter-symbol phase difference observed while operating within the plateau

regions, making this scheme unfeasible for this purpose. The experimental validation results are in good agreement with the corresponding numerical study.

Secondly, the noise response of an OIL-based amplitude regenerator was characterized for various values of OSNR of the master signal in a back to back configuration. After regeneration, a reduction in the rms amplitude noise by a factor of 2 was achieved, while the rms phase noise deteriorated only by a factor of 1.1, for master signal OSNR values between 20 dB and 14 dB. Receiver sensitivity improvements up to 1 dB (at BER $=10^{-4}$) for the same OSNR values were achieved. The performance of the regenerator was subsequently assessed in a 600 km installed link offering approximately a 1 dB power penalty improvement (at BER=10^{-4}) as compared to its output without regeneration.

Chapter 5

Demonstrations of phase regenerators using high-order harmonics

5.1 Introduction

This chapter includes work from two main areas. Firstly, a detailed study into wavelength converting PSA-based phase regeneration is proposed and demonstrated, where static and dynamic (with data) characterisations are experimentally, numerically and analytically conducted. Secondly, a novel simultaneous amplitude and phase regenerator is discussed. Results are obtained with regard to numerical and analytical measurements for BPSK and QPSK modulation formats.

5.2 Wavelength converting PSA-based phase regenerator

5.2.1 Introduction

For the case of 4-level phase quantisation (as applicable to QPSK signals), PSA-based schemes typically involve the coherent addition of the conjugated third harmonic photons to the original signal in a dual pump configuration [75]. In this chapter a novel, idler-free, PSA scheme is introduced and demonstrated, which coherently adds the conjugated signal photons to that of the generated third harmonic photons, while in the process wavelength converting and phase conjugating the original signal to the spectral position of the generated third harmonic. The use of a different wavelength to the original signal allows independent control of the relative power weights of the conjugated signal and third phase harmonic, achieving phase squeezing over a variety of operating

powers, potentially making this scheme a particularly low power solution for phase regeneration whilst offering a compact, single nonlinear stage setup (as the generation of the third harmonic and the conjugated signal happen in the same HNLF). Furthermore, it is very interesting to note that for any signal-pump power ratio (provided there is enough OSNR), it is always possible to control the harmonic mixing coefficient by varying the power of the second pump. In this sub-chapter the operation principle of the scheme and the corresponding implemented system will be proposed and discussed. Firstly, the wavelength converting, idler free scheme is statically characterized in terms of numerical (used to aid the experimental work with designed signal pump(s) power ratios) and experimental (gathered by Kyle Bottrill) output phase and amplitude transfer functions versus input phase for various harmonic mixing coefficients, and the corresponding spectral traces are reported. Secondly, the system is dynamically characterized: i) a numerical (which solves the NLSE using the SS-FM) based Error Vector Magnitude (EVM) study based on the constellation diagrams are reported for various phase noise values of an input 10 GBaud QPSK signal and for different mixing coefficients and total powers into the HNLF ii) and experimental constellation diagrams and corresponding BER curves for a 10 GBaud QPSK signal are reported for various input phase noise levels and for a mixing coefficient and total launched power into the HNLF similar to the ones investigated in the numerical study.

5.2.2 Operation principle

Typical PSA-based schemes for QPSK signal (four-level) phase regeneration, exploit two independent non-linear processing stages [75][76]. The first stage, depicted in Fig. 5.1a) left, consists of a degenerate, single pump FWM scheme, generating the higher order harmonics (third harmonic) phase locked to the signal (this is referred to as a phase-insenstive amplifier); the second stage, depicted in Fig.5.1a) right, consists of a dual pump FWM scheme, where the third harmonic is mixed back to the original signal. A more compact variant of the scheme is proposed in [24], shown in Fig. 5.1b) and referred to as the idler-free scheme, where the first and second stage are combined into a single HNLF. In this case the two input pumps are used with their power tuned so as to simultaneously produce the third harmonic and coherently add it back into the original signal. However, this scheme requires high pump and signal powers in order to generate and subsequently mix back the third harmonic onto the signal, and very specific pump-to-signal power ratios. The proposed wavelength-converting idler-free scheme is displayed in Fig. 5.1c). The set-up is similar to the idler-free scheme, but in this case instead of producing the third harmonic and coherently adding its conjugate to the original signal, the phase conjugated signal is coherently added to the third harmonic. As a consequence, the regenerated signal is formed at the wavelength of the third phase harmonic and is phase conjugated. The coherent addition of the conjugated signal photons with the third harmonic can be independently controlled via the initial power

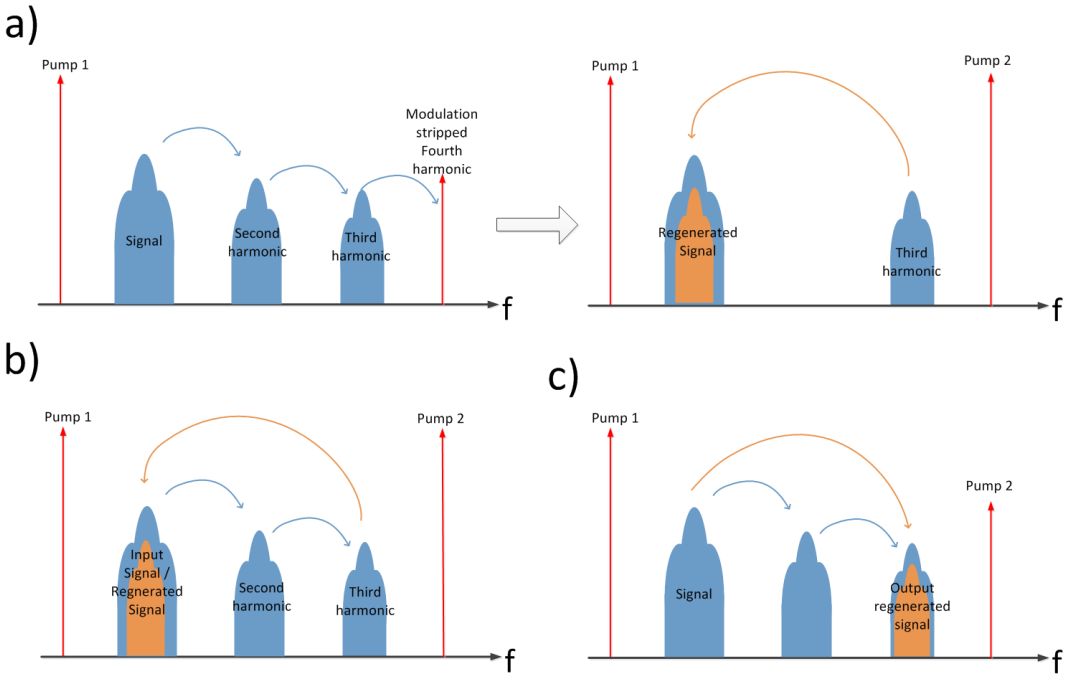

FIGURE 5.1: Spectral diagram of various phase regenerator, a) Dual stage scheme, b) Idler free scheme, and c) Wavelength converted idler free scheme

of the secondary pump (Pump 2), which is independent from the generation of the third phase harmonic. Therefore, provided that the final signal retains sufficient OSNR, for any input pump 1 to signal power ratio used to generate the third phase harmonic, any level of phase squeezing can be achieved by adjusting the initial power of Pump 2, potentially allowing lower pump powers to be used compared to the standard idler-free scheme. It is important to note that this PSA scheme can be followed by a wavelength converter to bring back the phase regenerated signal to the original input frequency and undo the phase conjugation that it has underdone. This has been subsequently demonstrated in [8], where I am responsible for the system concept and Kyle Bottrill was responsible for all of the experimental work. However, in the rest of this chapter, the scheme will be considered as a wavelength-converting phase regenerator only. This section compares and discusses both numerical and experimental work.

5.2.3 Numerical / Experimental Setup

The main goal of this section was to be able to obtain a wavelength-converting idler-free phase regenerator system for a QPSK signal. In order to achieve this goal static numerical and experimental studies were firstly performed.

The corresponding setup is shown in Fig. 5.2. Three phase locked CWs at 1556.9 (pump 1), 1557.36 (signal) and 1558.25 nm (pump 2) are coupled together. Experimentally, the phase locking among the three CWs were obtained by injecting a CW seed at 1557.36

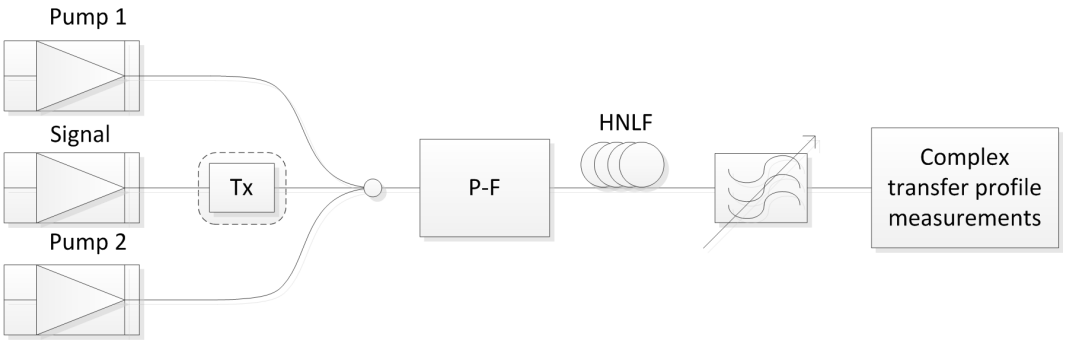

FIGURE 5.2: Numerical and experimental setup for the Wavelength-converting, idler free phase quantiser

nm into an overdriven (with a 40 GHz sinusoidal signal) Mach-Zehnder modulator producing a phase locked optical comb with 40 GHz line spacing. The comb was then fed into a programmable filter (P-F), which was used to set the relevant amplitude offsets, apply an incremental phase shift to the signal and filter out any undesired harmonics. The three waves were then injected into a HNLF with dispersion, dispersion slope, zero dispersion wavelength, nonlinear coefficient, linear loss and length of -0.08ps/nm/km, 0.018ps/nm^2/km, 1553nm, 11.6/W/km, 0.88dB/km and 0.3 km, respectively. Numerically, the output of the third harmonic at 1557.9 nm was filtered and characterized both in terms of phase and amplitude as the signal phase was varied. Experimentally, the same characterization was carried out; in particular, after the HNLF, a 3dB coupler was used to split the output optical waves, such that simultaneous power and phase measurements of the phase quantiser were taken. The relative power measurements were read from an optical spectrum analyser (OSA), while the phase measurements were carried out using a technique that will be described in Appendix B. To ensure a full phase characterisation, the phase and power measurements were conducted for 60 individual steps of input phase (applied to the signal by the P-F) from 0 to 2π radians. The input signal and pump powers were varied to achieve a variety of phase and amplitude transfer functions, and three of these cases are discussed in the following section.

5.2.4 Numerical, Experimental and analytical convergence

Within this section the experimental, numerical and analytical results for the static characterization of the phase regenerator are discussed. The system was tested with three different input power levels. The phase transfer functions generated by the experimental data are plotted against numerical and analytical data. The analytical equation that was used is the following:

$$A_{out}e^{i\phi_{out}t} = e^{-i\phi_{in}t} + m\left(e^{3i\phi_{in}t}\right) \tag{5.1}$$

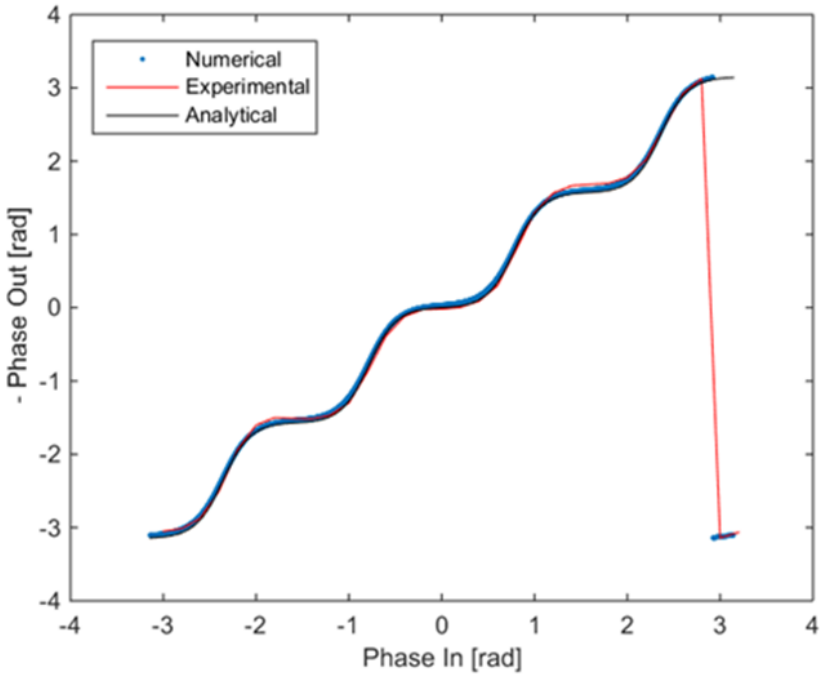

FIGURE 5.3: Phase transfer function of numerical, experimental and analytical in blue dots, red line and black line respectively, with an 'm' value of 0.3.

Where ϕ_{in} is the input signal phase, m is the harmonic mixing coefficient (defined as the ratio of the third harmonic added to that of the conjugated signal), A_{out} and ϕ_{out} are the output amplitude and phase of the regenerated signal, respectively. For the first characterization the experimental input power of P1, signal and P2 were 25 dBm, 23 dBm and 12.5 dBm, respectively. The corresponding numerical power values that had to be used to achieve a good match with the experimental results for P1, S and P2 were 21 dBm, 19 dBm and 8.5 dBm, respectively. The 4 dB power difference between the experimental and numerical values can be partially attributed to multiple potential effects: ASE noise at the output of the EDFA, splice losses in the HNLF, possible fluctuation of the zero dispersion wavelength of the HNLF and potential misalignment of the polarizations of the various waves. While the absolute power budget is relatively different, it is important to note that the power ratios are exactly the same between the experimental and numerical results. Fig. 5.3 displays the experimental (red), numerical (blue) and analytical (black) phase transfer functions. To easily compare with previous results the y-axis (output phase) has been inverted, since the regenerated wavelength-converted signal has the conjugate phase of the original signal. For the analytic fit a harmonic mixing coefficient of 0.3 was used.

Fig. 5.3 represents the phase transfer function that (approximately) has a zero gradient at the four input phases of 0 ,$\pi/2$, π and $3\pi/2$ radians as expected from [77]. As it will be clearer later in this section, this phase transfer function is the optimal configuration for phase regeneration up to a critical amount of phase noise, which coincides with the flat phase range of the curve. After this critical phase noise level it becomes advantageous

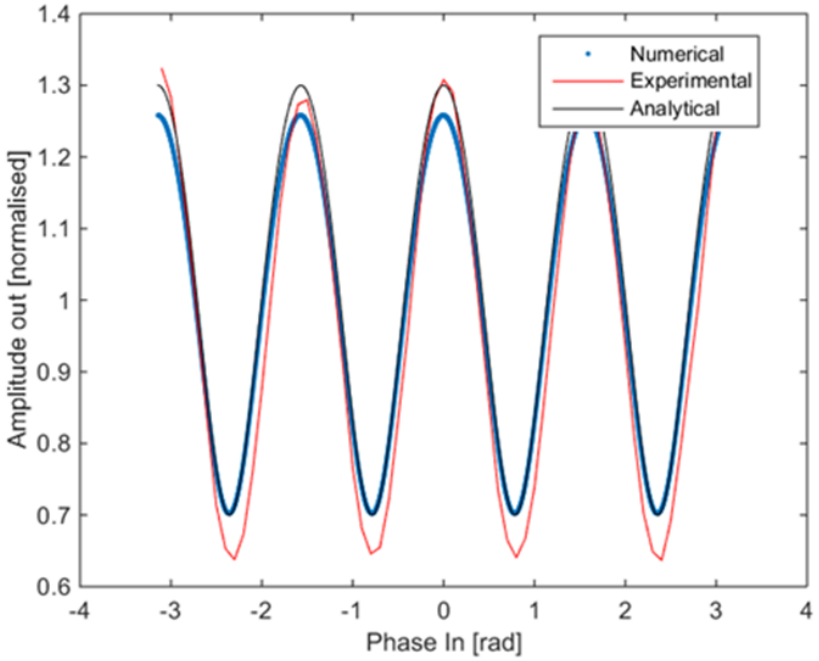

FIGURE 5.4: Output amplitude vs Input phase for numerical, experimental and analytical in blue, red and black, respectively, with an 'm' value of 0.3.

to increase the harmonic mixing coefficient, resulting in a negative gradient at the input phase values of 0 ,$\pi/2$, π and $3\pi/2$ radians, to compensate for the increased phase noise. Fig. 5.4 displays the normalised output amplitude versus the input phase. A peaked cosine-shaped amplitude response is displayed for each numerical, analytical and experimental case. There is a small discrepancy (<10%) with the amplitude values between the experimental and numerical curves.

The same experiment was repeated for a higher harmonic mixing coefficient by simply reducing the power of P2 by 3.5 dB. In the experiment (simulation) this corresponded to setting P2 to 9 dBm (4 dBm). This equates to a 1dB power ratio increase between experimental and numerical power ratio values.

Fig. 5.5 displays the phase transfer function for the experimental (red), numerical (blue) and analytical (black) curves corresponding to a harmonic mixing coefficient of 0.47. After the critical phase noise level (best regenerated by a system operating such that there is a zero gradient at output for input phases of 0, $\pi/2$, π and $3\pi/2$ radians), any additional phase noise will result in the optimal phase quantisation requiring higher harmonic mixing coefficients (as with the following two examples).

Fig. 5.6 displays the normalised output amplitude versus the input phase. There is good agreement with the numerical and experimental data.

Fig. 5.7 displays the phase transfer function for the experimental (red), numerical (blue) and analytical (black) curve for a harmonic mixing coefficient of 0.7. The numerical power value of P2 is 1 dBm. This equates to a 1 dB power ratio increase between the

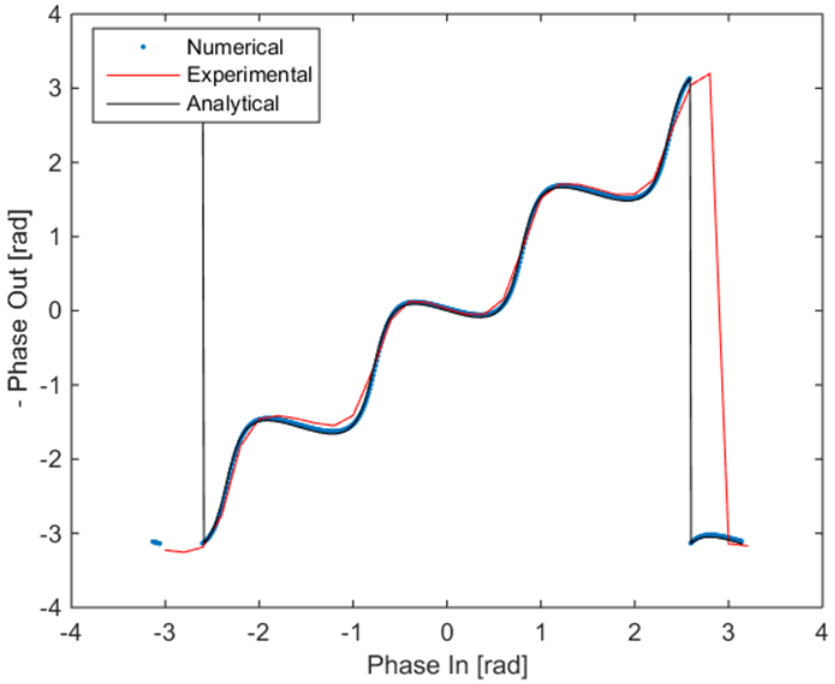

FIGURE 5.5: Phase transfer function of numerical, experimental and analytical in blue, red and black, respectively, with an 'm' value of 0.47.

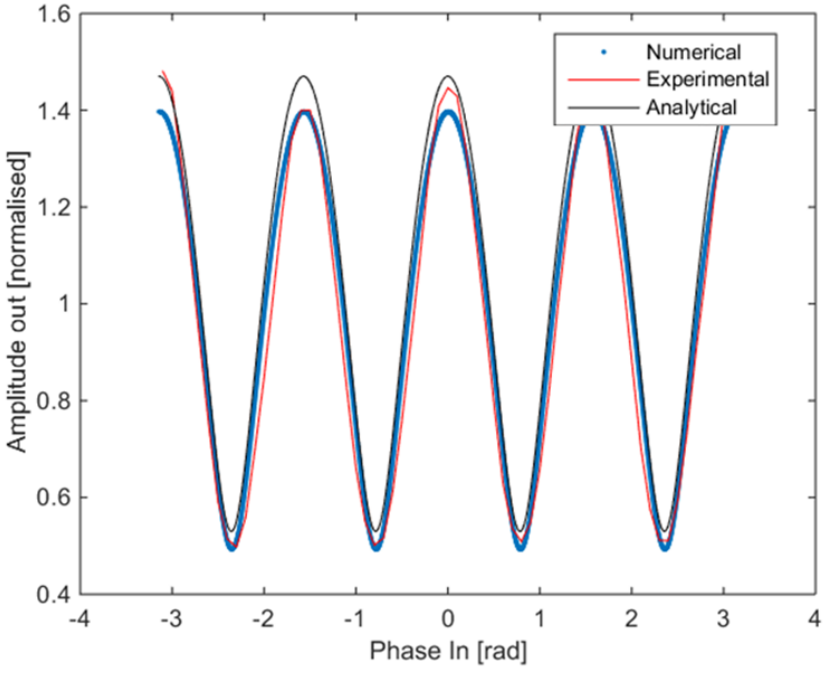

FIGURE 5.6: Output amplitude vs Input phase for numerical, experimental and analytical in blue, red and black, respectively, with an 'm' value of 0.47.

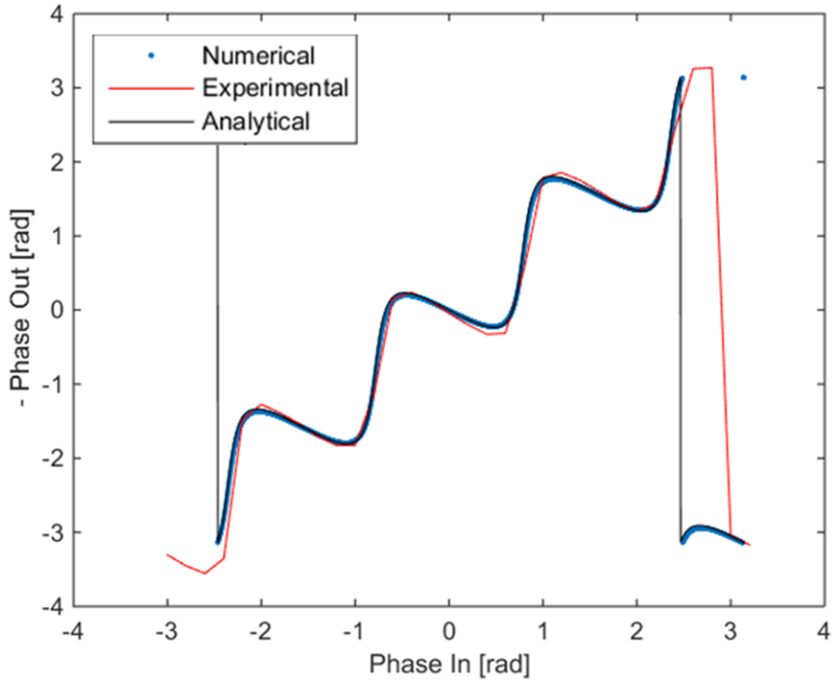

FIGURE 5.7: Phase transfer function of numerical, experimental and analytical in blue, red and black, respectively, with an 'm' value of 0.7.

experimental and numerical power ratio values for the secondary pump. The simulated P2 power was -5dBm.

Fig. 5.8 displays the normalised output amplitude versus the input phase. There is a discrepancy (<15%) with the numerical and experimental output amplitude. However, there is good agreement between the experimental and analytical data.

In conclusion it can be clearly seen that the harmonic mixing coefficient is inversely proportional to the pump power, i.e. as the pump power reduces the amount of conjugated signal which coherently adds to the (same amount of) third harmonic reduces. This reduction causes the overall output signal field to be become more dominated by the third harmonic and produce phase transfer functions with more negative slopes at the four threshold input phases as well as larger output amplitude variations.

5.2.5 EVM analysis (numerical)

This section describes a numerical study on a 10Gbaud QPSK data modulated signal. Various amounts of Gaussian phase noise were added to the signal, for three different signal to P1 power ratios, with the power of the secondary pump being swept for each set. The output EVMs of the regenerated signal are plotted against the powers of P2 along with some examples of constellation diagrams of interest. Fig. 5.9 displays a sketch of the spectral arrangement at the input of the HNLF to highlight the power budget in this first instance. The pump and signal powers were 21 and 19 dBm in this

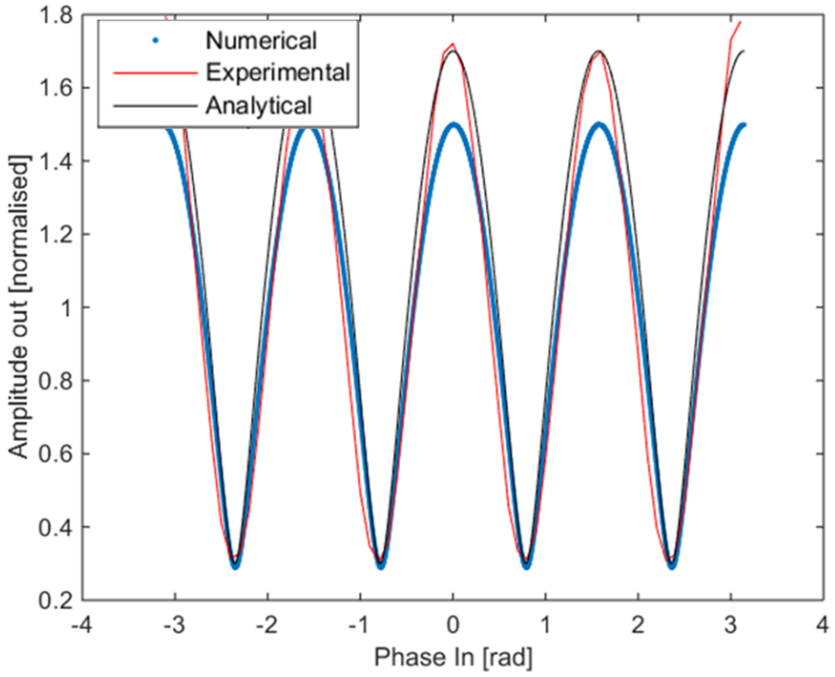

FIGURE 5.8: Output amplitude vs Input phase for numerical, experimental and analytical in blue, red and black, respectively, with an 'm' value of 0.7.

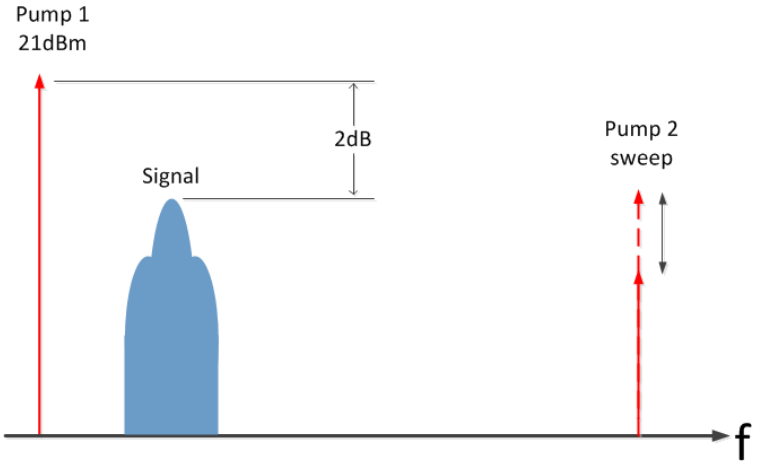

FIGURE 5.9: Cartoon of the input optical spectra when P1 power is 21 dBm, Signal power is 19 dBm and P 2 power is swept from 3.5 to 13.5 dBm.

case, respectively. Fig. 5.10 displays the EVM of the signal after the regenerator when the P2 power is swept between 3.5 dBm and 13.5 dBm. The three curves on Fig. 5.10 represent three different initial phase noise amplitudes used. The blue, red and orange curves display the output EVM values plotted for input EVM values of 5.44, 10.60 and 15.25% rms, respectively. Clearly, there is an optimal value for P2, around 7.5 dBm, where the output EVM values are the lowest for all three phase noise levels. Considering the optimum power of the secondary pump the 5.44, 10.60 and 15.25% rms input EVM values are reduced to 1.0, 2.2 and 5.0% rms, respectively.

Fig. 5.11 shows constellation diagrams of the points (1)-(5) in Fig. 5.10, each containing

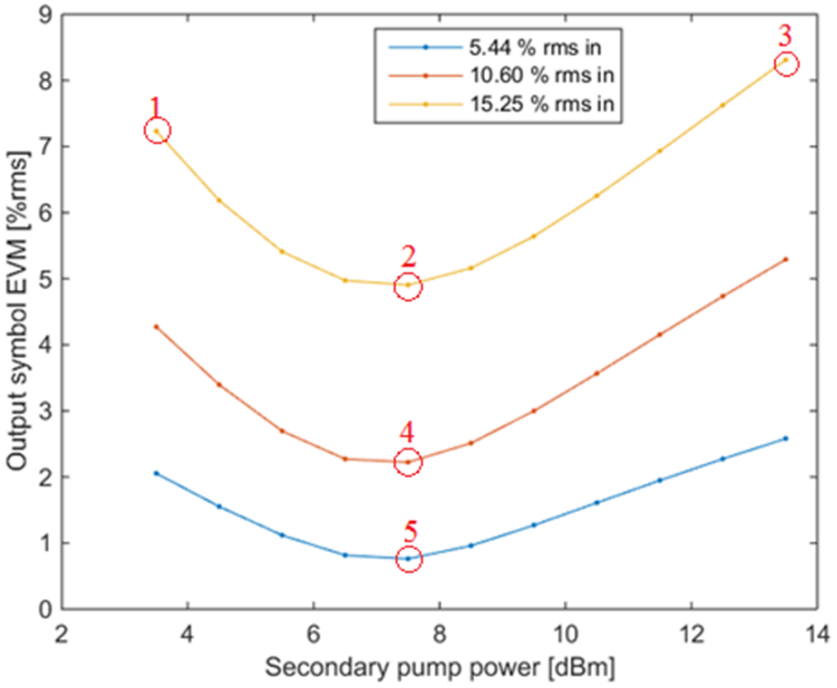

FIGURE 5.10: Output EVM study for three different levels of phase noise when P1 is 21 dBm and Signal is 19 dBm.

4096 constellation points. In particular, Fig. 5.11 1) - 3) represent the constellation points 1 - 3 respectively on the EVM curve with input EVM of 15.25% rms. Point 1 displays sub-optimal regeneration, with P2 power of 3.5 dBm. Due to the low P2 power, the contribution to the regenerated signal is lacking in conjugated signal optical field. On the other hand, the regenerated signal contains a high level of third harmonic power thus resulting in the ring shaped symbol constellation diagram. Point 2 displays optimal regeneration with a P2 power of 7.5 dBm. The regenerated output constellation diagram symbols are arrow shaped. Point 3 displays another sub-optimal regeneration, with a P2 power of 13.5 dBm. This regeneration performance is low for the opposite reasons relative to point 1. Here P2 power is too high resulting in an increase in the power of the conjugated signal at the regenerated output (or a decrease in the third harmonic). The regenerated constellation diagram symbols appear as wide-arrow shaped. Points 4 and 5 are the optimal regeneration points for input EVM of 10.60 and 5.44% rms, respectively, for a P2 power of 7.5 dBm.

Fig. 5.12 displays a sketch of the spectral arrangement at the input of the HNLF to highlight the power budget in a second scenario that was used to generate the signal EVM curves after the regenerator. The P1 and signal powers were 21 and 14 dBm, respectively, while the power of P2 was swept from -7 to 3.5 dBm. As shown in Fig. 5.13, by reducing the power of the signal, the power of the third harmonic will reduce. Hence, a lower power of P2 will be necessary to achieve the same harmonic mixing coefficients as observed previously when the P1 to signal ratio was 2dB. The blue, red and orange curves display the data plotted for input EVM values of 5.44, 9.86 and

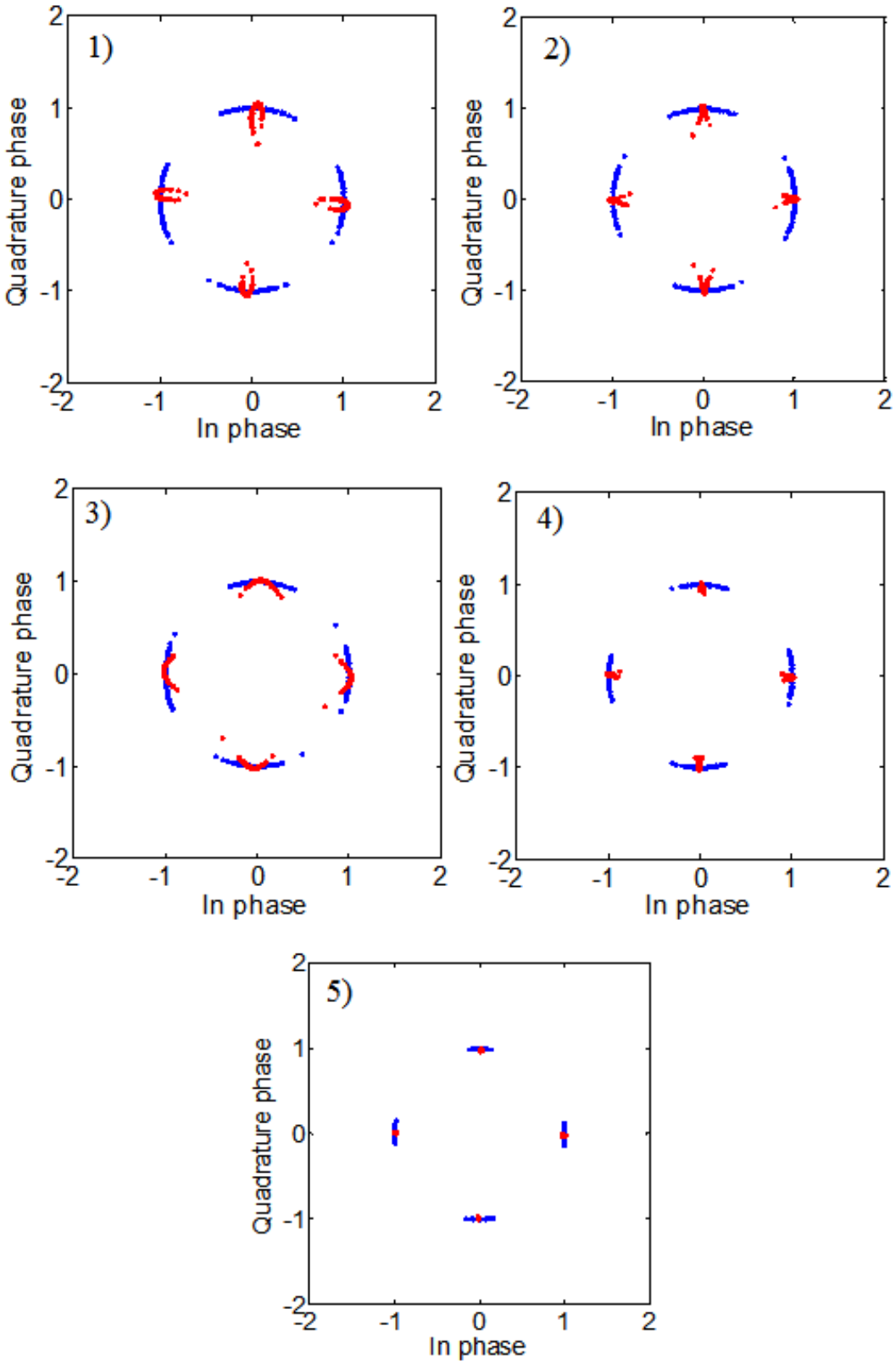

FIGURE 5.11: Constellation diagrams before (blue) and after (red) regeneration, for the points (1)-(5) displayed in Fig. 5.10.

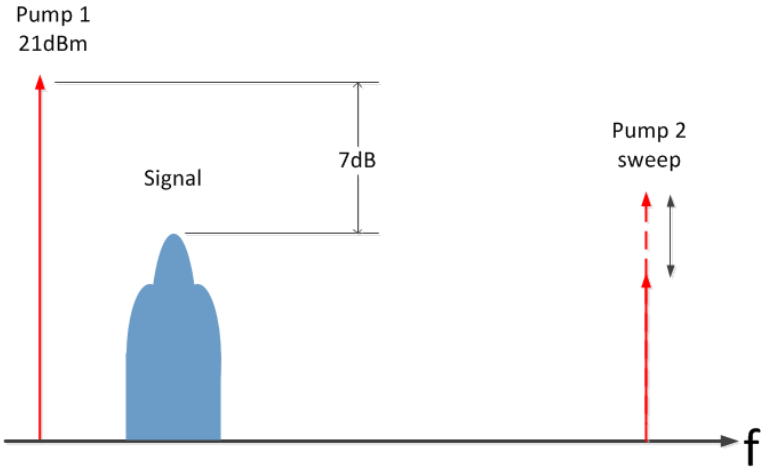

FIGURE 5.12: Cartoon of the Input spectra when P1 power is 21dBm, Signal power is 14dBm and the power of P2 is swept from -7 to 3.5dBm.

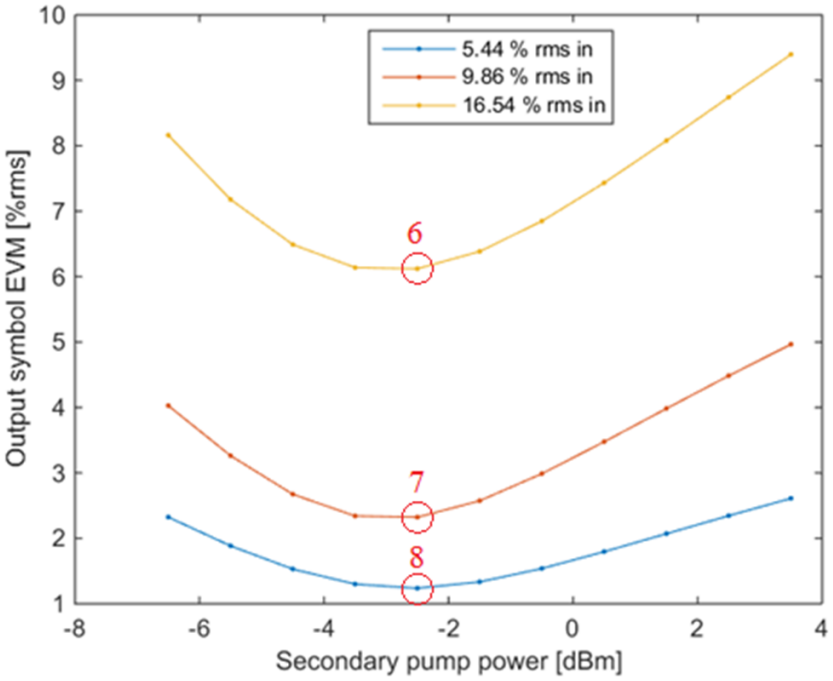

FIGURE 5.13: Output EVM study for three different levels of phase noise when P1 is 21 dBm and Signal is 14 dBm.

16.54% rms, respectively. Clearly, there is an optimal value of secondary pump power, around -2.5 dBm, where the output EVM values are the lowest for all three phase noise levels. Considering the optimum regenerative power of the secondary pump, at -2.5dBm, the 5.44, 9.86 and 16.54% rms input EVM values are reduced to 1.2., 2.3 and 6.0% rms, respectively.

Fig. 5.14 displays the constellation diagrams before (blue) and after (red) regeneration for the corresponding points 6 - 8 in Fig. 5.13. Fig. 5.14 6)-8) correspond to the optimal regeneration of input EVM of 16.54, 9.86 and 5.44% rms for the corresponding pump 2 power of -2.5 dBm.

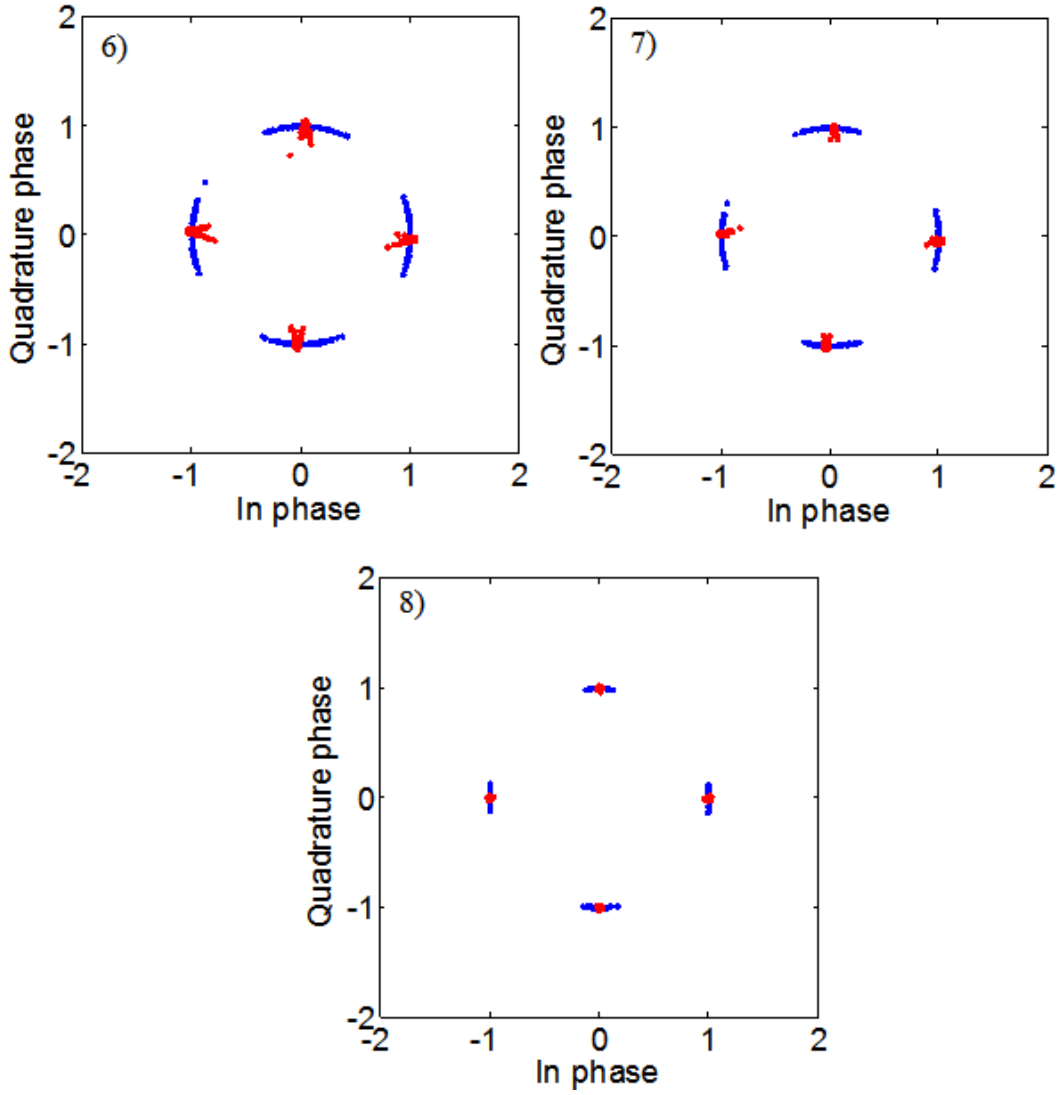

FIGURE 5.14: Constellation diagrams before (blue) and after (red) regeneration, for the points (6)-(8) displayed in Fig. 5.13.

Fig. 5.15 displays a sketch of the spectral arrangement in the HNLF to highlight the power budget in the final scenario that was studied. The P1 and signal powers were 19 and 17 dBm, respectively, while the power of P2 was swept from -3.5 to 6.5 dBm. The blue, red and orange curves display the data plotted for input EVM values of 5.44, 11.26 and 15.92% rms, respectively. There is an optimal value of the power of P2, around 1.5 dBm, where the output EVM values are the lowest for all three phase noise levels. A slight decrease in the optimal power of P2 is observed when the input EVM is increased. Considering the optimum power of the secondary pump the 5.44, 11.26 and 15.92% rms input EVM values are reduced to 1.0, 3.1 and 5.3% rms, respectively.

Fig. 5.17 displays the constellation diagrams before (blue) and after (red) regeneration for the corresponding points 9 - 11 in Fig. 5.16. Fig. 5.17 9)-11) correspond to the optimal regeneration of input EVM of 15.92, 11.26 and 5.44% rms for the corresponding pump 2 power of 1.5 dBm.

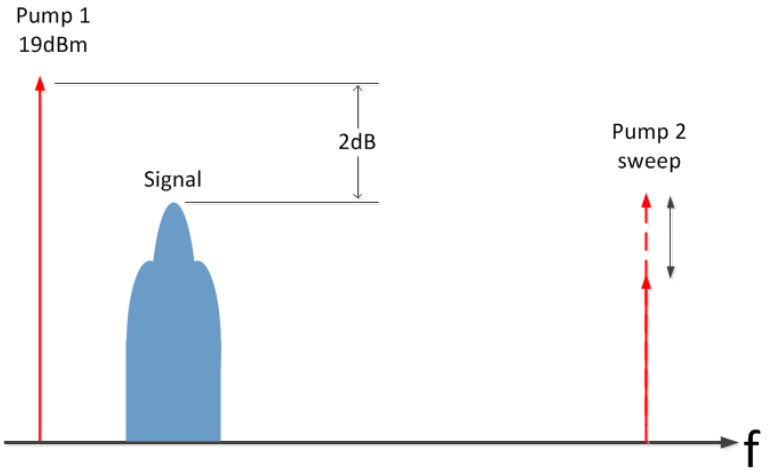

FIGURE 5.15: Cartoon of the Input optical spectra where when P1 power is 19 dBm, Signal power is 17 dBm and the pump power of P2 is swept from -3.5 to 6.5 dBm.

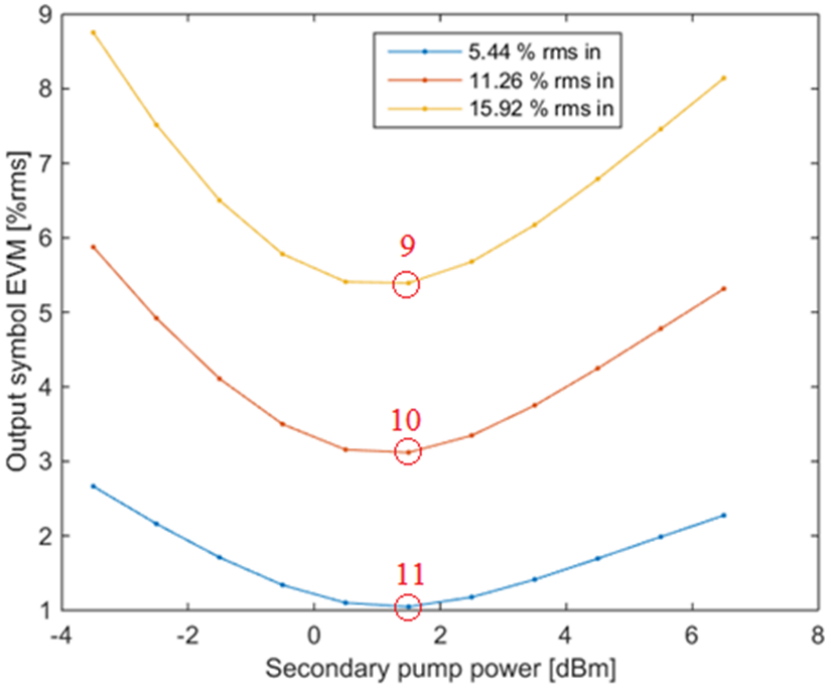

FIGURE 5.16: Output EVM study for three different levels of phase noise when P1 is 19 dBm and Signal is 17 dBm.

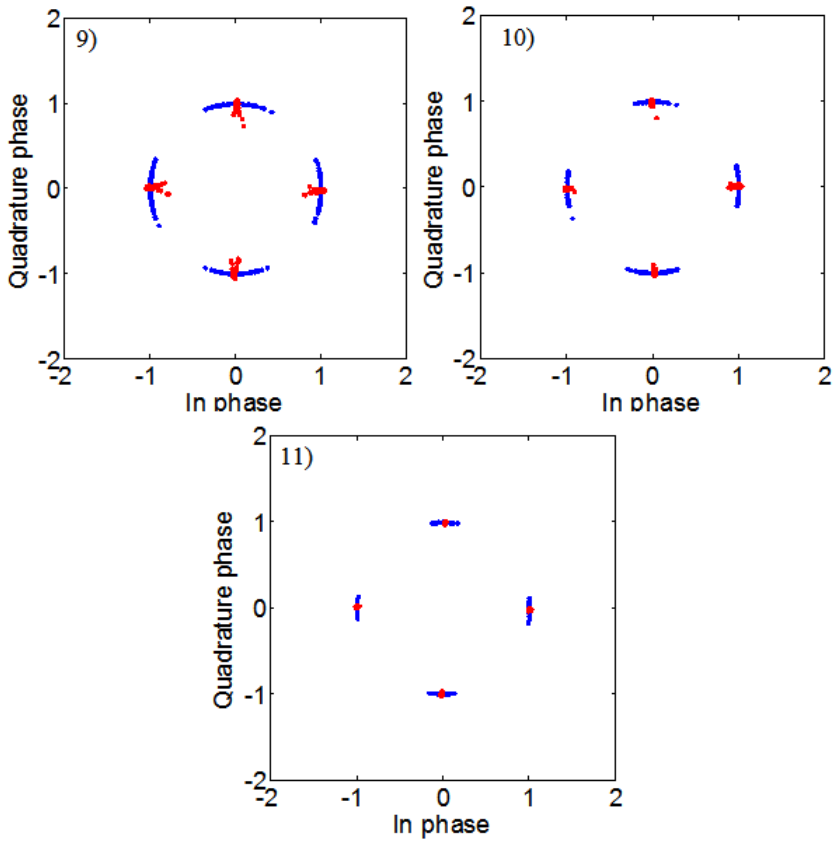

FIGURE 5.17: Constellation diagrams before (blue) and after (red) regeneration, for the points (9)-(11) displayed in Fig. 5.16.

It is important to note that for simplicity, the numerical results did not include any effect of how the OSNR of the signal and/or the generated third harmonic (regenerated signal) varies as the overall power budget changes. However, in the next experimental section it will be shown that the limit imposed by the OSNR will indeed impose a minimum overall power that can be used for specific set of signal and pump(s) values.

With the lower frequency pump (pump 1) set to 19 dBm and the input EVM set to 10.25% rms. The secondary pump power was swept between -10 and 15 dBm with the input signal power swept from 5 to 19 dBm. Fig. 5.18 displays the mesh diagram of the EVM (y-axis) vs. secondary pump power (x-axis) vs. the input signal power (z-axis). It is clear that there is a distinct valley in the EVM found for certain values of secondary pump and input signal power.

To observe the valley in greater detail a contour plot was populated with all the data held in Fig. 5.18. It is shown in Fig. 5.19.

Fig. 5.20 shows the minimum EVM vs. their corresponding input signal power. Here the minimum EVM value is shown to decrease as the signal power increases.

Fig. 5.21 displays the minimum EVM vs. their corresponding secondary pump power. The trend is that the minimum EVM reduces with increasing secondary pump power.

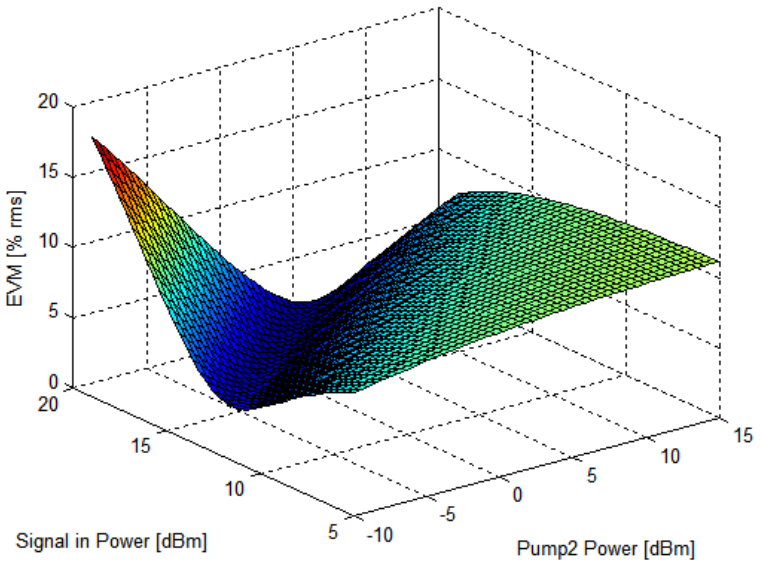

FIGURE 5.18: Mesh diagram of input signal power vs. secondary pump power vs. EVM

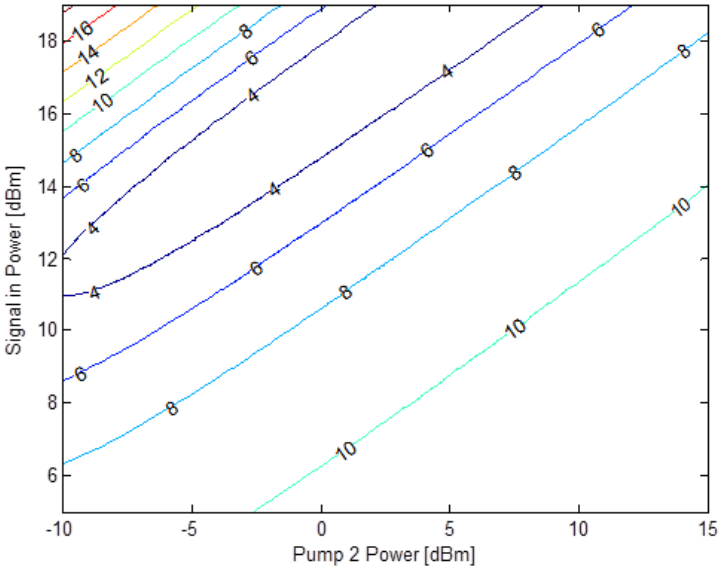

FIGURE 5.19: Contour diagram of input signal power vs. secondary pump power vs. EVM

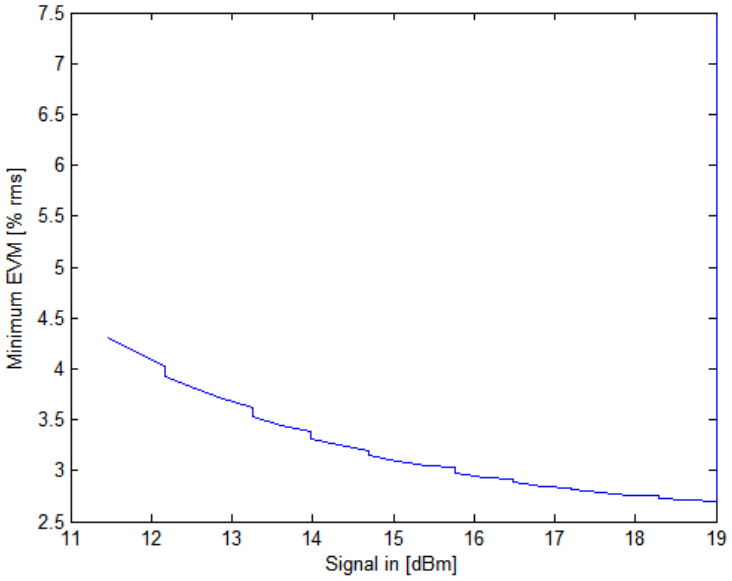

FIGURE 5.20: Minimum EMV vs. input signal power

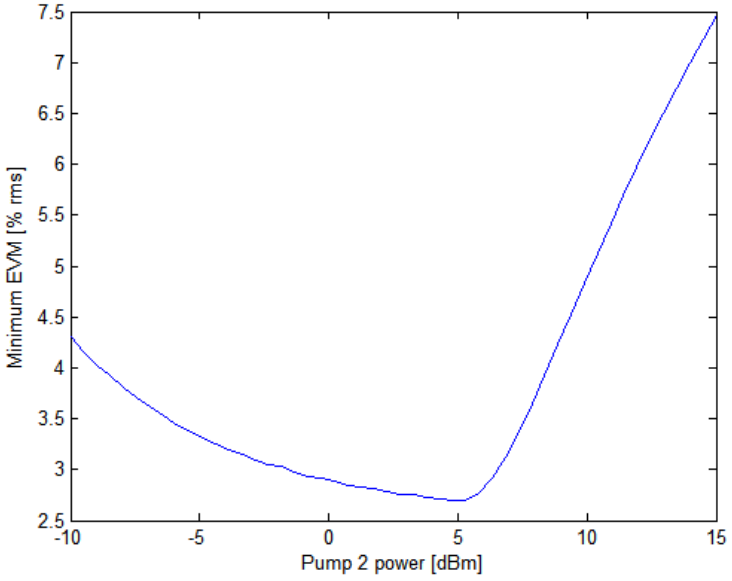

FIGURE 5.21: Minimum EMV vs. Secondary pump power

The reason that it increases after 5 dBm is that the signal in power is not sufficiently high enough. The valley of minimum EVM can be seen to run diagonally across the secondary pump power and input signal power values within Fig. 5.18.

5.2.6 Experimental work (on a QPSK data signal)

In line to the approach followed in the simulations, the experimental system was modified from the static configuration now to include a QPSK signal, as shown in Fig.

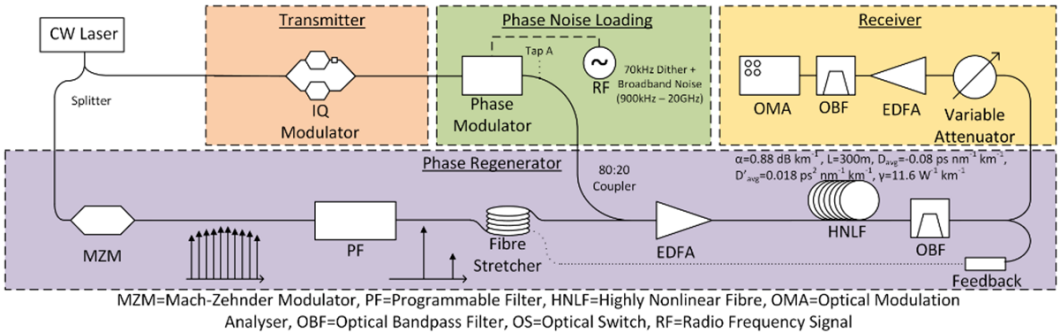

FIGURE 5.22: Experimental set-up of the idler free phase quantiser scheme, taken from [8].

5.22. A CW laser at 1557.36 nm was split into two paths. One of the CW paths was passed through a transmitter to produce a 10 GBaud NRZ-QPSK signal carrying two quadrature multiplexed PRBS $2^{15} - 1$ data streams. The other CW path was passed into a sinusoidally (over)driven MZM and P-F to generate the two pumps as previously described. Phase noise was added to the signal along with a 70 kHz sinusoidal dither (used alongside the fibre stretcher and electronic control circuitry to achieve carrier phase tracking). The signal and the pumps were coupled together and amplified before entering the same HNLF as previously discussed. The relative powers of the pumps were set using the P-F. After the HNLF, an optical band pass filter was used to select the regenerated signal. A coupler was used to tap off a small portion of the signal containing the dither waveform, which could be electronically recovered and used to stabilise the phase tracking feedback system via the fibre stretcher. The receiver consisted of a variable attenuator followed by a fixed output power EDFA, and a 0.32 nm optical band pass filter before entering an optical modulation analyser (OMA).

Fig. 5.23a) displays constellation diagrams for various amounts of phase noise before and after the phase regenerator. Fig. 5.23b) displays the corresponding BER curves for with and without regeneration applied to a signal with and without the addition of phase noise. The numbered figures in Fig. 5.23a) display the varying amounts of input phase noise for before (left) and after (right) the phase regenerator system described in this section. With no additional phase noise (inset numbers 1 and 2) the system slightly degrades the signal, quantified by a 0.5 dB power penalty for a BER of 10^{-4}. However, with the addition of input phase noise, the system reduces the overall phase noise present at the output. With an input signal phase error of 8^o rms (inset 3), the regenerated output displays a signal phase error reduced to 4.5^o rms (inset 4). With the input signal phase error increased to 12^o rms (inset 5), the regenerated output offers a substantially reduced signal phase error of 5^o rms (inset 6), resulting in an improvement in receiver sensitivity by 5.6 dB for a BER of 10^{-4}. This 5.6 dB receiver sensitivity improvement means it is possible to launch a signal with a 5.6 dB worse OSNR and still be intelligently received, the system has become more tolerant to noise.

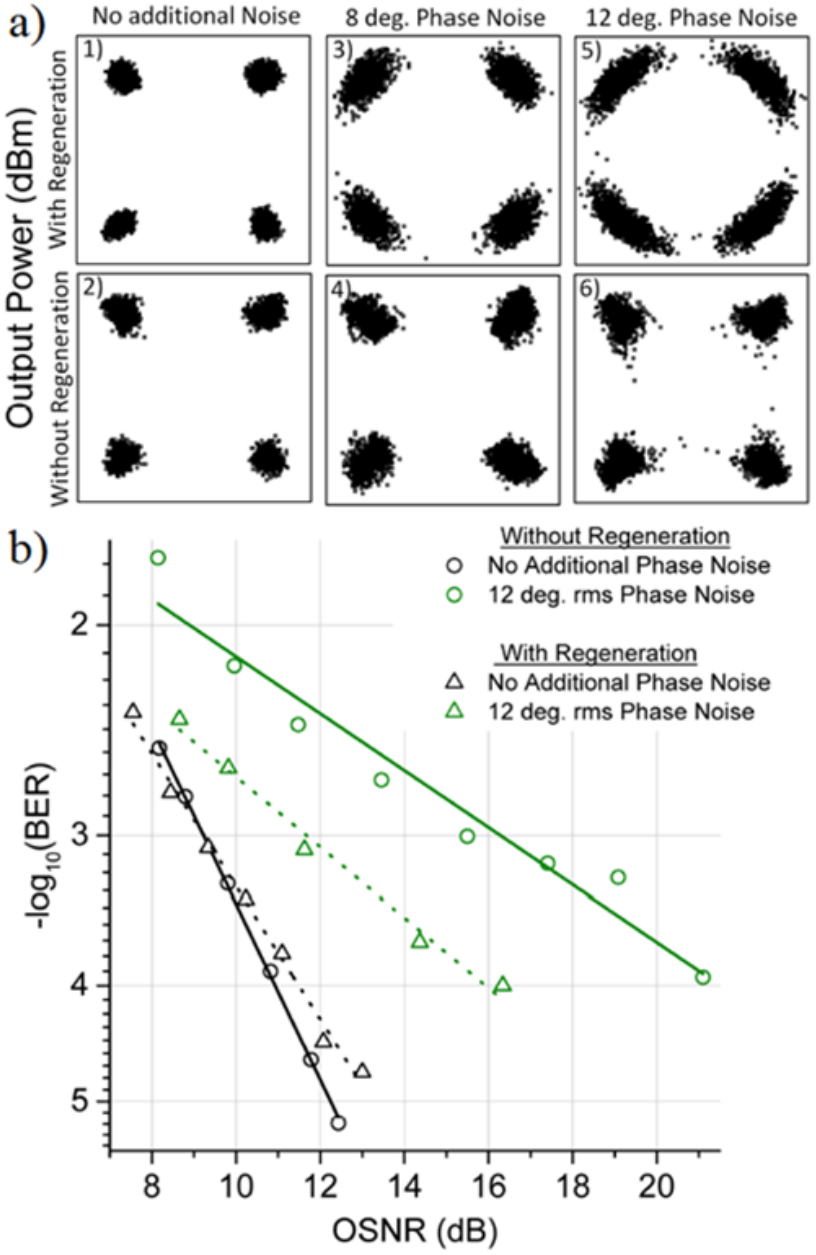

FIGURE 5.23: a) Constellation plots for various additional phase noise, before (left) and after (right) regeneration, b) BER curves for with and without regeneration, adapted from [8].

5.2.7 Discussion

Data gathered experimentally, numerically and analytically were compared for the proposed wavelength-converting idler-free phase regenerator. Static and dynamic characterizations of the new proposed scheme were carried out. Very good agreement between the experimental, numerical and analytical results are achieved for the phase transfer functions generated by varying the power of P2 at the input of the HNLF. The total power, into the HNLF (of the three optical fields), between the experimental and numerical results have a small discrepancy (however, good agreement with pumps and signal power ratios), as previously discussed. Numerical EVM analyses of the phase regenerator are shown, highlighting the regenerative performance of the system as P2 varies, and the effect of increasing the input phase noise added. Finally, the phase regenerator was experimentally analysed with a 10 GBaud QPSK signal, where the performance of the regenerator was tested with and without the addition of phase noise. The performance was assessed via constellation diagrams and BER curves, showing a small performance degradation without phase noise addition, but a 5.6 dB power sensitivity improvement (at a BER of 10^{-4}) for an input phase noise of 12^{o}rms.

5.3 Simultaneous amplitude and phase regenerator operating in the linear signal regime

To date PSAs have only been able to provide, in combination with phase regeneration, amplitude regeneration in the signal saturation regime usually at high pump powers [2, 24, 52]. Signal saturation is caused by pump depletion and/or excitation of higher-order FWM components [68, 73]. In the second part of this chapter a simultaneous amplitude and phase regeneration technique based on PSA is proposed and numerically validated, where amplitude squeezing is achieved while the signal operates in the linear amplification region (i.e. far from pump depletion).

5.3.1 Operation principle and setup

A spectral illustration of the pumping scheme used to achieve the amplitude and phase regenerator is shown in Fig. 5.24. Initially the conjugated $(M+1)^{th}$ (where M is the number of phase levels used) phase harmonic is created, from an incoming M-PSK signal, through a single pump (P1 in Fig. 5.24a)) FWM scheme (PIA stage), producing high order phase harmonics (phase locked to the signal and pump (P1)). This harmonic is then phase shifted by π radians before being mixed back into the signal through a second stage of FWM based on a dual pump (P1 and P2, which are both phase locked to the signal) non-degenerate PSA, as illustrated in Fig. 5.24b). In the small gain regime the

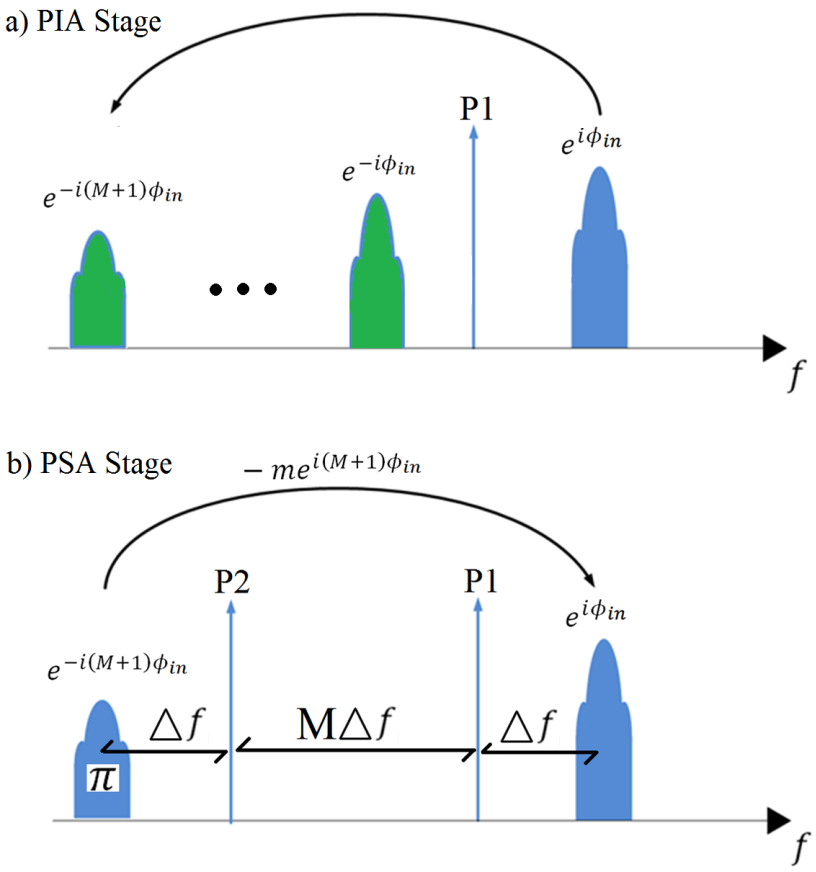

FIGURE 5.24: a) Harmonic generation through PIA Stage, and b) Harmonic addition through PSA Stage of the proposed MPSK regenerator.

signal transfer function at the output of the scheme can be analytically expressed by the following equation:

$$\begin{aligned} A_{out}e^{i\phi_{out}t} &\propto A_{in}e^{i\phi_{in}t} + mA_{in}^{(M+1)}e^{i(M+1)\phi_{in}t+\pi} \\ &\propto A_{in}e^{i\phi_{in}t} - mA_{in}^{(M+1)}e^{i(M+1)\phi_{in}t} \end{aligned} \tag{5.2}$$

Where A_{out} and ϕ_{out} are the output signal electric field amplitude and phase, A_{in} and ϕ_{in} are the input amplitude and phase of the incoming MPSK signal and m is the harmonic mixing coefficient of both the PIA and PSA stages. The negative sign in front of the second term on the right hand side expressed in Eq. 5.2 is due to the π phase shift placed on the conjugated M+1^{th} harmonic. In this expression, the phases of the various pumps have been neglected while their amplitudes are included in the coefficient m. The greater the pump powers (in reference to the signal), the closer the m factor will be to 1.

For the specific case of a BPSK signal ($M = 2$), Fig. 5.25 displays the analytical response of Eq. 5.2, with $m = 0.322$ (calculated to achieve a flat phase plateau at zero input phase in the phase transfer function), where Fig. 5.25(a) is the phase transfer

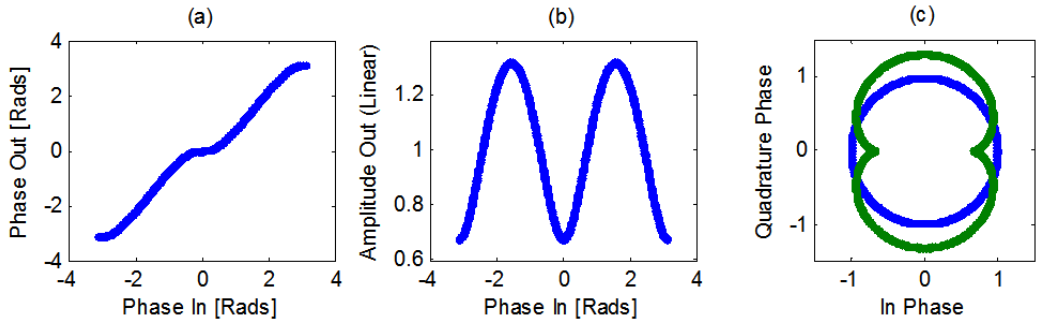

FIGURE 5.25: a) Phase transfer function, b) Amplitude phase transfer function versus input phase and c) full phase spread constellation diagram of input (blue) and output (green).

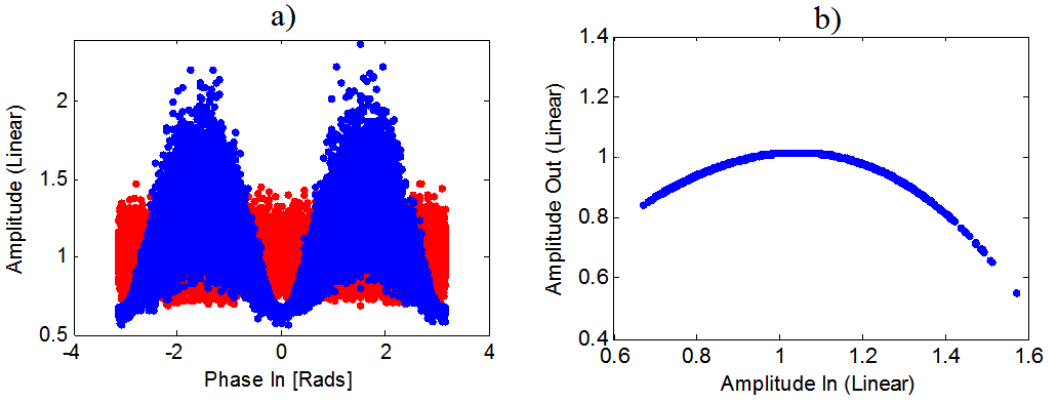

FIGURE 5.26: a) Amplitude versus input phase before (red) and after (blue) regeneration, b) Amplitude transfer function (linear).

function, Fig. 5.25(b) is the output amplitude evolution as a function of the input phase and Fig. 5.25(c) is the full phase spread constellation diagram for the input signal (blue) and the output signal (green). It is clear that the phase transfer function offers a two level squeezing effect (as there are two plateaus observable in the output phase) within the 0 to 2π region. In order to appreciate the amplitude squeezing capability of this regenerator the amplitude out versus input phase (seen in Fig. 5.25(b)) with added input amplitude noise will be analysed in the following section.

5.3.2 BPSK Results and discussion

As mentioned above, Fig. 5.25 displays the analytical response of Eq. 5.2 modified for a BPSK signal.

Fig. 5.26a) displays the amplitude fluctuations before (red) and after (blue) the regenerator versus the input phase when a input Gaussian amplitude noise distribution of 10.7 % is added to the signal. It is apparent that the output amplitude distribution changes as a function of the input phase. The regions of interest of amplitude squeezing lie around the input phases of 0 and $\pm\pi$ radians (plateau regions in the corresponding

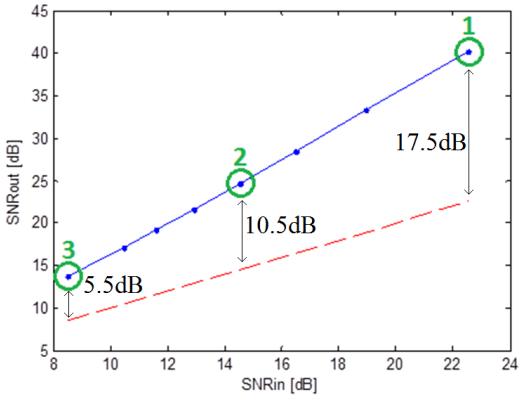

FIGURE 5.27: Input SNR versus output SNR, in dB. 1:1 ratio represented by the red dashed line.

phase transfer function of Fig. 5.25a)), where a minimum amplitude noise distribution of 1.6 % can be seen, providing an amplitude regeneration factor of 6.69 for an optimised mixing coefficient of $m = 0.3071$. This can be understood as the amplitude noise present on the high-order harmonic of interest (conjugated third in the BPSK case) is greater than that present on the original BPSK signal and indeed it has an amplitude noise fluctuation that can be proportional to A_{in}^3, and can be subtracted, via the π phase shift of the harmonic, from the original amplitude noise fluctuation via the mixing coefficient m.

Signal-to-noise ratio (SNR) analysis

An initial study of the SNR at the input and output of the system was carried out. To calculate the input and output SNRs the following equations were used (taken from [78]):

$$\begin{aligned} SNR(dB) &= 10\log_{10}\left(\frac{Power_{Signal}}{Power_{Noise}}\right) \\ SNR_{IN}(dB) &= 10\log_{10}\left(\frac{|mean(IN)|}{|var(IN)|}\right) \\ SNR_{OUT}(dB) &= 10\log_{10}\left(\frac{|mean(OUT)|}{|var(OUT)|}\right) \end{aligned} \tag{5.3}$$

Where *var* implies the variance of the input (IN) and output (OUT) symbol distribution and SNR_{IN} and SNR_{OUT} represent the SNR at the input and output, respectively. Fig. 5.27 shows the SNR at the output of the regenerator versus the SNR at the input of the regenerator, shown by the blue curve. The red dashed line represents the 1:1 ratio line, highlighting that the regenerator offers SNR improvement. It is clear from Fig. 5.27 that for higher input SNR there is a higher SNR improvement offered by the regenerator. It is worth noting that for each point in Fig. 5.27 the harmonic mixing coefficient (m factor) had to be optimised to achieve the highest output SNR. For each point various m factor values were used and the one which gave the highest output SNR values was used.

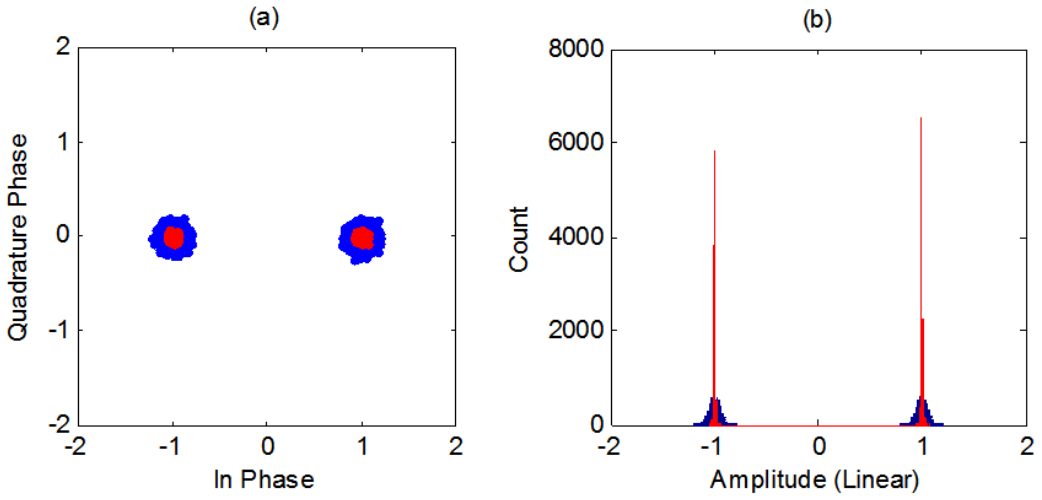

FIGURE 5.28: Analytical results displaying a) Constellation diagram and b) in-phase axis histogram of the signal before (blue) and after (red) the regenerator, for an input SNR of 22.5 dB.

BPSK Constellation analysis

The system was assessed for three particular initial SNRs, the three green values in Fig. 5.27, in terms of constellation diagrams and histograms of the in-phase axis, in Figs. 5.28, 5.29 and 5.30, respectively. For BPSK signals the in-phase axis corresponds to signal amplitude fluctuations and thus was chosen to further study the amplitude noise distribution before (blue curve) and after (red curve) the regenerator.

Fig. 5.28 displays point 1 on Fig. 5.27, with an input SNR, output SNR, input phase standard deviation, output phase standard deviation, input amplitude standard deviation and output amplitude standard deviation of 22.5 dB, 40.1 dB, 0.053 rad, 0.0085 rad, 5.34 % and 0.58 %, respectively. The optimised harmonic mixing coefficient used here is $m = 0.322$. Here a SNR improvement of 17.5dB was achieved with a 6.2 and 9.2 times improvement in phase and amplitude noise distribution, respectively.

Fig. 5.29 displays point 2 on Fig. 5.27, with an input SNR, output SNR, input phase standard deviation, output phase standard deviation, input amplitude standard deviation and output amplitude standard deviation of 14.5 dB, 24.7 dB, 0.134 rad, 0.049 rad, 13.2 % and 3.46 %, respectively. The optimised harmonic mixing coefficient used here is $m = 0.3051$. Here a SNR improvement of 10.2 dB was achieved with a 2.7 and 3.8 times improvement in phase and amplitude noise distribution, respectively. Looking at the histogram on the RHS of Fig. 5.29 allows for an easier visualisation of the improvement in SNR, as the distribution has changed from a Gaussian to a super-Gaussian.

Fig. 5.30 displays point 3 on Fig. 5.27, with an input SNR, output SNR, input phase standard deviation, output phase standard deviation, input amplitude standard deviation and output amplitude standard deviation of 8.5 dB, 13.7 dB, 0.277 rad, 0.179 rad, 25.92 % and 12.42 %, respectively. The optimised harmonic mixing coefficient used here

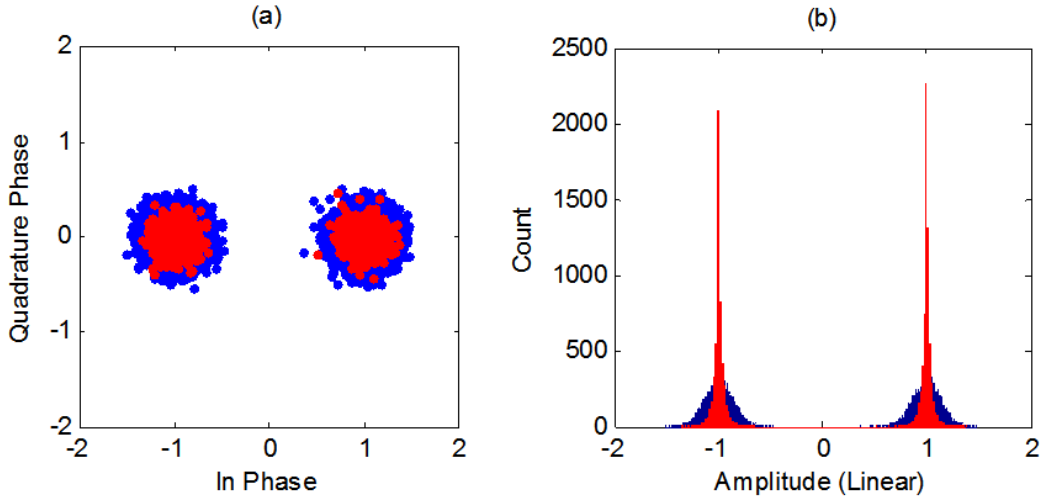

FIGURE 5.29: Analytical results displaying a) Constellation diagram and b) in-phase axis histogram of the signal before (blue) and after (red) the regenerator, for an input SNR of 14.5 dB.

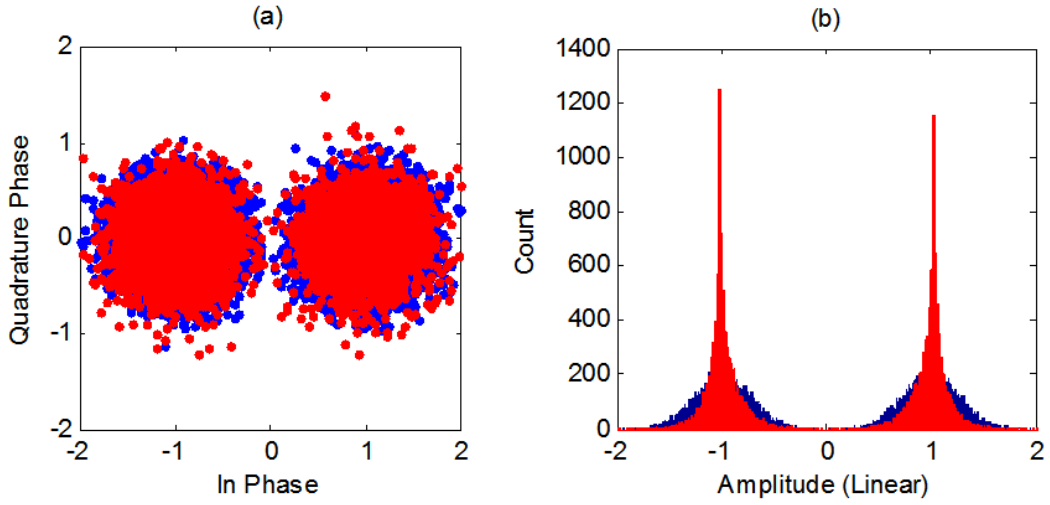

FIGURE 5.30: Analytical results displaying a) Constellation diagram and b) in-phase axis histogram of the signal before (blue) and after (red) the regenerator, for an input SNR of 8.5 dB.

is $m = 0.2542$. Here a SNR improvement of 5.2 dB is achieved with a 1.5 and 2.1 times improvement in phase and amplitude noise distribution, respectively.

It can be seen that for increasing values of noise (reducing input SNR) the optimum harmonic mixing coefficient m value reduces as expected from Eq. 5.2 and the SNR improvement of the regenerator is greater when lower noise levels are added to the system.

Noise perimeter analysis

The following study was focused on the performance of the analytically calculated system with the input of the right-most BPSK symbol (nominally at 0 rads) approximated with

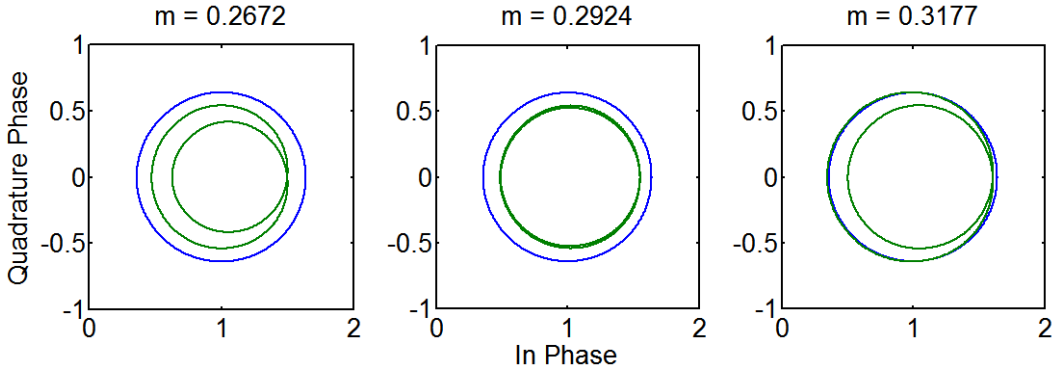

FIGURE 5.31: Constellation diagrams of input (blue) and output (green) of the regenerator, with m values lower (left), equal to (middle) and above (right) the optimal value.

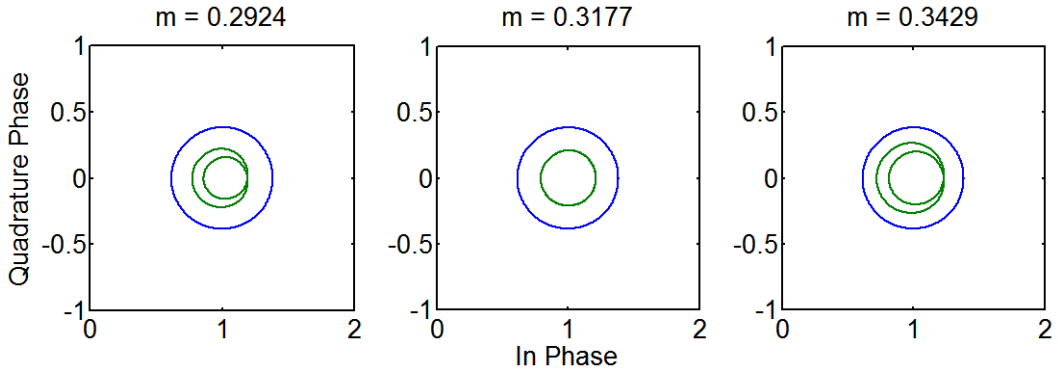

FIGURE 5.32: Constellation diagrams of input (blue) and output (green) of the regenerator, with m values lower (left), equal to (middle) and above (right) the optimal value.

a circular shape. With this circular shaped symbol it was possible to appreciate how the perimeter of the output symbol changes at the output of the regenerator. Figs. 5.31 - 5.33 display the input (blue) and output (green) constellation diagrams of the regenerator for different diameters of the input circle, corresponding to different noise levels. Each figure has three constellation diagrams, displaying the output of the regenerator with an m factor value lower than (left), equal to (middle) and greater than (right) the optimal m factor value for each instance. It is noticeable with an increase in the input circle diameter the m value required for optimal regeneration reduces. Considering Eq. 5.2 this relationship can be intuitively understood as the input noise increases the A_{in}^3 term becomes comparatively larger than the A_{in} term and thus a smaller m value is required to minimise the equation. The m factor plays an important role in optimising the regenerated signal. If the m value is too small or too large the perimeter traced by the output constellation diagram shows concentric circles with different diameters. For the optimal m value the concentric circles overlap with (almost) the same diameter.

BPSK Simulations

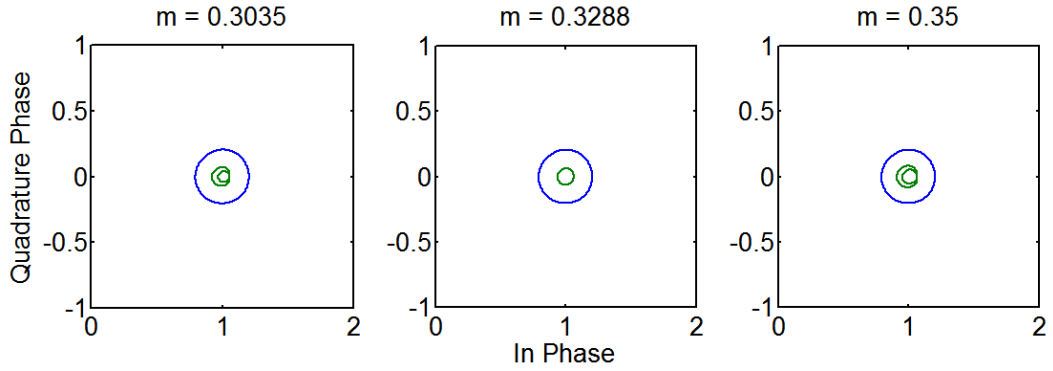

FIGURE 5.33: Constellation diagrams of input (blue) and output (green) of the regenerator, with m values lower (left), equal to (middle) and above (right) the optimal value.

A schematic of the setup for the simulation of a regenerator of a generic M-PSK signal is shown in Fig. 5.34). A noisy (both in amplitude and phase) MPSK signal was coupled with a CW pump (P1) before entering the first HNLF, the PIA stage, to generate the higher-order phase harmonics, including the required $(M+1)^{th}$ phase harmonic. The output was launched into a wavelength selective switch (WSS) which can filter out the undesirable harmonics, adjust the relative power of the remaining optical waves and apply the π radian phase shift to the $(M+1)^{th}$ harmonic. A new pump (P2) was coupled with P1, the signal and the $(M+1)^{th}$ harmonic. P2 needs to be phase-locked with the other waves. This can be practically achieved using the modulation stripped M^{th} phase harmonic, generated in the PIA stage, filtered and amplified using an injection-locked laser, as demonstrated in [2]. The subsequent four optical fields (see Fig. 5.24b)) enter the second HNLF, acting as a dual-pump nondegenerate PSA. In the simulations, the HNLFs (for PIA and PSA stages) had the same fibre parameters, such that the dispersion, dispersion slope, zero dispersion wavelength, nonlinear coefficient, linear loss and length were -0.08ps/nm/km, 0.018ps/nm^2/km, 1553nm, 11.6/W/km, 0.88dB/km and 0.3 km, respectively. The signal was filtered out and analysed. In the simulation we considered both the cases of BPSK and QPSK signals and in this section the results for a BPSK signal will be reported.

For the simulations of BPSK signals the initial pump power for the harmonic generation stage is 30 dBm, with the input signal power of 10 dBm. The pumps in the PSA stage are 15 dBm each, the signal power was reduced to 0 dBm and the conjugated third harmonic power was varied for best performance. The signal was centred at 1557 nm with a repetition rate of 40 Gbit/s. For each case 2048 symbols were considered. For the following figures the constellation diagram (left) and in-phase axis histogram (right) of the signal before (blue) and after (red) regeneration are displayed.

Fig. 5.35 displays the analysis of the signal with input SNR, output SNR, input phase standard deviation, output phase standard deviation, input amplitude standard deviation and output amplitude standard deviation of 22.5 dB, 33.5 dB, 0.052 rad, 0.018

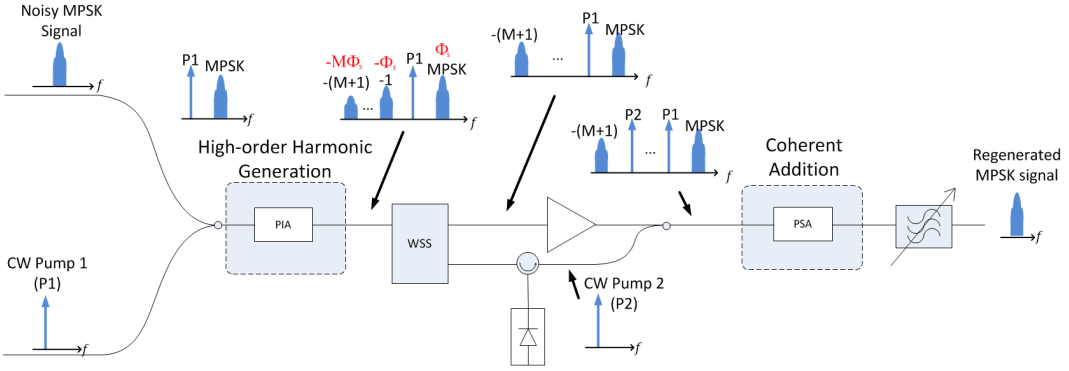

FIGURE 5.34: Operating principle of the simulated setup of the proposed MPSK regenerator.

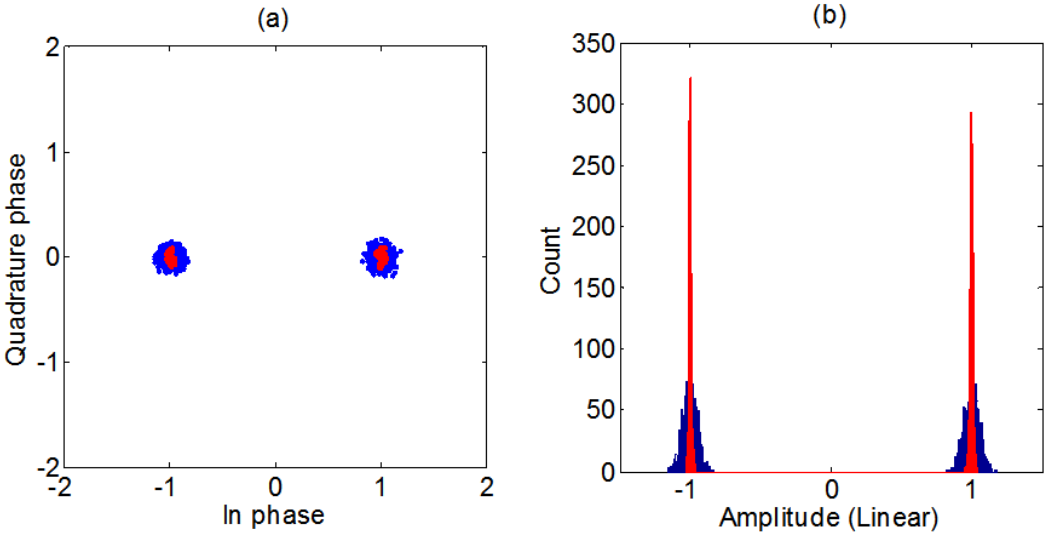

FIGURE 5.35: Simulated results of the signal before (blue) and after (red) the regenerator, a) Constellation diagram and b) in-phase axis histogram for an input SNR of 22.5 dB.

rad, 5.3 % and 1.1 %, respectively. For this noise level the conjugated third harmonic power at the input of the PSA stage was 8 dBm and a SNR improvement of 11 dB was achieved with a 2.9 and 4.8 times improvement in phase and amplitude noise distribution, respectively.

Fig. 5.36 displays the analysis of the signal with input SNR, output SNR, input phase standard deviation, output phase standard deviation, input amplitude standard deviation and output amplitude standard deviation of 14.5 dB, 20.8 dB, 0.134 rad, 0.072 rad, 12.74 % and 5.59 %, respectively. For this noise level the conjugated third harmonic power at the input of the PSA stage was 7 dBm and a SNR improvement of 6.3 dB was achieved with a 1.9 and 2.3 times improvement in phase and amplitude noise distribution, respectively.

Fig. 5.37 displays the analysis of the signal with input SNR, output SNR, input phase

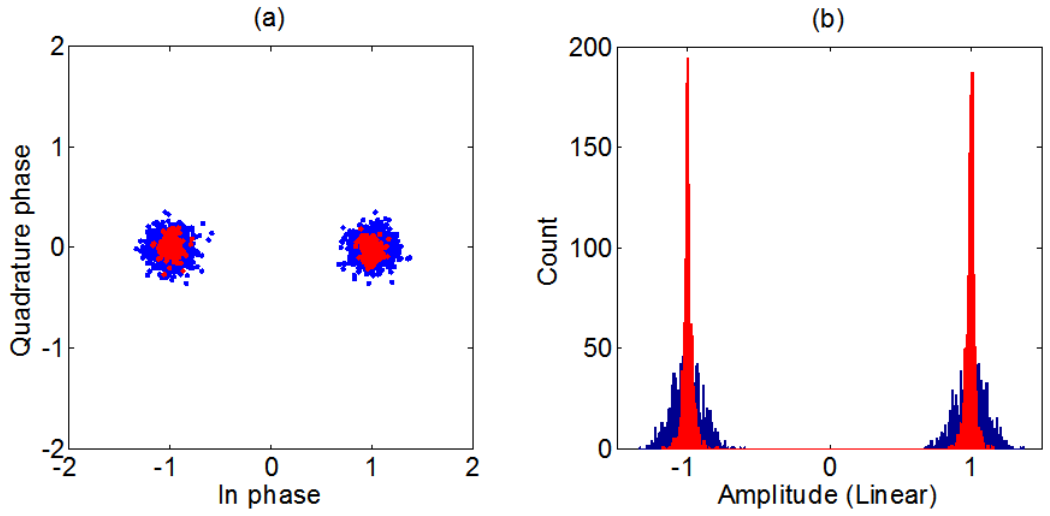

FIGURE 5.36: Simulated results of the signal before (blue) and after (red) the regenerator, a) Constellation diagram and b) in-phase axis histogram for an input SNR of 14.5 dB.

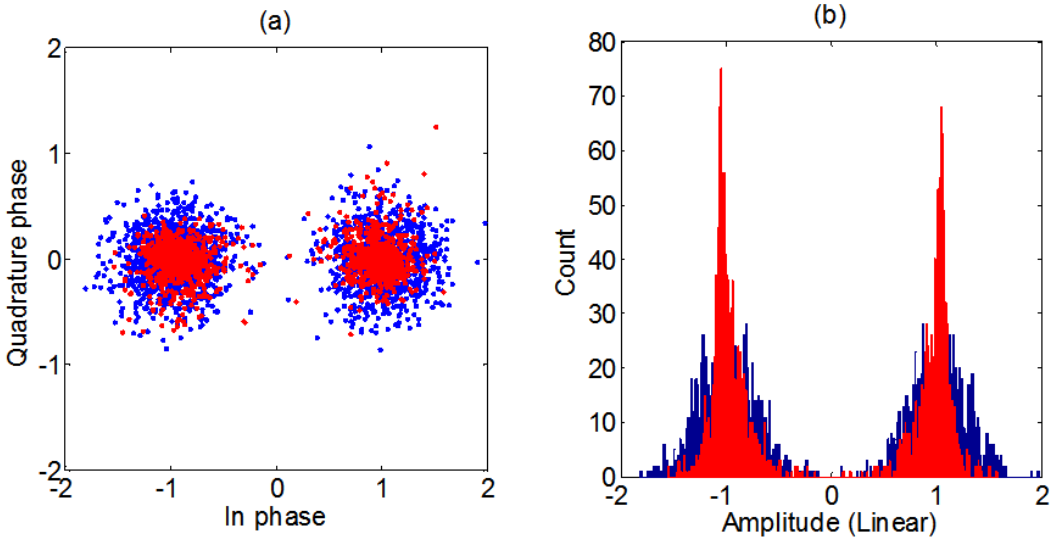

FIGURE 5.37: Simulated results of the signal before (blue) and after (red) the regenerator, a) Constellation diagram and b) in-phase axis histogram for an input SNR of 8.5 dB.

standard deviation, output phase standard deviation, input amplitude standard deviation and output amplitude standard deviation of 8.5 dB, 10.88 dB, 0.283 rad, 0.225 rad, 25.66 % and 18.31 %, respectively. For this noise level the conjugated third harmonic power at the input of the PSA stage was 6 dBm and a SNR improvement of 2.38 dB was achieved with a 1.3 and 1.4 times improvement in phase and amplitude noise distribution, respectively.

Fig. 5.38 displays the corresponding phase (a) and amplitude (b) noise standard deviation transfer functions obtained from in Figs. 5.35 - 5.37. The red dashed lines represent the 1:1 ratio. Both phase and amplitude noise standard deviations at the output of the

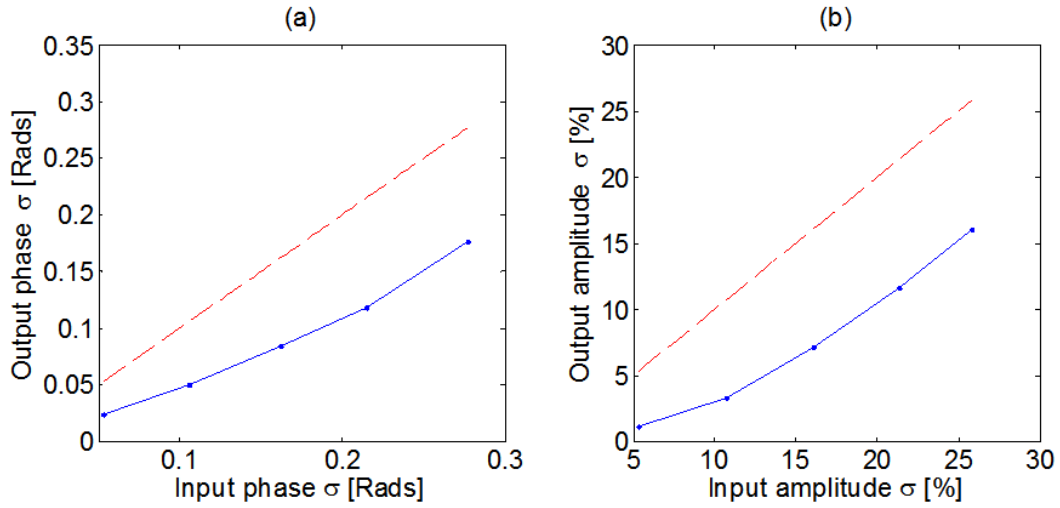

FIGURE 5.38: a) Phase standard deviation transfer function, b) amplitude standard deviation transfer function (1:1 ratio represented by the red dashed lines).

regenerator are smaller than their corresponding values at the input of the regenerator, highlighting the simultaneous amplitude and phase regeneration for this scheme. The comparative performance of the regenerator increases with reducing input phase and amplitude noise, which agrees with the trend observed within the analytical analysis. Similarly, the simulations have agreed with the analytical model, as the lower the input SNR the lower the harmonic mixing coefficient was needed for optimal performance i.e. the conjugated third harmonic was reduced for reducing input SNR.

Drawing a direct comparison between the output phase standard deviation and output amplitude standard deviation of the three analytical figures (Figs. 5.28, 5.29 and 5.30) with the figures generated through simulation (Figs. 5.35, 5.36 and 5.37) it is possible to compare the difference in output phase and amplitude standard deviation of the three input SNRs (22.5 dB, 14.5 dB and 8.5 dB). For an input SNR of 22.5 dB the ratio between output phase standard deviation for simulated and analytical work is 2.12, whereas the ratio between output amplitude standard deviation for simulated and analytical work is 1.90. For an input SNR of 14.5 dB the ratio between output phase standard deviation for simulated and analytical work is 1.47, whereas the ratio between output amplitude standard deviation for simulated and analytical work is 1.62. For an input SNR of 8.5 dB the ratio between output phase standard deviation for simulated and analytical work is 1.26, whereas the ratio between output amplitude standard deviation for simulated and analytical work is 1.47. Here, it is shown that as the SNR reduces the difference between the simulated and analytical results reduce for both the output phase and amplitude standard deviations.

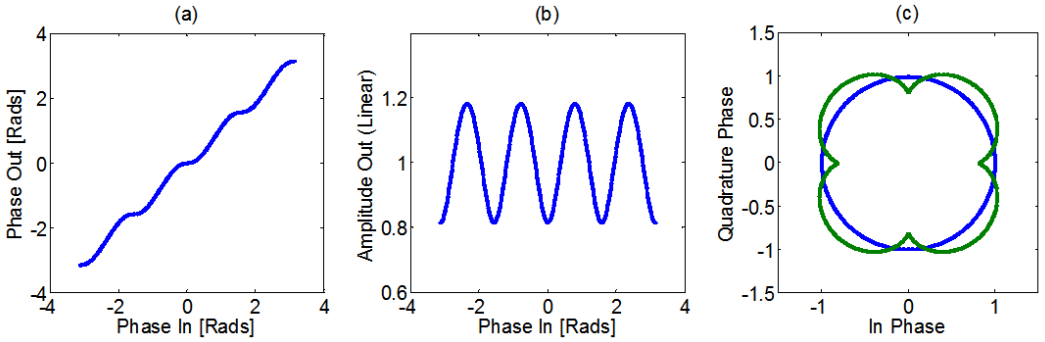

FIGURE 5.39: a) Phase transfer function, b) Amplitude phase transfer function versus input phase and c) full phase spread constellation diagram of input (blue) and output (green).

5.3.3 QPSK Results and discussion

As discussed earlier, the proposed scheme can be extended to any M-PSK signal and, in this section a QPSK (M=4) signal will be analysed similarly to the previous BPSK case. Fig. 5.39 displays the response of Eq. 5.2 modified for a QPSK signal, with $m = 0.1837$ (obtained to give a flat phase response for the four phase positions of interest), where the phase transfer function (a), the amplitude out versus input phase (b), and the full phase spread constellation diagram (c) for input signal (blue) and output signal (green) are shown. It is clear that the phase transfer function presents a four level squeezing effect, observable by the four plateaus in the output phase of Fig 5.39(a). As discussed previously, the phase plateaus correspond to the minimum of the amplitude transfer function profile. Similar to the BPSK case, the amplitude regeneration effects cannot be understood from Fig. 5.39, but are understood by the same effect as detailed earlier for BPSK (seen in Fig. 5.26).

SNR analysis

The system was first analytically characterised in terms of SNR. Fig. 5.40 displays the corresponding SNR of the input and output of the system. It is clear that the same trend as the BPSK SNR is achieved (as seen in Fig. 5.27), with the reduction of SNR improvement observed as the input SNR is reduced. However, the SNR improvement observed for the QPSK regenerator at any specific input SNR is lower than the one achieved for the BPSK regenerator. For example, at an input SNR of 20 dB the output SNR for the BPSK case is 35 dB whereas the output SNR for the QPSK case is 30 dB.

QPSK Constellation analysis

Similarly to the case of the BPSK signal, three specific initial input SNRs (circled in green in Fig.5.40) were chosen and initially analytically investigated using Eq. 5.2 and are shown in Figs. 5.41, 5.42 and 5.43, respectively. Each figure includes a constellation diagram (left) and an in-phase axis histogram of the symbols present on the in-phase

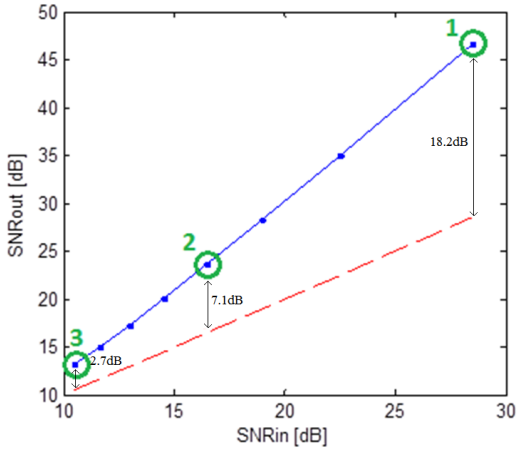

FIGURE 5.40: Input SNR versus output SNR, in dB. 1:1 ratio represented by the red dashed line.

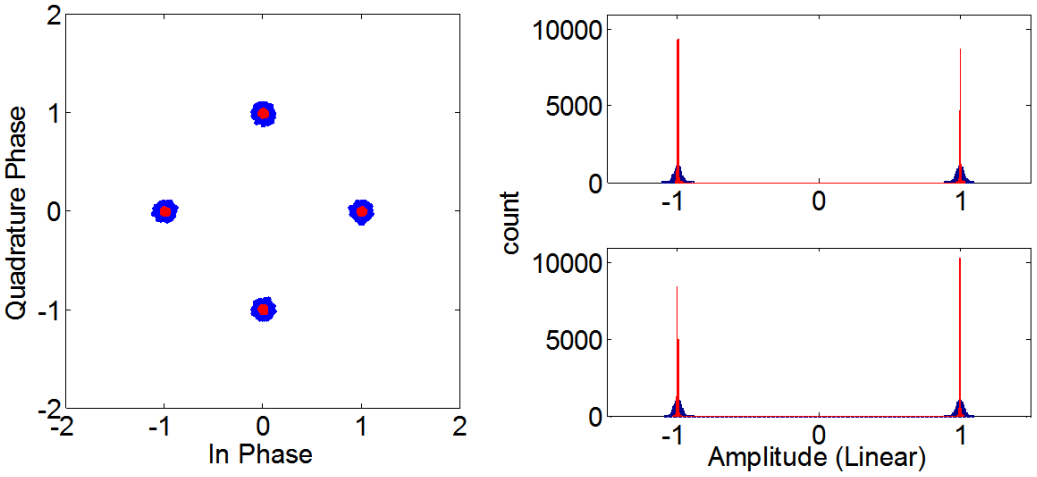

FIGURE 5.41: Signal before (blue) and after (red) the regenerator, a) Constellation diagram and b) in-phase axis histogram for an input SNR of 28.5 dB.

axis (top right) and a quadrature-phase axis histogram of the symbols present on the quadrature-phase axis (bottom right) of the signal before (blue) and after (red) the regenerator, these histograms correspond to the amplitude noise distributions (on the 0, π, $\pi/2$, $3\pi/2$ rad phase values) of the four symbols in the QPSK signal.

Fig. 5.41 displays point 1 on Fig. 5.40, with an input SNR, output SNR, input phase standard deviation, output phase standard deviation, input amplitude standard deviation and output amplitude standard deviation of 28.5 dB, 46.7 dB, 0.026 rad, 0.0037 rad, 2.65 % and 0.29 %, respectively. The optimised harmonic mixing coefficient used here is $m = 0.2041$. Here a SNR improvement of 18.2 dB is achieved with a 7 and 9.1 times improvement in phase and amplitude noise distribution, respectively.

Fig. 5.42 displays point 2 on Fig. 5.40, with an input SNR, output SNR, input phase standard deviation, output phase standard deviation, input amplitude standard deviation and output amplitude standard deviation of 16.5 dB, 23.6 dB, 0.107 rad, 0.051 rad,

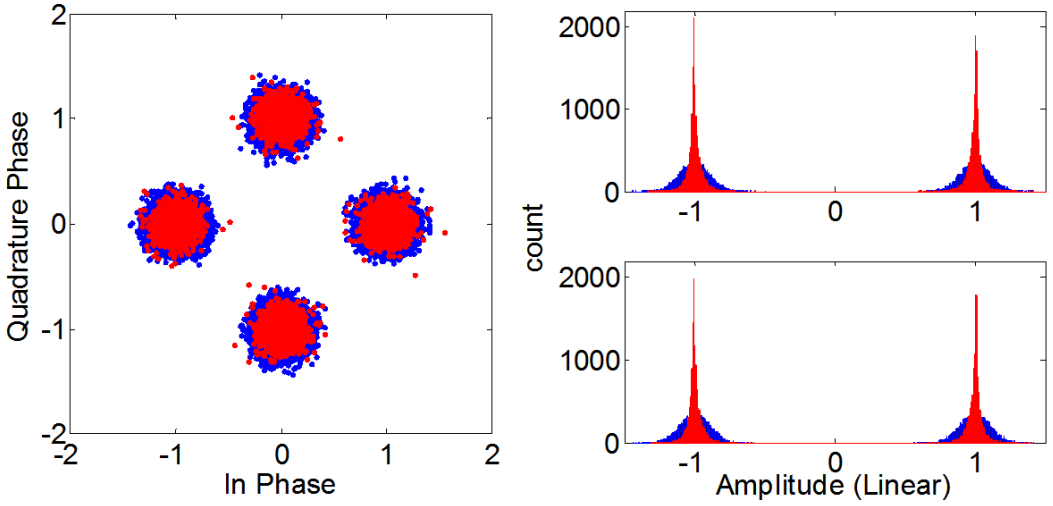

FIGURE 5.42: Signal before (blue) and after (red) the regenerator, a) Constellation diagram and b) in-phase axis histogram for an input SNR of 16.5 dB.

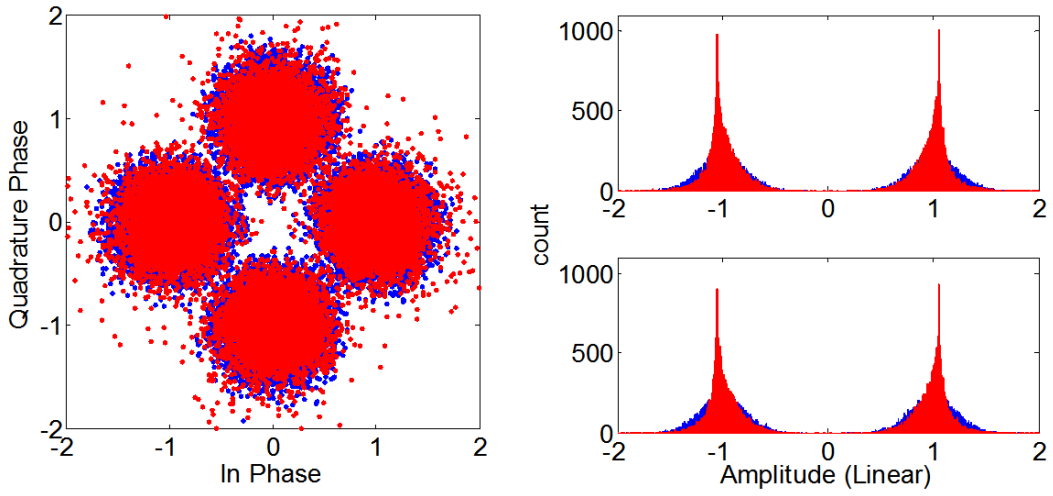

FIGURE 5.43: Signal before (blue) and after (red) the regenerator, a) Constellation diagram and b) in-phase axis histogram for an input SNR of 10.5 dB.

10.6 % and 4.3 %, respectively. The optimised harmonic mixing coefficient used here is $m = 0.1633$. Here a SNR improvement of 7.1 dB is achieved with a 2.1 and 2.5 times improvement in phase and amplitude noise distribution, respectively.

Fig. 5.43 displays point 3 on Fig. 5.40, with an input SNR, output SNR, input phase standard deviation, output phase standard deviation, input amplitude standard deviation and output amplitude standard deviation of 10.5 dB, 13.2 dB, 0.218 rad, 0.168 rad, 21.0% and 14.6 %, respectively. The optimised harmonic mixing coefficient used here is $m = 0.1020$. Here a SNR improvement of 2.7 dB is achieved with a 1.3 and 1.4 times improvement in phase and amplitude noise distribution, respectively.

QPSK Simulations

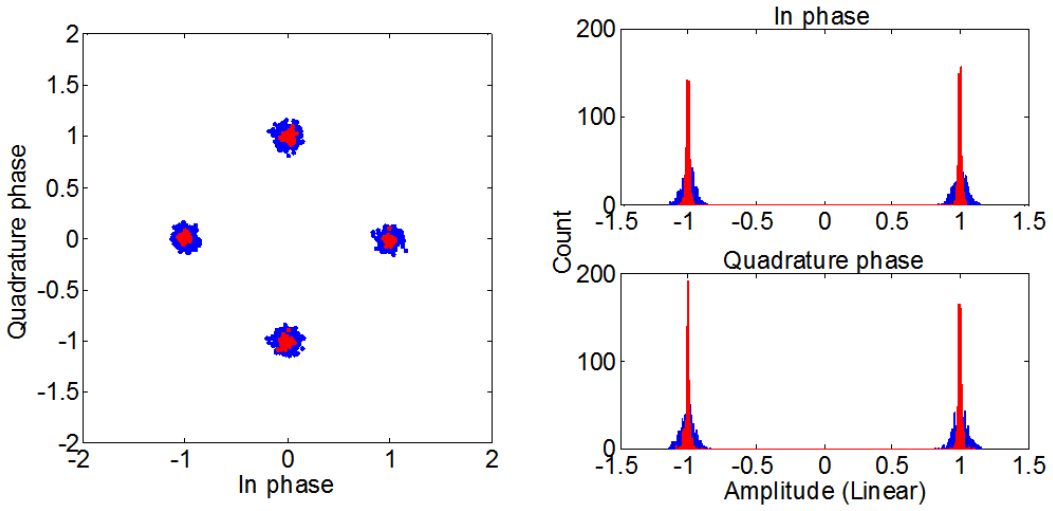

FIGURE 5.44: Signal before (blue) and after (red) the regenerator, a) Constellation diagram and b) in-phase axis histogram for an input SNR of 28.5 dB.

Similarly to the BPSK case, simulations using the setup shown in Fig. 5.34 were carried out for M = 4. The same HNLF parameters were used in this section. For the following simulations the initial pump power for the harmonic generation stage was 30 dBm, with an input signal power of 15 dBm. Higher input powers were required to generate sufficient conjugated fifth harmonic as compared to the BPSK case, where only the conjugated third harmonic was required. The initial pump power was kept at 30 dBm as higher power would be difficult to inject into the HNLF in a practical sense due to the SBS threshold of the HNLF. The pumps in the PSA stage were 15 dBm each, the signal power was reduced to 0 dBm and the conjugated fifth harmonic power was varied for best performance. The signal was centred at 1557 nm with a repetition rate of 40 Gbit/s. For each case 4096 symbols were considered. For the following figures the constellation diagram (left), in-phase axis histogram of the symbols on the in-phase axis (top right) and quadrature-phase axis histogram of the symbols on the quadrature-phase axis (bottom right) of the signal before (blue) and after (red) regeneration are displayed.

Fig. 5.44 displays the analysis of the signal with input SNR, output SNR, input phase standard deviation, output phase standard deviation, input amplitude standard deviation and output amplitude standard deviation of 28.5 dB, 38.83 dB, 0.0255 rad, 0.0065 rad, 2.73 % and 0.94 %, respectively. Here the conjugated fifth harmonic power at the input of the PSA stage was 6 dBm. Here a SNR improvement of 10.33 dB was achieved with a 3.9 and 2.9 times improvement in phase and amplitude noise distribution, respectively. Again, as with the BPSK case the analytical results show better regenerative performance than the simulated results.

Fig. 5.45 displays the analysis of the signal with input SNR, output SNR, input phase standard deviation, output phase standard deviation, input amplitude standard deviation and output amplitude standard deviation of 16.5 dB, 21.72 dB, 0.108 rad, 0.059

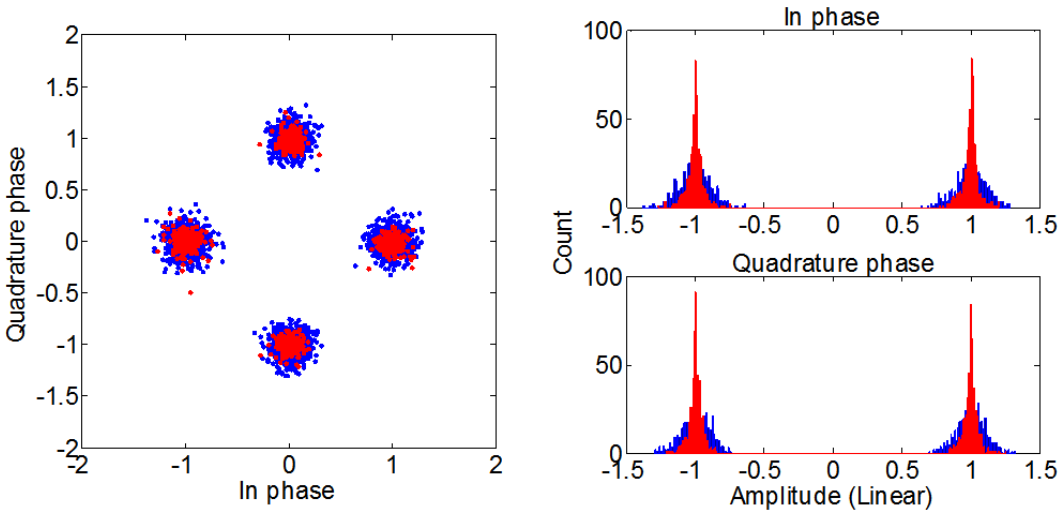

FIGURE 5.45: Signal before (blue) and after (red) the regenerator, a) Constellation diagram and b) in-phase axis histogram for an input SNR of 16.5 dB.

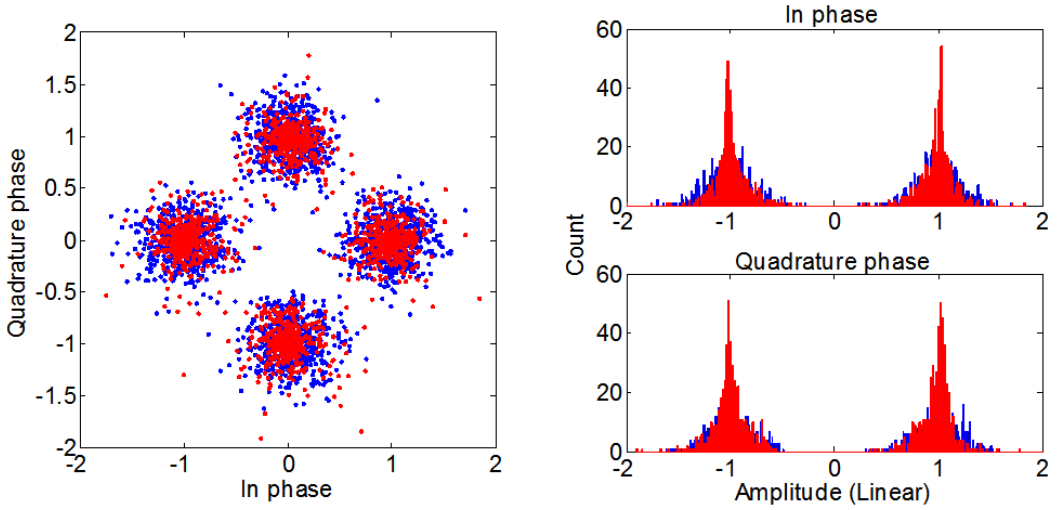

FIGURE 5.46: Signal before (blue) and after (red) the regenerator, a) Constellation diagram and b) in-phase axis histogram for an input SNR of 10.5 dB.

rad, 10.74 % and 5.72 %, respectively. Here the conjugated fifth harmonic power at the input of the PSA stage is 4.5 dBm. Here a SNR improvement of 5.22 dB is achieved with a 1.8 and 1.9 times improvement in phase and amplitude noise distribution, respectively.

Fig. 5.46 displays the analysis of the signal with input SNR, output SNR, input phase standard deviation, output phase standard deviation, input amplitude standard deviation and output amplitude standard deviation of 10.5 dB, 12.69 dB, 0.204 rad, 0.171 rad, 18.75 % and 15.95 %, respectively. Here the conjugated fifth harmonic power at the input of the PSA stage is 3 dBm. Here a SNR improvement of 2.19 dB is achieved with a 1.2 times improvement in both phase and amplitude noise distribution.

Again, a similar trend can be observed between the analytical and simulation analysis of this QPSK regenerator scheme. With lower input signal SNR the performance of

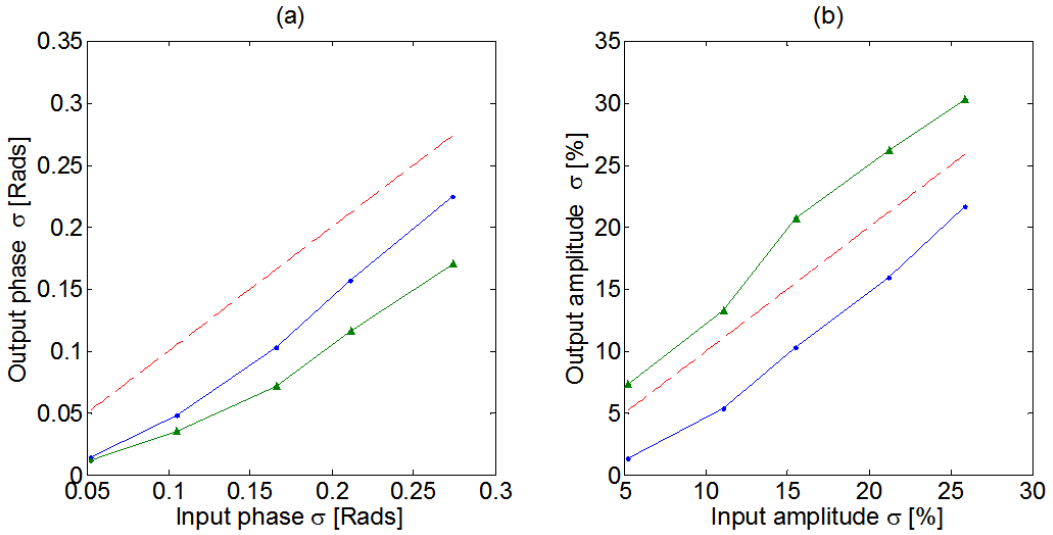

FIGURE 5.47: a) Phase standard deviation transfer function, b) amplitude standard deviation transfer function of the regenerator demonstrated here (blue) and the QPSK regenerator demonstrated in [9] 1:1 ratio represented by the red dashed lines

the regenerator reduced. Also, the optimal harmonic mixing coefficient (m factor in the analytical expression) reduces as the input SNR reduces.

Fig. 5.47 summarises the simulated phase (a) and amplitude (b) noise standard deviation transfer functions for the simultaneous amplitude and phase regenerator described in this section (blue) alongside the same information gathered by the operation of the phase regenerator demonstrated in [9] (green), these were simulated by myself explicitly for this comparison. The regenerator from [9] is implemented by a similar dual-pump nondegenerate PSA, where the harmonic coefficient used is the third harmonic, taking the general formula of (M-1)th. The frequency spacing, signal repetition rate, HNLF parameters were the same as the case simulated in this section. The regenerator was operated in an unsaturated regime were the power of the pump and the signal in the PIA stage were 30 dBm and 15 dBm, respectively. The pump powers in the second (PSA stage) HNLF were 15 dBm and the signal was reduced to 0 dBm. The third harmonic power was varied to offer best performance (around 0 dBm). The red dashed lines represent the 1:1 ratio.

Fig. 5.47 shows that the regenerator demonstrated in this section offers improvement in both the amplitude and phase noise standard deviation, whereas the regenerator demonstrated in [9] offers an improvement in phase noise standard deviation (up to 45% further improvement over the regenerator demonstrated in this section) and a deterioration in the amplitude noise standard deviation (due to phase-to-amplitude noise conversion effects). The average improvement in amplitude noise standard deviation of the regenerator demonstrated in this section over that demonstrated in [9] is 2.6. The average improvement in phase noise standard deviation of the regenerator demonstrated in [9] over that demonstrated in this section is 1.3.

5.4 Conclusion

This chapter contains two different PSA-based regenerators. In the first subsection a study was carried out into a wavelength converting idler-free phase regenerator. Here analytical, numerical and experimental data were compared resulting in a good understanding of the dynamics related to the secondary pump power and the regenerators' mixing coefficient m. The regenerator showed great power flexibility and good results for QPSK data. In the second subsection a study was carried out into a simultaneous phase and amplitude regenerator. Here results were compared from analytic and numerical simulations with and without data. Both BPSK and QPSK were compared, with an independent study conducted on the changes made to the perimeter of a single symbol for low, high and optimised harmonic mixing coefficients. Finally, simulations were carried out considering setups that could be feasible for future laboratory experiments.

Chapter 6

PSA based phase regeneration of a high-order M-PSK signal

6.1 Introduction

To date, optical regeneration of binary phase shift keying (BPSK) and quadrature phase shift keying (QPSK) signals has been successfully demonstrated exploiting the characteristics of either single- or dual- pump phase-sensitive amplification (PSA), implemented in either highly nonlinear fibers (HNLF) [2, 75], periodically poled Lithium Niobate (PPLN) waveguides [51, 79], or semiconductor optical amplifiers (SOA) [80, 81]. The regeneration of an M-PSK signal (where M is the number of phase levels used) is possible in principle in a dual pump PSA, but requires the generation of higher order phase harmonics [75], posing inherent practical difficulties. Indeed, the generation of high-order phase harmonics through four-wave mixing (FWM) can be limited by the fiber parameters and input power constraints. Very recently 16-QAM signals in both polarizations and up to three channels have been successfully processed in a copier-PSA configuration [51], however this comes with the compromise of doubling the bandwidth occupied by the system. In the literature, a suggested approach towards the regeneration of complex modulation formats is to first demultiplex the signal into simpler phase-only tributaries, before parallel regeneration and subsequent coherent recombination [69]. In this chapter, the same principle is followed and discussed in order to regenerate an M-PSK signal for $M = 2^k$, with k an integer. In this new scheme the second and third phase harmonics are generated in a FWM process where the M-PSK signal and a continuous wave (CW) beam are used as the pump and the FWM-seed signal, respectively. The generated second phase harmonic, which corresponds to a down-converted M/2-PSK signal [82], is subsequently partially regenerated before being coherently recombined with the third phase harmonic signal in another FWM process. As we will see in the following sections, the resulting idler is now the fully phase-regenerated original M-PSK signal.

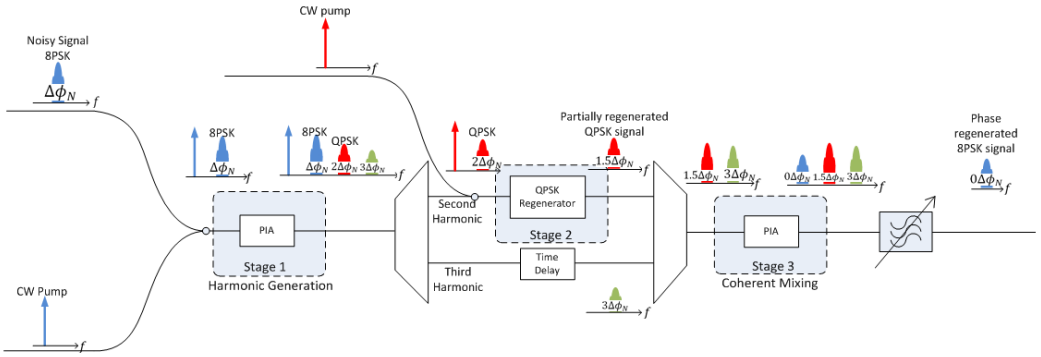

FIGURE 6.1: Operating principle and schematic diagram of the proposed M-PSK phase regenerator, adapted for an 8-PSK signal.

A key point of the scheme is that only partial regeneration of an M/2-PSK is required in order to fully regenerate an M-PSK signal with clear power budget advantages. It is quite intuitive that this scheme can then, in principle, be repeated (nested) several times in order to scale to ever higher values of M to allow the regeneration of signals of ever increasing complexity, albeit at the expense of more involved physical implementations.

6.2 Operating principle and setup

The operating principle of the proposed M-PSK phase regeneration scheme is depicted in Fig. 6.1 for the specific case of an 8-PSK signal. The figure also shows representations of the corresponding spectra at various points in the system which are be also highlighted by a diagrammatic spectral representation in Fig. 6.2. Fig. 6.2 displays the three stages of the regenerator, keeping in focus the spectral position of the various signals and harmonics. The evolution of the noise on the signal and (regenerated) harmonics is shown. The regenerator comprises three main stages: in the first stage, the 8-PSK signal and a CW pump are used as inputs in a FWM process (a phase-insensitive amplifier, PIA) to generate the second and third phase harmonics of the incoming 8-PSK signal. If the pump phase is assumed constant for the sake of clarity, and thus ignored, the phases of the second and third phase harmonics can be written as a function of the initial 8-PSK signal as follows:

$$\phi_{\text{second harmonic}} = 2\phi_{8PSK} \tag{6.1}$$

$$\phi_{\text{third harmonic}} = 3\phi_{8PSK} \tag{6.2}$$

Where ϕ_{8PSK} represents the original phase states of the input 8-PSK signal, depicted as the 'original signal' in Fig. 6.3. For example, for the second phase harmonic signal the phase states 0 and π are changed to 0 and 2π after the process (similar relationships apply to the remaining states, as shown in Table 6.1). As a consequence, the second

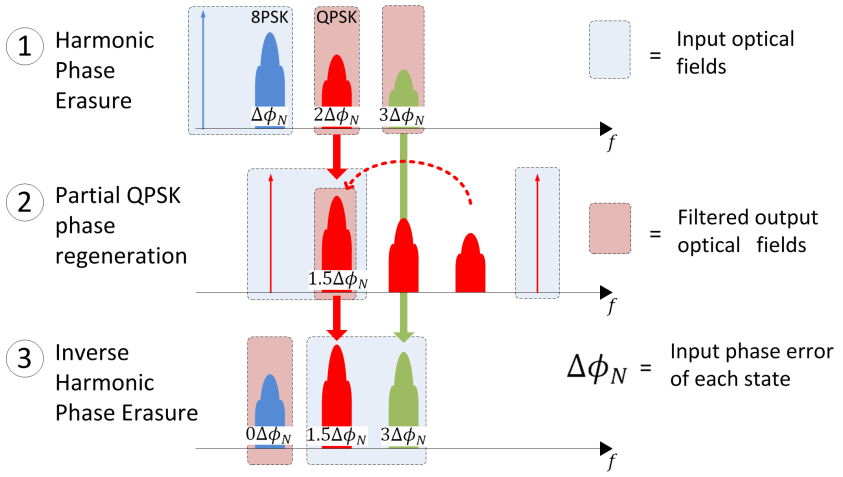

FIGURE 6.2: Diagrammatic spectral representation of the three stages within the regenerator, adapted for an 8-PSK signal.

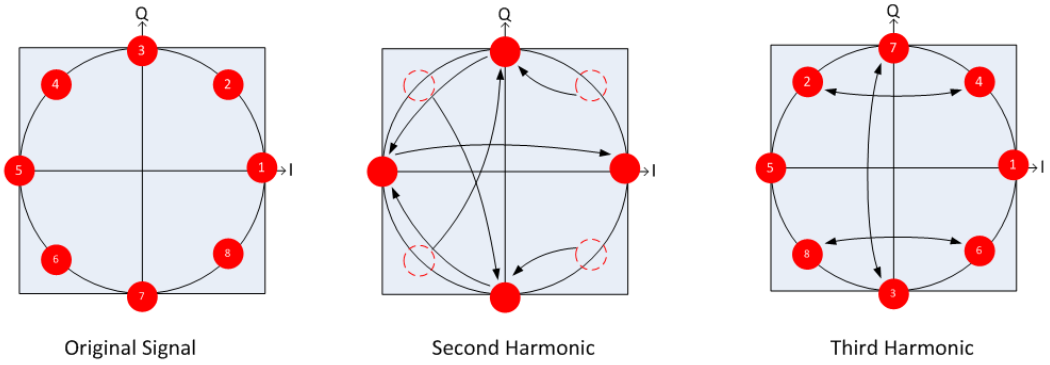

FIGURE 6.3: Constellation diagrams showing symbol placements for original signal (left), second (middle) and third (right) phase harmonics.

phase harmonic signal corresponds to an optically format down-converted 4-PSK signal (i.e. it takes the form of a QPSK signal). This transformation is pictorially represented in Fig. 6.3 in the form of the signal constellations. In the general case, the second phase harmonic term takes the form of a M/2-PSK signal. (It should be appreciated however, that this is only a virtual format conversion, since the M/2-PSK second phase harmonic signal cannot possibly contain the full information of the original M-PSK signal.) For the third phase harmonic, on the other hand, the nominal phase values are multiplied by three, and as a result, the third phase harmonic corresponds to a signal which is still in the form of 8-PSK (and M-PSK in the general case), but where the various symbol allocations have been shuffled in the constellation map, as also pictorially represented in Fig. 6.3. The corresponding nominal phase combinations between the various harmonics are also summarized in Table 6.1. In the second stage, the format converted QPSK signal (M/2-PSK in the general case) is partially phase regenerated. Meanwhile the third phase harmonic is simply temporally delayed to guarantee synchronization and temporal coherence with the partially regenerated second phase harmonic. Finally, in the third stage, the partially regenerated QPSK signal is coherently mixed with the

third phase harmonic in order to obtain the properly regenerated 8-PSK signal. This is achieved by using them as the pump and signal, respectively, in an additional PIA stage. The phase of the mixing output $\phi_{8PSK_{output}}$ can then be written as follows (again the pump phase is assumed constant):

$$\phi_{8PSK_{output}} = 2 * \phi_{reg-second-harmonic} - \phi_{third-harmonic} \tag{6.3}$$

Where, $\phi_{reg-second-harmonic}$ and $\phi_{third-harmonic}$ are the phase of the partially phase regenerated M/2-PSK signal and third harmonic, respectively. If Eq. 6.1 and Eq. 6.2 are substituted in Eq. 6.3, the following equation is obtained:

$$\phi_{8PSK_{output}} = 2\left(2\phi_{8PSK_{input}}\right) - 3\phi_{8PSK_{input}} = \phi_{8PSK_{input}} \tag{6.4}$$

Eq. 6.4 implies that in the noiseless case the original 8-PSK formatted signal will be obtained at the output of the system. In order to understand how regeneration is achieved, similar equations for the corresponding phase noise components associated with each of the nominal phase states need to be derived. For example, if each phase state of the original signal is characterized by an initial phase error $\Delta\phi_N$ (so that the actual relative value of the phase of the symbol is $\phi_{8PSK_{input}} + \Delta\phi_N$), the second (third) phase harmonic will have twice (three times) that very same phase error. Bearing this in mind and considering Eq. 6.3, it can be deduced that to achieve optimum phase squeezing capability (where the output phase noise tends to zero), i.e. the minimum phase error for each nominal phase state, the phase noise error of the format converted signal (second harmonic) is required to be only partially regenerated (by 25%). With this partially regenerated phase error of the second phase harmonic (i.e. $2\Delta\phi_N$ becoming $1.5\Delta\phi_N$), a similar equation to Eq. 6.3 can be written to represent the output phase error of each state:

$$\Delta\phi_{N_{output}} = 2\left(1.5\Delta\phi_N\right) - 3\Delta\phi_N = 0 \tag{6.5}$$

It is worth highlighting that the phase noise of the second (third) phase harmonic needs to have exactly twice (three times) the phase noise distribution for correct phase noise cancellation. This regeneration technique can be extended, such that the process of harmonic phase generation, partial regeneration and recombination can be nested to allow the use of even lower level regenerators. For instance, the QPSK signal resulting from format conversion, in the case described above, can be further down-converted to a BPSK signal. This BPSK signal can be partially regenerated (by a factor which can be calculated to be 6.25% following the same methodology as above) and then sequentially recombined with the third phase harmonics of each nested stage to generate the phase regenerated 8-PSK signal. It is worth highlighting that no specific phase or frequency relation is required between the pumps in Stage 1 and Stage 2, and also that in the simulations (introduced in section 6.3) the pumps have been assumed ideal with no associated phase and/or amplitude noise.

TABLE 6.1: Individual symbol phase values

Symbol	Input signal phase [^{o}]	2^{nd} Harmonic (SH) phase [^{o}]	3^{rd} Harmonic (TH) phase [^{o}]	2x(SH)-(TH) phase [^{o}]
1	0	0	0	0
2	45	90	135	45
3	90	180	270	90
4	135	270	45	135
5	180	0	180	180
6	225	90	315	225
7	270	180	90	270
8	315	270	225	315

6.3 Results and discussion

Detailed simulations to prove the validity of the proposed approach were carried out and presented in this section. These simulations assumed a set-up that followed the schematic shown in Fig. 6.1. A non-return-to-zero (NRZ) 25 GBaud 8-PSK signal at 1557 nm was combined with a CW pump at 1552 nm before entering the phase harmonic generation stage. For the nonlinear element in the first stage, as well as in all the others included in the set-up, typical parameters of a state-of-the-art strained HNLF, available in many laboratories, were used. In particular the same parameters of the HNLF were used for all the three stages of the setup exhibiting a dispersion, dispersion slope, zero dispersion wavelength, nonlinear coefficient, linear loss and length of -0.08ps/nm/km, 0.018ps/nm^2/km, 1553nm, 11.6/W/km, 0.88dB/km and 0.3 km, respectively [75]. The fiber SBS threshold (after straining) was 27 dBm. The second and third order phase harmonic signals, which were produced in the first PIA, were then demultiplexed; the second phase harmonic (the format down-converted QPSK signal) was partially regenerated using a dual-pump non-degenerate PSA as described in [75]. The maximum power used for the two phase-locked pumps for this PSA was 24 dBm each, while the power of the signal was 10 dBm. These power relations ensured that the signal was only partially regenerated at the output of the PSA and far from saturation of the pumps (optimum phase regeneration would require a power of 27 dBm on each of the pumps). In parallel, the third phase harmonic was propagated through a standard single mode fiber (SSMF) in order to properly match the two path lengths. The partially regenerated second phase harmonic was coherently mixed with the third phase harmonic in a last PIA stage to reconstruct the 8-PSK with regenerated phase at exactly the original wavelength. Fig. 6.4 reports the amplitude and phase responses of the proposed system. In particular, Fig. 6.4 (a) shows the output phase transfer function as a function of the input signal phase between $-\pi/8$ and $+\pi/8$ radians. The blue dots represent the numerical simulations and the red line represents the analytical fit. To obtain this fit, the signals after the partial QPSK regenerator and at the output of the system were represented by their amplitude (A_{pr} and A_{out}) and phase (ϕ_{pr} and ϕ_{out}) transfer profiles,

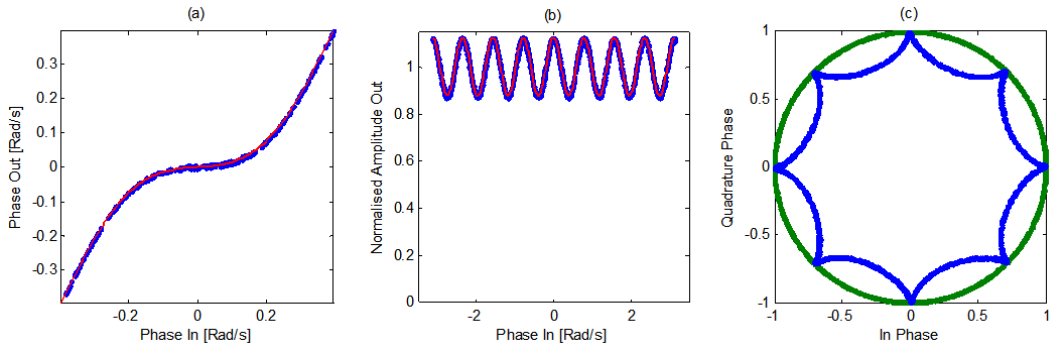

FIGURE 6.4: Simulation in blue, analytic fit in red repeating for the case of m=0.069 a) Phase transfer function versus input phase between $-\pi/8$ and $\pi/8$ rads, b) Amplitude phase transfer function versus input phase and c) full phase spread constellation diagram of input (green) and output (blue).

as follows:

$$A_{pr}e^{i\phi_{pr}} \propto e^{i(2\phi_s)} + me^{-3i(2\phi_s)} \tag{6.6}$$

$$A_{out}e^{i\phi_{out}} \propto A_{pr}^2 e^{i(2\phi_{pr}-3\phi_s)} \tag{6.7}$$

where ϕ_s is the phase of the initial 8-PSK signal and m is the optimum mixing ratio which related to the gain of the PSA process as defined in [75]. The optimal value for the m factor, which was used to calculate the corresponding transfer functions displayed in Fig. 6.4, is m =0.069. As compared to the optimal value of m =0.33 required for full QPSK regeneration (as estimated in [77]), this is much lower, as expected, since only partial regeneration is needed. The system implication is that Stage 2 requires lower pump powers than traditional QPSK regenerators [77], in order to achieve the optimum overall phase transfer function. However, the trend of the various transfer functions as m increases are very similar in the two regenerators. Examples of the phase transfer functions for four values (0, 0.069, 0.13 and 0.33) of m are depicted in Fig. 6.5, at different points of the system. Fig. 6.5a) displays the single step (between $-\pi/4$ and $\pi/4$ radians) phase transfer function for the four m values directly after the QPSK regenerator (output of Stage 2). Fig. 6.5b) displays the corresponding single step (between $-\pi/8$ and $\pi/8$ radians) phase transfer function for the four m values for the final 8-PSK signal (output of Stage 3). Fig. 6.5 together show the minimal amount of regeneration necessary in Stage 2 to achieve optimal (and over) regeneration considering the whole system. Fig. 6.4(b) shows the numerical simulation and analytic fit of the output amplitude as a function of the input phase between $-\pi$ and $+\pi$ radians. As expected the amplitude of the synthesized signal becomes a cosine function of the phase with a periodicity of $2\pi/M$. Fig. 6.4(c) displays how the input signal (green) with induced continuous phase variations from 0 to 2π is shaped at the output (blue) of the (fully regenerated) system, at the optimal mixing factor (m =0.069).

Figs. 6.6, 6.7 and 6.8 present constellation diagrams at the input (a) and output (b) of the 8-PSK regenerator for three different values of phase noise with a constant (flat-top)

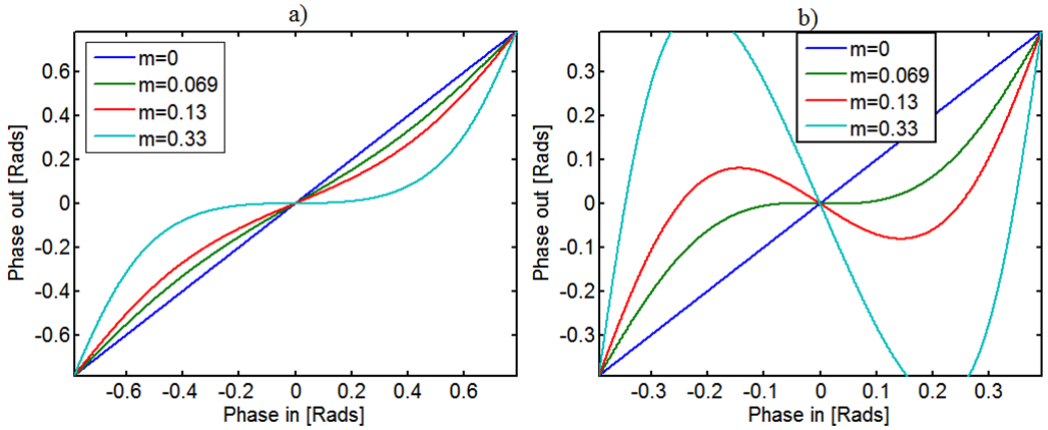

FIGURE 6.5: Single step phase transfer function of the a) QPSK signal after Stage 2, and the b) final 8-PSK signal, with m factor set to 0 (blue), 0.069 (green), 0.13 (red) and 0.33 (teal).

probability density function of 0.062, 0.098 and 0.124 radians, respectively, added to the signal, highlighting the regenerator performance. No amplitude noise was considered at the input in this instance and different m factor values were considered for the various studied cases in order to minimise the output phase noise. In particular, as the amount of phase noise increases, higher m factor values had to be chosen to minimise the output phase noise. Specifically for Figs. 6.6, 6.7 and 6.8 the m factor values used were 0.069, 0.085 and 0.13, respectively. At the output of the regenerator the phase noise distribution was reduced to 0.006, 0.016, 0.042 radians in these three respective cases. This is clearly understandable from Fig. 6.5b), where it can be seen that for relatively low phase noise at the input of the system the optimum phase transfer function corresponds to m =0.069. This translates all of the phase noise present at the input into amplitude noise via a cosine function (Fig. 6.4b)) as depicted in Fig. 6.6. As the input phase noise further increases, the transfer functions with higher m values accommodate more input phase noise variation for fewer output phase noise variation, and are thus preferable. Also in Fig. 6.5b) it can be seen that for m>0.069, the transfer function does not increase monotonically and two different values of input phase correspond to the same value of output phase. This effect on the constellation diagram is visualised as an elliptical shape of the constellation symbols that get more and more pronounced as the m factor increases, as displayed in Figs. 6.7b) and 6.8b).

The regenerator was then fully characterized for various levels of initial Gaussian distributed phase noise added to the signal. Again no amplitude noise was added to the signal for this study. The corresponding standard deviations of the phase and amplitude noise at the output of the system as a function of the input phase noise standard deviation are summarised in Fig. 6.9. The output phase noise stayed reasonably constant up to an input phase noise standard deviation of 0.065 radians, achieving a reduction in the phase noise by as much as 7.1 times. For all these measurements the value of the m factor value was kept constant around m =0.069. Beyond this value of input phase

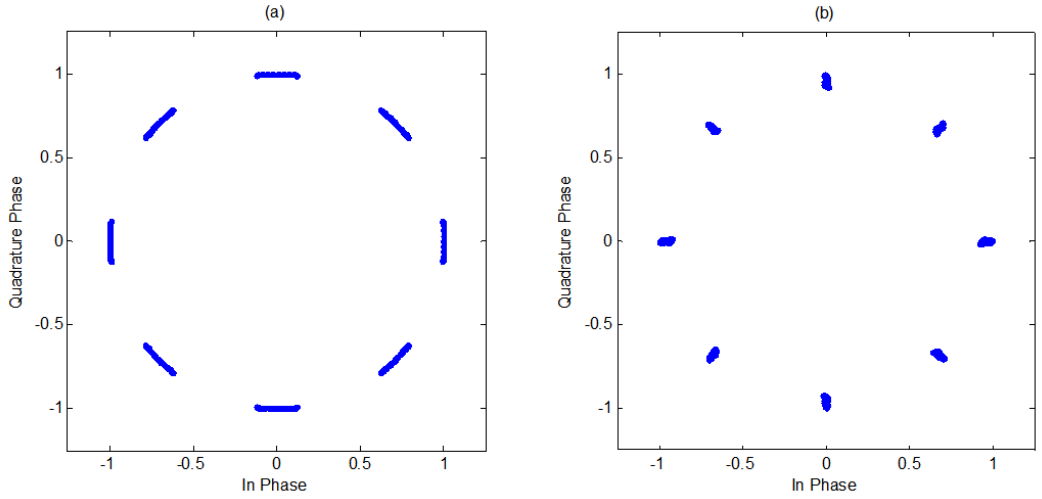

FIGURE 6.6: Example of constellation diagrams at the input (a) and output (b) of the system when a phase noise of 0.062 radians (with a constant probability density function) is added to the signal.

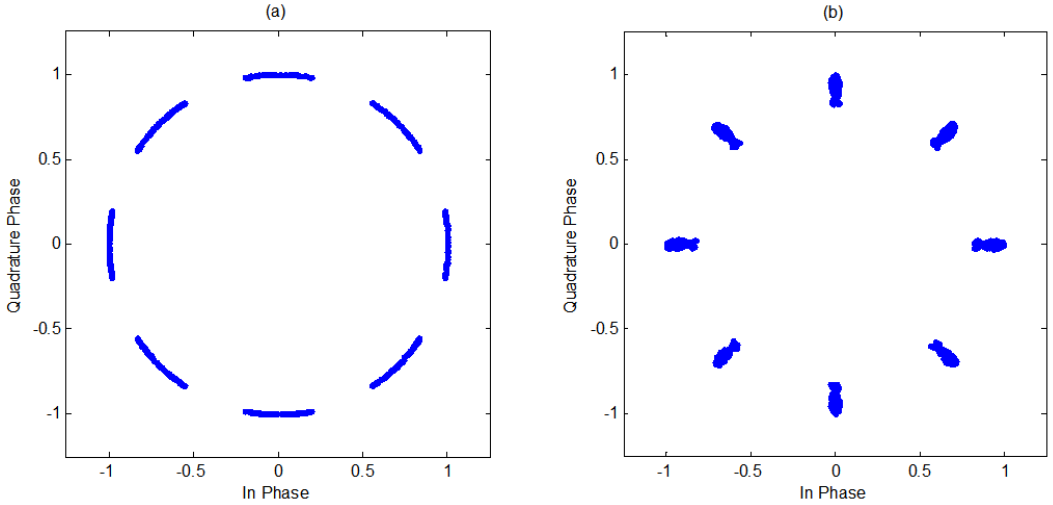

FIGURE 6.7: Example constellation diagrams at the input (a) and output (b) of the system when a phase noise of 0.098 radians (with a constant probability density function) is added to the signal.

deviation higher values of m had to be used, it was observed that the output phase noise slightly increased with input signal phase noise, however a reduction of almost 3 times for the worst case examined was still achieved, corresponding to an input phase noise standard deviation of 0.124 radians. The reason for the increased output phase noise is the non-monotonic curve of the transfer function in Fig. 6.5b) at m factor values greater than 0.069, as previously discussed. The red dotted line denotes the 1:1 ratio and the region below it represents the area where phase regeneration occurs. On the other hand, unless saturation is achieved, phase-to-amplitude noise conversion takes place via the cosine transfer function shown in Fig. 6.4(b), as discussed previously. This effect can also be clearly seen in Fig. 6.6, 6.7 and 6.8. In this scheme, the PSA-based partial phase regenerator was intentionally operated in the linear regime to guarantee correct overall

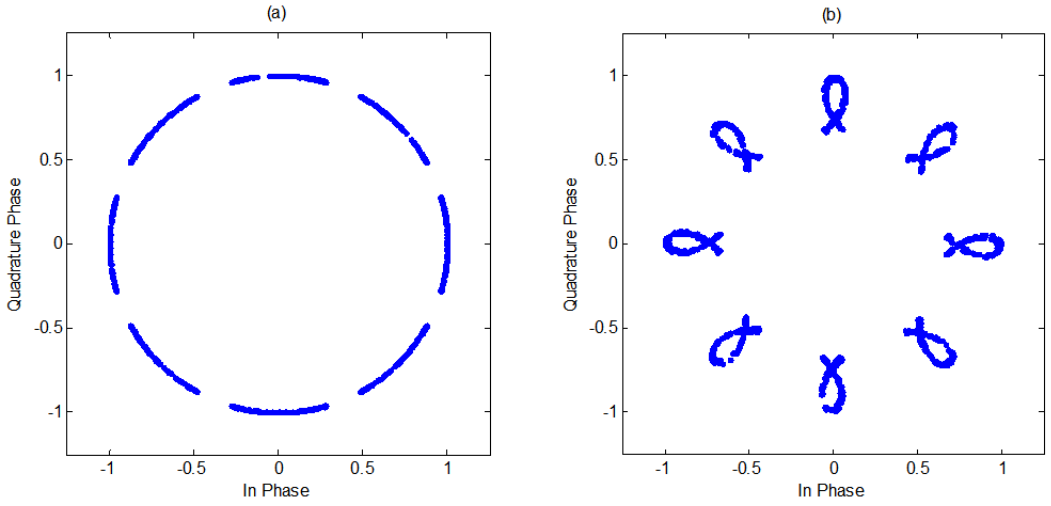

FIGURE 6.8: Example constellation diagrams at the input (a) and output (b) of the system when a phase noise of 0.124 (with a constant probability density function) is added to the signal.

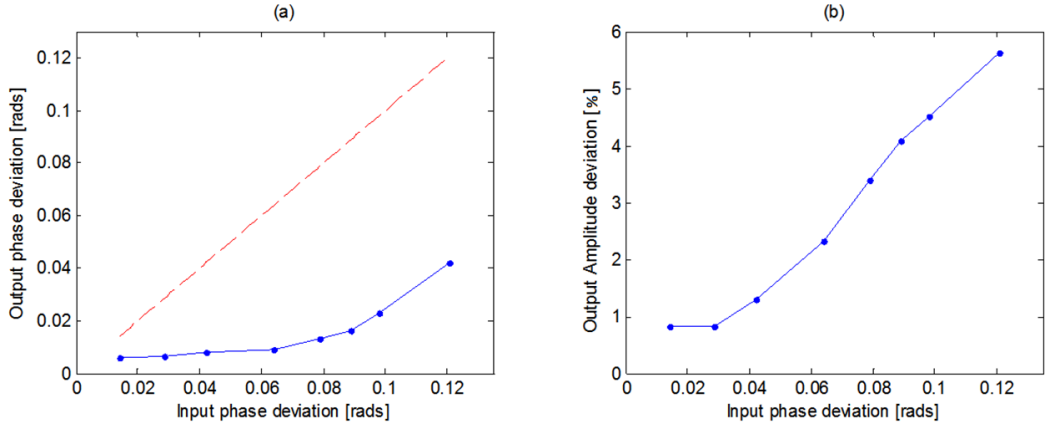

FIGURE 6.9: Output phase standard deviations versus initial phase standard deviations (a) and normalized output amplitude standard deviations versus initial phase standard deviations (b).

phase noise cancellation. It is noted however, that this undesired phase-to-amplitude conversion effect could be reduced drastically if a more complex PSA scheme, including an extra phase harmonic, was considered, as proposed and demonstrated in [25, 83].

Finally, the system was numerically characterized for the case when both Gaussian phase and amplitude noise was added to the 8-PSK input. The standard deviation of the phase and amplitude noise assumed was 0.064 radians and 6%, respectively.

Fig. 6.10 displays the constellation diagrams of the input and output of the system with the added Gaussian amplitude and phase noises. It is clear from Fig. 6.10b) that the phase noise has been reduced, but at the cost of drastically increasing the amplitude noise.

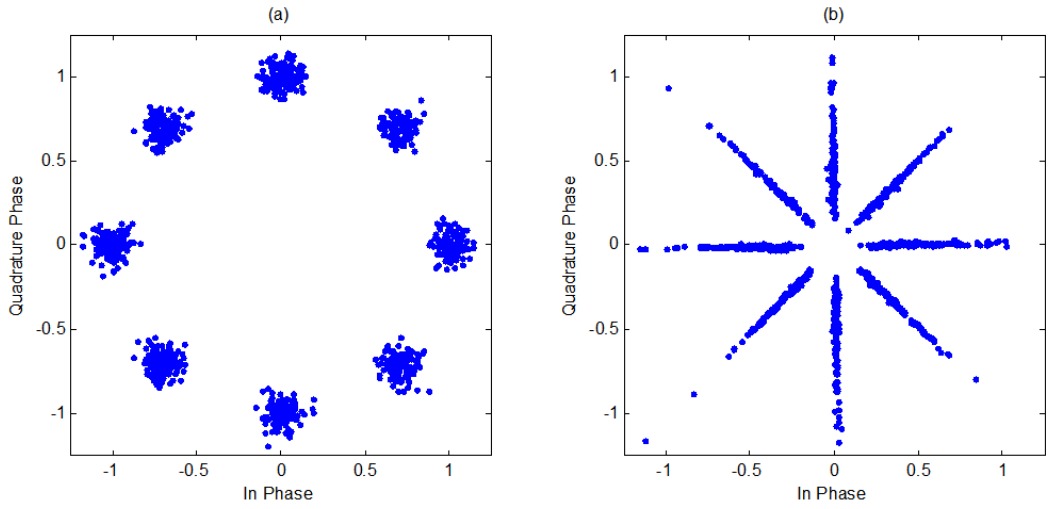

FIGURE 6.10: (a) Input and (b) output of the system when Gaussian phase and amplitude noises with standard deviations of 0.064 radians and 6%, respectively, were added to the signal.

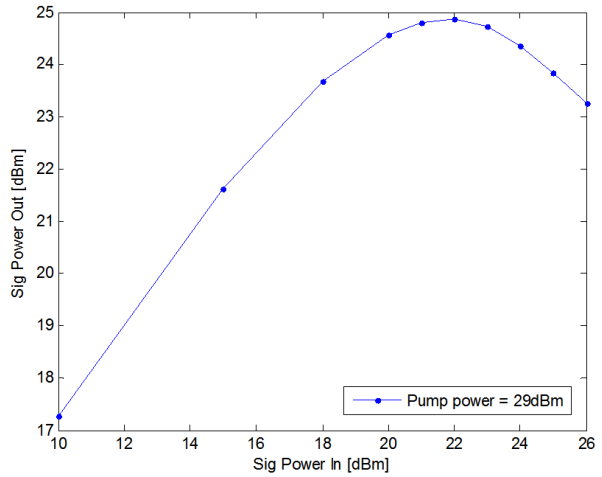

FIGURE 6.11: Signal power transfer function for the saturated single-pump parametric amplifier based amplitude limiter, with pump power at 29 dBm.

Since the proposed phase regenerator scheme amplifies the input amplitude noise (due to the phase-to-amplitude noise conversion in Stage 2 and the FWM-induced amplification of amplitude noise from Stage 1 and Stage 3 (as seen in Fig. 6.1)), it was considered imperative to firstly reduce the amplitude noise on the signal present at the input of the regenerator. An amplitude limiter based on a saturated single-pump parametric amplifier was then implemented, consisting of a single HNLF (with the same characteristics as in the remaining sections), pumped by a CW signal with a power level of 29 dBm (ignoring any SBS effects) at 1552 nm. The power transfer function of this system is shown in Fig. 6.11.

Fig. 6.11 shows a plateau in the signal power transfer function at an input signal power of around 22 dBm. Fig. 6.12 shows the corresponding regenerative performance of the amplitude limiter mentioned above when only amplitude noise with constant (flat-top)

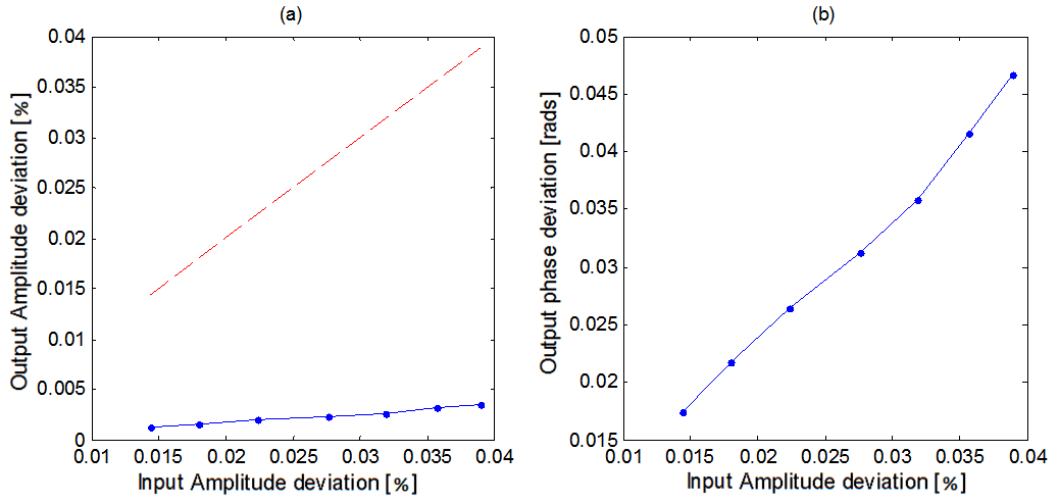

FIGURE 6.12: a) Amplitude standard deviation transfer function and b) output phase standard deviation versus input amplitude standard deviation of the amplitude limiter.

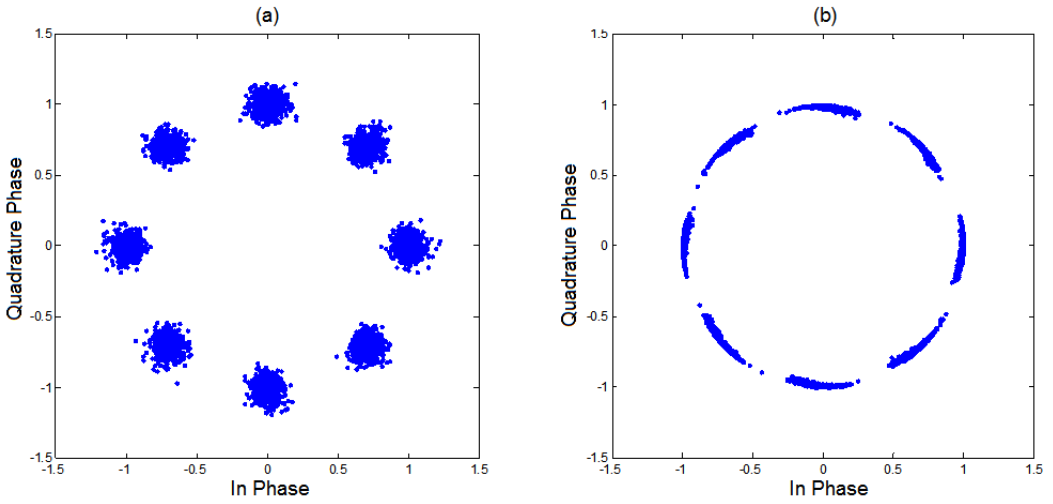

FIGURE 6.13: a) Input and b) output signal constellations of the amplitude limiter.

probability density function was considered. Fig. 6.12a) shows the amplitude noise standard deviation transfer function as the amplitude noise varies, where the red dashed line represents the 1:1 ratio. Fig. 6.12b) shows amplitude-to-phase noise conversion of the amplitude limiter due to SPM effects. Different amplitude limiters could be chosen with further reduced amplitude-to-phase conversion [3].

Fig. 6.13 shows the input (a) and output (b) signal constellations of the saturated single-pump parametric amplifier based amplitude limiter for the same input signal amplitude and phase noise discussed in Fig. 6.10a). The non-uniform phase noise distribution after amplitude regeneration that can be seen in the constellation of Fig. 6.13b) is due to the effects of SPM in the saturated FWM system.

Fig. 6.14 displays the corresponding constellation diagrams at the input (a) and output (b) of the complete 8-PSK regenerator, comprising the amplitude limiter and the

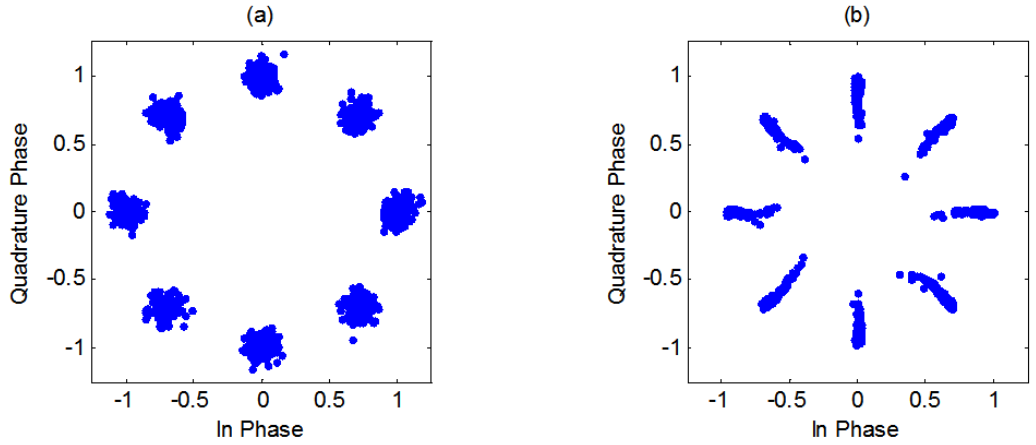

FIGURE 6.14: Examples of constellation diagrams at the input (a) and output (b) of the system when Gaussian phase and amplitude noises with standard deviations of 0.064 radians and 6%, respectively, were added to the signal.

previously discussed phase regenerator. At the output of the regenerator the signal phase and amplitude noise deviations were 0.014 radians and 8.75%, respectively. Consequently, the phase deviation was reduced by a factor of 4.5, while the amplitude noise was increased slightly by a factor of 1.5.

Some practical issues relating to this scheme are imposed by the need to preserve coherence among the different paths in the second stage of the system in Fig. 6.1. In these simulations, HNLFs have been considered, however in order to ensure that the signals traversing the various paths are added coherently, photonic integrated solutions would provide far better stability in practice.

6.4 Conclusion

The scheme proposed in this chapter demonstrates a phase regeneration technique that allows an M-PSK signal to be regenerated using an M/2-PSK (or an even lower order) partial regenerator. The technique requires a three-stage coherent process. Firstly, a single pump parametric amplifier is used to produce the two spectral phase harmonics of interest, the second and third phase harmonics. Secondly, the second (down-converted) phase harmonic is partially regenerated using a M/2-PSK regenerator. A dual-pump PSA was used in this case as proposed in [9], but a more complex configuration based on three pumps [25] could have been used to reduce the phase-to-amplitude regeneration in the partial regenerator stage. Thirdly, the third phase harmonic and the partially regenerated second phase harmonic are used as the signal and pump, respectively, in a last FWM stage where the original signal is recovered at the very same wavelength. If the incoming signal exhibits amplitude noise, an amplitude limiter must be considered at the very beginning of the system as it was demonstrated in the previous section.

Chapter 7

Conclusions

This thesis introduces schemes for the synthesis and regeneration of advanced optical modulation formats using all-optical signal processing. Several different all-optical regeneration techniques mainly based on phase sensitive amplifier configurations have been successfully developed and implemented for various optical modulation formats.

In the introduction to this thesis a brief history of the technologies that went into creating the modern day optical telecommunications infrastructure are highlighted. The motivation for the work presented in this thesis is discussed from a socio-economic and technologically feasible paradigm. Some limiting factors with high speed electronics were highlighted, with the onus put onto describing the possible improvements using all-optical signal processing and what it could bring to next generation optical communication systems. The recent benchmarks in fibre capacity and transmission length are graphically displayed showing the high capacity length products achieved by both single and multi-mode/core fibres. The research aims were discussed with a detailed introduction of the key features of phase sensitive amplifiers that constitute the building blocks of many demonstrations that were discussed in this thesis.

The thesis begins with a review of the main theory that needs to be understood for the comprehension of the work performed. An introduction into the description of the fundamentals of wave propagation in an optical fibre followed by different effects of dispersion are highlighted. Nonlinear refraction is discussed alongside self and cross phase modulation. An analytical explanation of four wave mixing and fibre optic parametric amplifier gain characterisation are offered such that phase sensitive amplification can be more understood. This is followed by the description of some of the inelastic scattering mechanisms in optical fibres, namely simulated Raman scattering and stimulated Brillouin scattering. The Nonlinear Schrödinger equation is introduced and its solution using the split-step Fourier method is described, which is used within this thesis to perform simulations of parametric devices used for regeneration. Optical injection locking is

briefly introduced within this chapter. A number of optical modulated signals are introduced and described. Noise degradation within a communication system is discussed as this has been be of importance when transmission experiments were conducted. Finally, some literature review of optical regeneration is reported which is an important topic in this thesis.

The work within the third chapter has provided experimental tools to emulate/generate more advanced modulation formats from an original BPSK signal, which provides modulation format flexibility as an alternative to using expensive dedicated transmitters. This work includes higher modulation format emulation of both QPSK and 16-QAM signals, combined with a detailed demonstration of an opto-electric feedback system successfully used to stabilise the emulated signals. Similarly, modulation format conversion and packet compression where achieved, allowing a method to temporally interleave format converted signals to increase signal spectral efficiencies. A broadband phase noise source based on XPM induced in a HNLF, between an ASE noise source at variable bandwidth and a signal, has been used to apply broadband phase noise onto the designated signal. This noise source scheme was used to emulate noise in a novel W-type PSA based all-optical phase regenerator.

In the fourth chapter, two phase-preserving amplitude regenerators were discussed and studied. Firstly, a dual pump signal degenerate PSA configuration has been used to generate a nonlinear signal power transfer function that exhibits a multilevel profile suitable to regenerate the amplitude of 4-ASK signals. This is achieved by a combination of SPM and XPM effects which induced phase dependent amplification/de-amplification along with the effects of pump depletion. The inter-symbol phase difference of the 4-ASK signal was characterised with the understanding that phase preservation is a requirement for amplitude regeneration of phase encoded signals. Due to the influence of both SPM and XPM on the signal field, there was an unacceptable degree of inter-symbol phase difference observed while operating within the plateau regions, making this scheme unsuitable for the processing of these signals. The experimental validation results were in good agreement with the corresponding numerical studies.

Secondly, the noise response of an OIL scheme was characterised to evaluate its performance as an amplitude regenerator. Different values of OSNR of the injected signal (master source to the OIL system) were considered. After regeneration, a reduction in the rms amplitude noise by a factor of 2 was achieved, albeit with a slight deterioration in the rms phase noise by a factor of only 1.1, for master signal OSNR values between 20 dB and 14 dB. Receiver sensitivity improvements up to 1 dB for the same OSNR values were achieved. The performance of the regenerator was subsequently assessed in a 600 km installed link (the Aurora dark fibre link), demonstrating the robustness of the implementation. It offered approximately a 1 dB power penalty improvement (at BER=10^{-4}) as compared to its output without regeneration.

The fifth chapter contains work from two areas. In the first subsection a study was carried out towards a wavelength converting idler-free phase regenerator where the scheme is notable for its low power operation, compactness and flexibility in the choice of operation power. Analytical, numerical and experimental data were compared resulting in a good understanding of the dynamics related to the pump power levels to be used corresponding to the optimum regenerators mixing coefficient 'm'. I have proposed the idea and carried out the numerical studies, while Mr Kyle Bottrill, another PhD student, has carried out the corresponding experiments to assess the scheme for static as well as dynamic characterisations using a QPSK signal as input. In particular, using the system as a regenerator BER measurements were taken for QPSK data loaded with broadband phase noise, illustrating that for an input signal with phase error equal to 11^o rms, the phase error can be reduced by half and receiver sensitivity can be decreased by 5.6 dB for a BER of $1x10^{-4}$. It is worth mentioning that this phase regenerator has been combined with a (separate) amplitude regeneration stage, which was based on saturated pump-depletion FWM [84]. However, the demonstration of this all-optical phase and amplitude regenerator is out of the scope of this thesis, but clearly highlights the importance of achieving simultaneous phase and amplitude noise suppression for unlimited transmission.

In the second subsection of the fifth chapter a different scheme was studied to simultaneously achieve phase and amplitude regeneration. Here the M+1^{th} phase harmonic was phase shifted by π radians and coherently added back with the original signal. Firstly, a harmonic generation stage was used to generate the conjugated M+1^{th} phase harmonic. A dual-pump non-degenerate FWM scheme was used to perform the coherent addition after the M+1^{th} phase harmonic has been properly phase shifted. Here results were compared between analytical and numerical simulations for both static and dynamic components. Both BPSK and QPSK were compared, with an independent study conducted on the changes made to the perimeter of a single symbol for low, high and optimised harmonic mixing coefficients.

The sixth chapter contains a demonstration of a phase regeneration technique that allows an M-PSK signal to be regenerated using an M/2-PSK (or an even lower order) partial regenerator. The technique requires a three-stage coherent process. Firstly, a single pump parametric amplifier is used to produce the two spectral phase harmonics of interest, the second and third phase harmonics. Secondly, the second (down-converted) phase harmonic is partially regenerated using a M/2-PSK regenerator. A dual-pump PSA was used in this case as proposed in [9]. Thirdly, the third phase harmonic and the partially regenerated second phase harmonic are used as the signal and pump, respectively, in a last FWM stage where the original signal is recovered at the very same wavelength. If the incoming signal exhibits amplitude noise, an amplitude limiter (for example similar to the one demonstrated in chapter 4) must be considered at the very beginning of the system.

In order to experimentally implement the regeneration of higher order modulation formats following the process detailed in this chapter, it will be important to drastically reduce the length of the nonlinear media of each stage, such that the path length mismatches between co-propagating optical fields can be minimised. This can be achieved by moving to waveguide technologies, which offer very high nonlinear coefficients and short propagation lengths [85]. Indeed the recent advances and maturity of silicon photonics technologies have led to the fabrication of small, low cost, CMOS-compatible devices. These features together with the ultra-high χ^3 nonlinearity of silicon, have allowed the use of silicon photonics as an attractive platform for all-optical nonlinear applications. For example, a PSA using pulsed pumps has been demonstrated in a silicon germanium waveguide [86] or PSAs using CW pumps have been demonstrated using a silicon waveguide with a reversed bias p-i-n junction to minimise free carrier absorption [87] or in a passive low-birefringent SiGe waveguide using a polarisation assisted PSA configuration [88]. These waveguide-based PSA demonstrations highlight the potential for a future all-optical signal processing shift into waveguide technologies.

To scale to higher modulation formats (M-PSK signals in this instance) the main limitation comes from the ability to generate high enough phase harmonics in the FWM process. For example, the phase regeneration of a 16-PSK signal requires the generation of the 15^{th} phase harmonic and this harmonic needs to be coherently added back to the original signal. However, it is worth noting that it is possible to phase regenerate a 16-PSK signal by combining the 7^{th} harmonic on the pump side ($\exp(7i\phi)$) and the 9^{th} harmonic on the signal side ($\exp(-9i\phi)$), which are easier to generate, however the symbols get reordered in a known fashion and this regenerator type is less susceptible to phase noise as outlying phase points can be spread across numerous other symbols. The work presented in the sixth chapter of this thesis aims to address this issue, proposing a way to deal (regenerate) with higher order modulation formats using a regenerator for lower order modulation formats.

Another key feature of all-optical regenerators that has not been addressed within this thesis should be the ability to scale the system to multichannel operation. Most PSA experiments reported in the literature have supported single channel operation with only a few attempts to simultaneously regenerate two or more channels in a single device [54, 55, 89, 90], highlighting the challenges faced when attempting to achieve multichannel operation. For example in [89], two scalar PSAs, sharing one pump, were used to demonstrate simultaneous regeneration of two channels, mainly limited by the strong pump-to-pump and pump-to-signal FWM interaction over a large bandwidth. In [54] the simultaneous regeneration of up to six channels in a single nonlinear medium has been successfully achieved in a polarisation assisted PSA, together with bidirectional propagation and careful placement of the pump signal wavelengths. In [55] the simultaneous regeneration of four channels has been experimentally represented using optical Fourier transformation and PSA.

Yet another limitation to the PSA-based phase regenerator, when scaled to higher order modulation formats, is the drop off in step-like (reduction in steepness) phase transfer function. An ideal step-like phase transfer function can be achieved for BPSK signals (M=2), however for ever increasing PSK modulation format complexity (M> 2) the phase transfer response becomes increasing less step-like. There are several possible solutions to achieving a more step-like phase transfer function. Firstly the signal can be chosen to be regenerated several times, with concatenated regenerators, taking the output of one regenerator as the input to the next [91] (ensuring the harmonic mixing coefficient is not selected at too high a value). After every successive regeneration the phase transfer function will become increasingly step-like. The drawback to this is that the cost, complexity and power usage scales with every successive regenerator used. Secondly, a different solution that only applies to square-QAM signals involves deconstruction of the signal into its constituent QPSK/BPSK signals. For example a 16-QAM signal can be deconstructed into four BSPK signals using an extension of the methods shown in [92]. Here each BPSK signal can be regenerated with the ideal step-like phase transfer function before being coherently added back together to achieve the original 16-QAM signal. The drawback to this method is that extreme care would have to be taken to ensure the temporal coherence of the four deconstructed regenerated BPSK signals when coherent addition takes place. Thirdly, a technique which includes a PSA system (detailed in [9]) with a optical injection locking amplitude limiter is discussed in [93].

Finally, it is worth assessing whether the power efficiency of all-optical signal processing would compare well against its electronic counterparts. It is fair to say that as the spectral efficiency increases, either through higher data rates and/or higher modulation format transmission, the power efficiency swings in favour of the all-optical signal processing. This statement can be realised as the speed of all-optical signal processing is limited by the fempto-second (PHz) response of optical processes whereas digital signal processing speeds are sub 100 GHz. All-optical signal processing is potentially competitive with electronic signal processing as long as the signal processing function is simple. In general, when considering the energy consumed, complex processing functions requiring several operations on each bit are more efficiently performed using electronic rather than optical signal processors [94]. As DSP operates upon electronic signals, not optical ones, its use implies a potentially energy inefficient conversion back and forth between the optical and electrical domains with relative limited electrical bandwidth. On the other hand, all-optical solutions, such as signal regeneration, where the signals remain in the optical domain at all times, are characterised by very broad bandwidth of operation. Similarly, all-optical signal processing can also potentially offer reduced latency as compared to DSP.

Appendix A

DLI Stabilisation

Fig. A.1 shows a schematic for two separate TAs, the DAQ card and the voltage following current booster, this has been built and is used as a subsection of the entire DLI stabilisation system. The current booster is required to produce enough current to drive the low resistance (34 ohm) thermo-resistive phase shifting element. The current booster is required to provide sufficient electrical power to the phase shifting element at higher voltages, since the DAQ card saturates at 30 mA. All electronic circuits used in this section can be derived from [95].

Calibration The variable parameters that are included in the DAQ card of the stabilisation system are: SP; averaged sample length; sampling rate; threshold voltages (min and max); proportional, integral and derivative gain coefficients. The system responded better with a relatively low averaging sample length of 50 (i.e. it shows a faster real time response). The sampling rate was best kept at its maximum, which for this card was 48k samples per second. The CO was allowed to vary between the threshold voltages

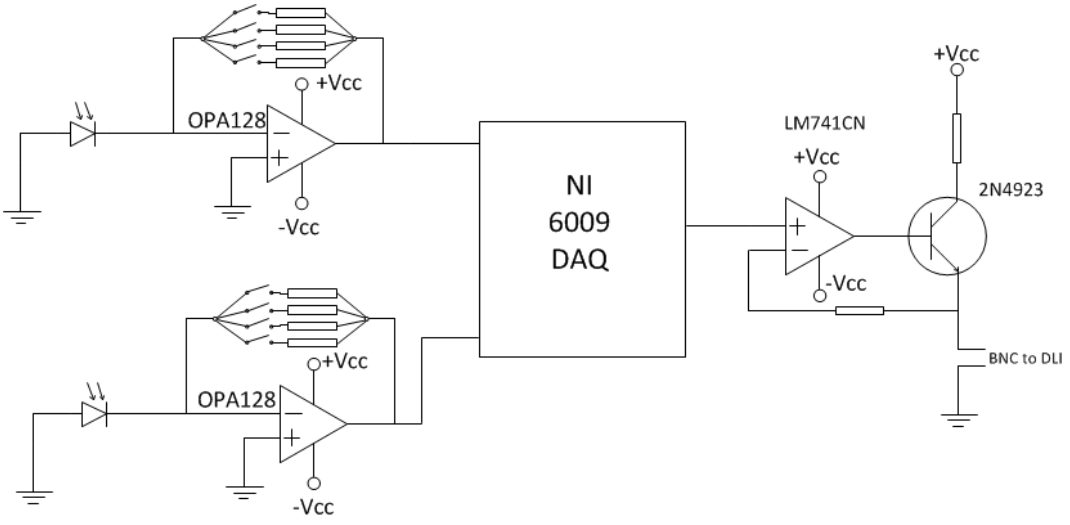

FIGURE A.1: Detailed electronic components in the DLI stabilisation system.

of 0V (due to the limitations of the card itself) and 3.5V (so as to ensure that it operated within safe limits for the thermoresistor). To initially set the SP value a manual DC bias voltage was used to optimise the QPSK signal. The relating ΔPV term was displayed on the worktop screen in Labview, this value was copied into the SP of the system, then the feedback system was used. The system searches for this ΔPV value to achieve a stable QPSK signal. If there was a fluctuation in the system the CO may need to change the driving voltage of the phase shifter to compensate and ensure the same ΔPV value and hence the same stable constellation diagram. Due to the slow effects of thermal drift this system only needs proportional feedback control as the DLI has inherent stability up to tens of minutes. The proportional coefficient was selected to be 0.01, this ensures a fast enough response to temperature/vibrations but a slow enough response to mitigate ringing.

Appendix B

Wavelength converting, idler free phase quantiser

This appendix reports the experimental set-up and the steps that were carried out to measurement the signal phase transfer functions of the wavelength converting, idler free phase quantiser, discussed in Chapter 5. To measure the signal phase an independent phase reference needs to be considered. For this case one of the pumps phases (P2, which was spectrally closer to the signal) was considered as the reference phase, as its power was much higher that the test signal and, thus, it remained unaffected as the single phase was changed for the measurements (this was also confirmed through simulation). In order to measure the phase difference between the signal and the reference line (P2), all the spectral lines at the output of the HNLF were fed into a programmable filter (PF-B in Fig B.1) to remove all spectral lines apart from the signal to be measured, (S_{out}), and P2. A phase shift, ζ, was applied to P2 using PF-B and coherently added these two lines using a second MZM (MZM-B), which was overdriven by the same 40 GHz sinusoidal waveform as used for MZM-A (used to previously generate the frequency comb, cfr. Fig. 5.22 in Chapter 5), as illustrated in Fig. 5.22. The two optical combs generated by the signal and the pump overlap due to their frequency spacing matching the frequency difference between the input lines. By measuring the intensity of one of these mixed lines and applying successive phase shifts of to the pump line using PF-B, a time sequential, balanced coherent detector, may be formed, where the role of the local oscillator is taken by P2. Measurements of the intensity of the selected line are made for each of the following four discrete (0, $pi/2$, pi, $3pi/2$) phase shift. Each power reading can be used in the equation displayed in Eqs. B.1 - B.4) (taken from [10]) to calculate the signal phase. This process was repeated sixty times per experimental measurement.

With the phase offsets (applied to Pump 2)

$$\zeta = (0, \pi/2, \pi, 3\pi/2) \tag{B.1}$$

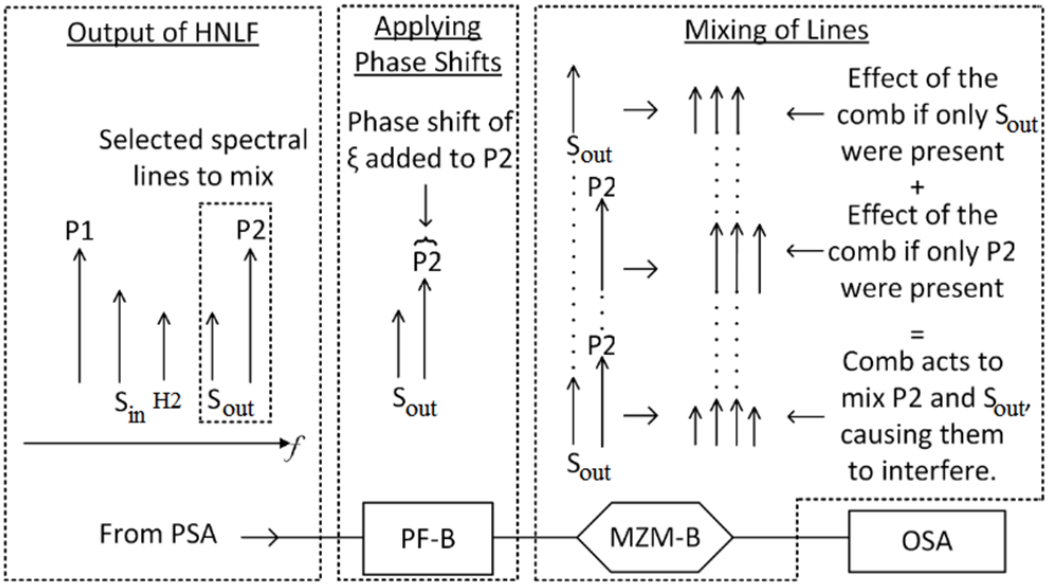

FIGURE B.1: Phase measurement setup, adapted from [10]

The power of the coherent interfered signal-pump field can be shown as:

$$P_\zeta = \left|\eta_s E_s e^{i\omega t+\phi_s} + \eta_p E_p e^{i\omega t+\zeta}\right|^2 \tag{B.2}$$

Expanding, and applying each value of ζ yields

$$\begin{aligned} P_{\zeta=0} &= \eta_s^2 E_s^2 + 2\eta_s\eta_p\sqrt{E_s E_p}\cos\phi_s \\ P_{\zeta=\pi/2} &= \eta_s^2 E_s^2 + 2\eta_s\eta_p\sqrt{E_s E_p}\sin\phi_s \\ P_{\zeta=\pi} &= \eta_s^2 E_s^2 - 2\eta_s\eta_p\sqrt{E_s E_p}\cos\phi_s \\ P_{\zeta=3\pi/2} &= \eta_s^2 E_s^2 - 2\eta_s\eta_p\sqrt{E_s E_p}\sin\phi_s \end{aligned} \tag{B.3}$$

Using the above equations a relationship can be obtained for ϕ_s

$$\phi_s = \arctan\left(\frac{P_{\zeta=\pi/2} - P_{\zeta=3\pi/2}}{P_{\zeta=0} - P_{\zeta=\pi}}\right) \tag{B.4}$$

List of Publications

B.1 Journal articles

(1) L. Jones, F. Parmigiani, P. Petropoulos and D. J. Richardson "Phase regeneration of an M-PSK signal using partial regeneration of its M/2-PSK second phase harmonic" Optics Communications 2014 Vol.334(1) pp.35-40 .

(2) M.A.Ettabib, K.Hammani, F.Parmigiani, L.Jones, A.Kapsalis, A.Bogris, D.Syvridis, M.Brun, P.Labeye, S.Nicoletti, P.Petropoulos "FWM-based wavelength conversion of 40 Gbaud PSK signals in a silicon germanium waveguide" Optics Express 2013 Vol.21(14) pp.16683-16689

(3) F.Parmigiani, L.Jones, J.Kakande, P.Petropoulos, D.J.Richardson "Modulation format conversion employing coherent optical superposition" Optics Express 2012 Vol.20(26) pp.B322-B330

(4) M.A.Ettabib, F.Parmigiani, X.Feng, L.Jones, J.Kakande, R.Slavik, F.Poletti, G.M.Ponzo, J.D.Shi, M.N.Petrovich, W.H.Loh, P.Petropoulos, D.J.Richardson "Phase regeneration of DPSK signals in a highly nonlinear lead-silicate W-type fiber" Optics Express 2012 Vol.20(24) pp.27419-27424

(5) M.A.Ettabib, L.Jones, J.Kakande, R.Slavk, F.Parmigiani, X.Feng, F.Poletti, G.M.Ponzo, J.D.Shi, M.N.Petrovich, W.H.Loh, P.Petropoulos, D.J.Richardson "Phase sensitive amplification in a highly nonlinear lead-silicate fiber" Optics Express 2012 Vol.20(2) pp.1629-1634

B.2 Conference Submissions

(1) K.R.H.Bottrill, F.Parmigiani, L.Jones, G.Hesketh, D.J.Richardson, P.Petropoulos "Phase and amplitude regeneration through sequential PSA and FWM saturation in HNLF" ECOC 2015 Valencia, Spain 27 Sep - 1 Oct 2015

(2) K.Bottrill, L.Jones, F.Parmigiani, D.J.Richardson, P.Petropoulos "FWM-based, idler-free phase quantiser with flexible operating power" OFC 2015 Los Angeles 22-26 Mar 2015

(3) L.Jones, F.Parmigiani, V.J.F.Rancao, M.A.Ettabib, P.Petropoulos and D.J.Richardson "Transmission performance of phase-preserving amplitude regenerator based on optical injection locking," OFC '13, Anaheim, USA, 19–21 March 2013.

(4) M.A.Ettabib, F.Parmigiani, X.Feng, L.Jones, J.Kakande, R.Slavik, F.Poletti, G.M.Ponzo, J.D.Shi, M.N.Petrovich, P.Petropoulos, W.H.Loh, D.J.Richardson "All-optical phase regeneration in a highly nonlinear lead-silicate fiber" OSA Nonlinear Photonics '12 Colorado Springs 17-21 Jun 2012

(5) F.Parmigiani, J.Kakande, L.M.Jones, P.Petropoulos, D.J.Richardson "Packet compression of complex modulation formats based on coherent optical superposition" International Conference on Transparent Optical Networks (ICTON 2012) Warwick 2-5 Jul 2012

(6) F.Parmigiani, J.Kakande, L.M.Jones, P.Petropoulos, D.J.Richardson "Temporal multiplexing of complex modulation formats facilitated by their coherent optical superposition" European Conference on Optical Communication (ECOC) Amsterdam 16-20 Sept 2012

(7) L.M.Jones, F.Parmigiani, J.Kakande, P.Petropoulos, D.J.Richardson "All-optical broadband phase noise emulation" OSA Nonlinear Photonics '12 Colorado Springs 17-21 Jun 2012

(8) M.A.Ettabib, L.Jones, J.Kakande, R.Slavik, F.Parmigiani, X.Feng, F.Poletti, G.M.Ponzo, J.D.Shi, M.N.Petrovich, P.Petropoulos, W.H.Loh, D.J.Richardson "Phase sensitive amplification in a highly nonlinear lead-silicate fibre" European Conference on Optical Communication (ECOC) Geneva, Switzerland 18-22 Sept 2011

References

[1] H. Takara, "Ultra-large-capacity multi-core fiber transmission technologies," in *Photonics Society Summer Topical Meeting Series, 2013 IEEE* pp. 133–134 (2013).

[2] R. Slavik, F. Parmigiani, J. Kakande, C. Lundstrom, M. Sjodin, P. A. Andrekson, R. Weerasuriya, S. Sygletos, A. D. Ellis, L. Gruner-Nielsen, D. Jakobsen, S. Herstrom, R. Phelan, J. O'Gorman, A. Bogris, D. Syvridis, S. Dasgupta, P. Petropoulos, and D. J. Richardson, "All-optical phase and amplitude regenerator for next-generation telecommunications systems," Nature Photonics **4**, 690–695 (2010).

[3] A. Fragkos, A. Bogris, D. Syvridis, and R. Phelan, "Amplitude Noise Limiting Amplifier for Phase Encoded Signals Using Injection Locking in Semiconductor Lasers," Lightwave Technology, Journal of **30**, 764–771 (2012).

[4] "Agilent N4391A Optical Modulation Analyzer. 2010," .

[5] E. Hecht, *Optics, Fourth Edition* (Addison-Westley, 2002).

[6] "Kylia, Quadrature Amplitude Modulator," http://kylia.com/kylia/wp-content/uploads/2015/02/datasheet-QAM-v2.0.pdf,.

[7] M. A. Ettabib, F. Parmigiani, X. Feng, L. Jones, J. Kakande, R. Slavík, F. Poletti, G. M. Ponzo, J. Shi, M. N. Petrovich, W. H. Loh, P. Petropoulos, and D. J. Richardson, "Phase regeneration of DPSK signals in a highly nonlinear lead-silicate W-type fiber," Opt. Express **20**, 27 419–27 424 (2012).

[8] K. R. Bottrill, L. Jones, F. Parmigiani, D. J. Richardson, and P. Petropoulos, "FWM-based, Idler-free Phase Quantiser with Flexible Operating Power," in *Optical Fiber Communication Conference* p. W4C.3 (2015).

[9] J. Kakande, A. Bogris, R. Slavik, F. Parmigiani, D. Syvridis, P. Petropoulos, and D. Richardson, "First demonstration of all-optical QPSK signal regeneration in a novel multi-format phase sensitive amplifier," in *Optical Communication (ECOC), 2010 36th European Conference and Exhibition on* pp. 1–3 (2010).

[10] K. R. Bottrill, G. D. Hesketh, F. Parmigiani, P. Horak, D. J. Richardson, and P. Petropoulos, "Suppression of Gain Variation in a PSA-Based Phase Regenerator Using an Additional Harmonic," Photonics Technology Letters, IEEE **26**, 2074–2077 (2014).

[11] "BBC, "Four in Five Regard Internet Access as a Fundamental Right: Global Poll," 2010." http://news.bbc.co.uk/1/hi/technology/8548190.stm,.

[12] S. Namiki, T. Kurosu, K. Tanizawa, J. Kurumida, T. Hasama, H. Ishikawa, T. Nakatogawa, M. Nakamura, and K. Oyamada, "Ultrahigh-Definition Video Transmission and Extremely Green Optical Networks for Future," Selected Topics in Quantum Electronics, IEEE Journal of **17**, 446–457 (2011).

[13] W. Gambling, "The rise and rise of optical fibers," Selected Topics in Quantum Electronics, IEEE Journal of **6**, 1084–1093 (2000).

[14] P. A. Franken, A. E. Hill, C. W. Peters, and G. Weinreich, "Generation of Optical Harmonics," Phys. Rev. Lett. **7**, 118–119 (1961).

[15] G.P.Agrawal, *Nonlinear Fiber Optics, Third Edition* (Academic Press, 2001).

[16] I. Hayashi, M. B. Panish, P. W. Foy, and S. Sumski, "Junction Lasers Which Operate Continuously At Room Temperature," Applied Physics Letters **17** (1970).

[17] E. Snitzer, "Cylindrical Dielectric Waveguide Modes∗," J. Opt. Soc. Am. **51**, 491–498 (1961).

[18] K. Kao and G. Hockham, "Dielectric-fibre surface waveguides for optical frequencies," Electrical Engineers, Proceedings of the Institution of **113**, 1151–1158 (1966).

[19] F. P. Kapron, D. B. Keck, and R. D. Maurer, "Radiation Losses In Glass Optical Waveguides," Applied Physics Letters **17** (1970).

[20] I. P. Kaminow, T. Li, and A. E. Willner, *Optical fibre telecommunications B: Systems and networks, Fifth Edition* (Academic Press, 2008).

[21] B. Puttnam, R. Luis, and W. e. a. Klaus, "2.15 Pb/s Transmission using a 22 Core Homogeneous Single-Mode Multi-Core Fiber and Wideband Optical Comb," in *ECOC 2015 Valencia* (2015).

[22] D. J. Richardson, "Filling the Light Pipe," Science **330**, 327–328 (2010).

[23] J. Sinsky and P. Winzer, "100-Gb/s optical communications," IEEE Microwave Magazine **10**, 44 – 57 (2009).

[24] J. Kakande, A. Bogris, R. Slavik, F. Parmigiani, D. Syvridis, M. Skold, M. Westlund, P. Petropoulos, and D. Richardson, "QPSK phase and amplitude regeneration at 56 Gbaud in a novel idler-free non-degenerate phase sensitive amplifier," in *Optical Fiber Communication Conference and Exposition (OFC/NFOEC), 2011 and the National Fiber Optic Engineers Conference* pp. 1–3 (2011).

[25] G. Hesketh and P. Horak, "Reducing bit-error rate with optical phase regeneration in multilevel modulation formats," Opt. Lett. **38**, 5357–5360 (2013).

[26] Z. Tong, C. Lundstrm, P. A. Andrekson, C. J. McKinstrie, M. Karlsson, D. J. Blessing, E. Tipsuwannakul, B. J. Puttnam, H. Toda, and L. Grüner-Nielsen, "Towards ultrasensitive optical links enabled by low-noise phase-sensitive amplifiers," Nature Photonics **5**, 430–436 (2011).

[27] F. Parmigiani, L. Jones, J. Kakande, P. Petropoulos, and D. J. Richardson, "Modulation format conversion employing coherent optical superposition," Opt. Express **20**, B322–B330 (2012).

[28] L. Jones, F. Parmigiani, J. Kakande, P. Petropoulos, and D. J. Richardson, "All-Optical broadband phase noise emulation," in *Advanced Photonics Congress* p. JM5A.19 (2012).

[29] L. Jones, F. Parmigiani, V. Rancano, M. Ettabib, P. Petropoulos, and D. Richardson, "Transmission performance of phase-preserving amplitude regenerator based on optical injection locking," in *Optical Fiber Communication Conference and Exposition and the National Fiber Optic Engineers Conference (OFC/NFOEC), 2013* pp. 1–3 (2013).

[30] L. Jones, F. Parmigiani, P. Petropoulos, and D. J. Richardson, "Phase regeneration of an M-PSK signal using partial regeneration of its M/2-PSK second phase harmonic," Optics Communications **334**, 35 – 40 (2015).

[31] "Corning SMF-28e Optical Fiber Product Information," . https://www.corning.com/media/worldwide/coc/documents/Fiber/SMF-28

[32] L. Cohen, W. Mammel, and S. Jang, "Low-loss quadruple-clad single-mode lightguides with dispersion below 2 ps/km nm over the 1.28 um-1.65 um wavelength range," Electronics Letters **18**, 1023–1024 (1982).

[33] "Corning. 2002, "Corning Single Mode Optical Fibre"," . http://www.princetel.com/datasheets/SMF28e.pdf

[34] G. Ning, P. Shum, H. Dong, M. Tang, and S. Aditya, "PMD effect on pulse shapes and power penalty in optical communication systems," in *Communications, Circuits and Systems, 2005. Proceedings. 2005 International Conference on* **1**, 571–574 Vol. 1 (2005).

[35] A. Carter and B. Samson, "Panda-style fibers move beyond telecom," http://connection.ebscohost.com/c/articles/14158924/panda-style-fibers-move-beyond-telecom,.

[36] R. Thompson and F. Akers, "Polarization maintaining single-mode fibers," Quantum Electronics, IEEE Journal of **17**, 2382–2384 (1981).

[37] D. Cotter, R. Manning, K. Blow, and A. Ellis, "Nonlinear Optics for High-Speed Digital Information Processing," Science **286**, 1523–1528 (1999).

[38] B. E. Olsson and D. Blumenthal, "All-optical demultiplexing using fiber cross-phase modulation (XPM) and optical filtering," Photonics Technology Letters, IEEE **13**, 875–877 (2001).

[39] X. Tang, S. H. Chung, A. Karar, J. Cartledge, A. Shen, and G.-H. Duan, "Spectral Filtering Characteristics of a Quantum-Dash Fabry-Perot Laser and Its Implications on 40 Gb/s XPM Based Optical Retiming Performance," Lightwave Technology, Journal of **29**, 31–36 (2011).

[40] R. Tang, J. Lasri, P. S. Devgan, V. Grigoryan, P. Kumar, and M. Vasilyev, "Gain characteristics of a frequency nondegenerate phase-sensitive fiber-optic parametric amplifier with phase self-stabilized input," Opt. Express **13**, 10 483–10 493 (2005).

[41] R. Tang, P. S. Devgan, V. S. Grigoryan, P. Kumar, and M. Vasilyev, "In-line phase-sensitive amplification of multi-channel CW signals based on frequency nondegenerate four-wave-mixing in fiber," Opt. Express **16**, 9046–9053 (2008).

[42] M. E. Marhic, *Fiber Optical Parametric Amplifiers, Oscillators and Related Devices: Theory, Applications, and Related Devices* (Cambridge University Press, 2008).

[43] C. J. McKinstrie and S. Radic, "Phase-sensitive amplification in a fiber," Opt. Express **12**, 4973–4979 (2004).
http://www.opticsexpress.org/abstract.cfm?URI=oe-12-20-4973

[44] R. H. Stolen, W. J. Tomlinson, H. A. Haus, and J. P. Gordon, "Raman response function of silica-core fibers," J. Opt. Soc. Am. B **6**, 1159–1166 (1989).

[45] J. M. C. Boggio, J. D. Marconi, and H. L. Fragnito, "Experimental and Numerical Investigation of the SBS-Threshold Increase in an Optical Fiber by Applying Strain Distributions," J. Lightwave Technol. **23**, 3808 (2005).

[46] W. Steier and H. Stover, "Locking of laser oscillators by light injection," Quantum Electronics, IEEE Journal of **2**, 111–112 (1966).

[47] J. P. Gordon and L. F. Mollenauer, "Phase noise in photonic communications systems using linear amplifiers," Opt. Lett. **15**, 1351–1353 (1990).

[48] P. Mamyshev, "All-optical data regeneration based on self-phase modulation effect," in *Optical Communication, 1998. 24th European Conference on* **1**, 475–476 vol.1 (1998).

[49] L. Bramerie, Q. T. Le, M. Gay, A. O'Hare, S. Lobo, M. Joindot, J. C. Simon, H.-T. Nguyen, and J.-L. Oudar, "All-Optical 2R Regeneration With a Vertical Microcavity-Based Saturable Absorber," Selected Topics in Quantum Electronics, IEEE Journal of **18**, 870–883 (2012).

[50] M. Sorokina, S. Sygletos, A. Ellis, and S. Turitsyn, "Regenerative Fourier transformation for dual-quadrature regeneration of multilevel rectangular QAM," Opt. Lett. **40**, 3117–3120 (2015).

[51] T. Umeki, M. Asobe, H. Takara, Y. Miyamoto, and H. Takenouchi, "Multi-span transmission using phase and amplitude regeneration in PPLN-based PSA," Opt. Express **21**, 18 170–18 177 (2013).

[52] K. Croussore, I. Kim, C. Kim, Y. Han, and G. Li, "Phase-and-amplitude regeneration of differential phase-shift keyed signals using a phase-sensitive amplifier," Opt. Express **14**, 2085–2094 (2006).

[53] T. Roethlingshoefer, G. Onishchukov, B. Schmauss, and G. Leuchs, "All-Optical Simultaneous Multilevel Amplitude and Phase Regeneration," Photonics Technology Letters, IEEE **26**, 556–559 (2014).

[54] F. Parmigiani, K. Bottrill, R. Slavík, D. J. Richardson, and P. Petropoulos, "PSA-based all-optical multi-channel phase regenerator," in *ECOC '15 Valencia* pp. 1–3 (2015).

[55] P. Guan, K. M. Roge, N. K. Kjoller, H. C. H. Mulvad, H. Hu, M. Galili, T. Morioka, and L. K. Oxenlowe, "All-optical WDM Regeneration of DPSK Signals using Optical Fourier Transformation and Phase Sensitive Amplification," in *ECOC '15 Valencia* (2015).

[56] M. Matsumoto, "Fiber-Based All-Optical Signal Regeneration," Selected Topics in Quantum Electronics, IEEE Journal of **18**, 738–752 (2012).

[57] M. Sorokina, "Design of multilevel amplitude regenerative system," Opt. Lett. **39**, 2499–2502 (2014).

[58] K. Croussore and G. Li, "Phase and Amplitude Regeneration of Differential Phase-Shift Keyed Signals Using Phase-Sensitive Amplification," Selected Topics in Quantum Electronics, IEEE Journal of **14**, 648–658 (2008).

[59] K. Croussore and G. Li, "Amplitude regeneration of RZ-DPSK signals based on four-wave mixing in fibre," Electronics Letters **43**, 177–178 (2007).

[60] S. Zhang and J. C. Cartledge, "A DSP-Based Control Method For a Nonlinear Mach x2013;Zehnder Interferometer DPSK Regenerator," Journal of Lightwave Technology **33**, 3788–3795 (2015).

[61] A. Ellis and S. Sygletos, "Phase sensitive signal processing using semiconductor optical amplifiers," in *Optical Fiber Communication Conference and Exposition and the National Fiber Optic Engineers Conference (OFC/NFOEC), 2013* pp. 1–3 (2013).

[62] T. Umeki, M. Asobe, H. Takara, T. Kobayashi, H. Kubota, H. Takenouchi, and Y. Miyamoto, "First demonstration of multi-span transmission using phase and amplitude regeneration in PPLN-based PSA," in *Optical Fiber Communication Conference and Exposition and the National Fiber Optic Engineers Conference (OFC/NFOEC), 2013* pp. 1–3 (2013).

[63] L. C. Christen, S. R. Nuccio, Y. K. Lize, N. Jayachandran, A. E. Willner, and L. Paraschais, "Stabilization of a 40 Gb/s DPSK Delay-Line Interferometer Using Half Bit-Rate AM Pilot Tone Monitoring," in *Conference on Lasers and Electro-Optics/Quantum Electronics and Laser Science Conference and Photonic Applications Systems Technologies* p. CMJJ2 (2007).

[64] A. Demir, "Nonlinear Phase Noise in Optical-Fiber-Communication Systems," Journal of Lightwave Technology, **25**, 2002–2032 (2007).

[65] Q. T. Le, L. Bramerie, H.-T. Nguyen, M. Gay, S. Lobo, M. Joindot, J.-L. Oudar, and J. C. Simon, "Saturable-Absorber-Based Phase-Preserving Amplitude Regeneration of RZ DPSK Signals," Photonics Technology Letters, IEEE **22**, 887–889 (2010).

[66] P. Frascella, S. Sygletos, F. C. G. Gunning, R. Weerasuriya, L. Gruner-Nielsen, R. Phelan, J. O'Gorman, and A. D. Ellis, "DPSK Signal Regeneration With a Dual-Pump Nondegenerate Phase-Sensitive Amplifier," Photonics Technology Letters, IEEE **23**, 516–518 (2011).

[67] A. Mussot, M. L. Parquier, B. Berrier, M. Perard, and P. Szriftgiser, "All-optical {SBS} reduction in fiber optic parametric amplifiers," Optics Communications **282**, 988 – 991 (2009).

[68] M. Matsumoto, "Performance improvement of phase-shift-keying signal transmission by means of optical limiters using four-wave mixing in fibers," Lightwave Technology, Journal of **23**, 2696–2701 (2005).

[69] A. Bogris and D. Syvridis, "All-optical signal processing for 16-QAM using four-level optical phase quantizers based on phase sensitive amplifiers," in *Optical Communication (ECOC 2013), 39th European Conference and Exhibition on* pp. 1–3 (2013).

[70] K. Cvecek, K. Sponsel, C. Stephan, G. Onishchukov, R. Ludwig, C. Schubert, B. Schmauss, and G. Leuchs, "Phase-preserving amplitude regeneration for a WDM RZ-DPSK signal using a nonlinear amplifying loop mirror," Opt. Express **16**, 1923–1928 (2008).

[71] M. Hierold, T. Roethlingshoefer, K. Sponsel, G. Onishchukov, B. Schmauss, and G. Leuchs, "Multilevel Phase-Preserving Amplitude Regeneration Using a Single Nonlinear Amplifying Loop Mirror," Photonics Technology Letters, IEEE **23**, 1007–1009 (2011).

[72] T. I. Lakoba, J. R. Williams, and M. Vasilyev, "Low-power, phase-preserving 2R amplitude regenerator," Optics Communications **285**, 331 – 337 (2012).

[73] J. Kakande, F. Parmigiani, R. Slavik, L. Gruner-Nielsen, D. Jakobsen, S. Herstrom, P. Petropoulos, and D. Richardson, "Saturation effects in degenerate phase sensitive fiber optic parametric amplifiers," in *Optical Communication (ECOC), 2010 36th European Conference and Exhibition on* pp. 1–3 (2010).

[74] Y. Chen and A. W. Snyder, "Four-photon parametric mixing in optical fibers: effect of pump depletion," Opt. Lett. **14**, 87–89 (1989).

[75] J. Kakande, R. Slavík, F. Parmigiani, A. Bogris, D. Syvridis, P. Petropoulos, and D. Richardson, "Multilevel quantization of optical phase in a novel coherent parametric mixer architecture," Nature Photonics **5**, 748–752 (2011).

[76] M. Asobe, T. Umeki, H. Takenouchi, and Y. Miyamoto, "In-line phase-sensitive amplification of QPSK signal using multiple quasi-phase matched LiNbO3 waveguide," Opt. Express **22**, 26 642–26 650 (2014).

[77] J. Kakande, R. Slavík, F. Parmigiani, P. Petropoulos, and D. Richardson, "All-Optical Processing of Multi-level Phase Shift Keyed Signals," in *Optical Fiber Communication Conference* p. OW1I.3 (2012).

[78] G.P.Agrawal, *Applications of Nonlinear Fiber Optics* (Academic Press, 2001).

[79] D. Mazroa, B. Puttnam, A. Szabo, S. Shinada, and N. Wada, "PPLN-based all-optical QPSK regenerator," in *Transparent Optical Networks (ICTON), 2013 15th International Conference on* pp. 1–4 (2013).

[80] R. P. Webb, J. M. Dailey, R. J. Manning, and A. D. Ellis, "Phase discrimination and simultaneous frequency conversion of the orthogonal components of an optical signal by four-wave mixing in an SOA," Opt. Express **19**, 20 015–20 022 (2011).

[81] K. R. H. Bottrill, R. Kakarla, F. Parmigiani, D. Venkitesh, and P. Petropoulos, "Phase Regeneration of QPSK Signal in SOA Using Single-Stage, Wavelength Converting PSA," IEEE Photonics Technology Letters **28**, 205–208 (2016).

[82] G.-W. Lu, E. Tipsuwannakul, T. Miyazaki, C. Lundstrom, M. Karlsson, and P. Andrekson, "Format Conversion of Optical Multilevel Signals Using FWM-Based Optical Phase Erasure," Lightwave Technology, Journal of **29**, 2460–2466 (2011).

[83] K. R. Bottrill, G. D. Hesketh, F. Parmigiani, P. Horak, D. J. Richardson, and P. Petropoulos, "An Optical Phase Quantiser Exhibiting Suppressed Phase Dependent Gain Variation," in *Optical Fiber Communication Conference* p. W3F.7 (2014).

[84] K. Bottrill, F. Parmigiani, L. Jones, G. Hesketh, D. J. Richardson, and P. Petropoulos, "Phase and Amplitude Regeneration through Sequential PSA and FWM Saturation in HNLF," in *ECOC 2015 Valencia, Spain* pp. 1–3 (2015).

[85] J. Leuthold, C. Koos, and W. Freude, "Nonlinear silicon photonics," Nature Photonics **4**, 535–544 (2010).

[86] M. Ettabib, F. Parmigiani, A. Kapsalis, A. Bogris, M. Brun, P. Labeye, S. Nicoletti, K. Hammani, D. Syvridis, D. Richardson, and P. Petropoulos, "Record phase sensitive extinction ratio in a silicon germanium waveguide," in *Lasers and Electro-Optics (CLEO), 2015 Conference on* pp. 1–2 (2015).

[87] F. Da-Ros, D. Vukovic, A. Gajda, K. Dalgaard, L. Zimmermann, B. Tillack, M. Galili, K. Petermann, and C. Peucheret, "Phase regeneration of DPSK signals in a silicon waveguide with reverse-biased p-i-n junction," Opt. Express **22**, 5029–5036 (2014).

[88] M. Ettabib, K. Bottrill, F. Parmigiani, A. Kapsalis, A. Bogris, M. Brun, P. Labeye, S. Nicoletti, K. Hammani, D. Syvridis, D. J. Richardson, and P. Petropoulos, "PSA-based Phase Regeneration of DPSK Signals in a Silicon Germanium Waveguide," in *ECOC 2015* (2015).

[89] S. Sygletos, P. Frascella, S. K. Ibrahim, L. Grüner-Nielsen, R. Phelan, J. O'Gorman, and A. D. Ellis, "A practical phase sensitive amplification scheme for two channel phase regeneration," Opt. Express **19**, B938–B945 (2011).

[90] S. Sygletos, P. Frascella, F. Gunning, and A. D. Ellis, "Multi-wavelength regeneration of phase encoded signals based on phase sensitive amplifiers," in *Transparent Optical Networks (ICTON), 2012 14th International Conference on* pp. 1–4 (2012).

[91] M. A. Sorokina, S. Sygletos, and S. K. Turitsyn, "Optimization of cascaded regenerative links based on phase sensitive amplifiers," Opt. Lett. **38**, 4378–4381 (2013).

[92] A. Bogris, "All-optical demultiplexing of 16-QAM signals into QPSK tributaries using four-level optical phase quantizers," Opt. Lett. **39**, 1775–1778 (2014).

[93] A. Bogris, "Optical phase processor with enhanced phase quantization properties for higher order modulation formats relying on phase sensitive amplification and limiting amplifiers," in *2015 European Conference on Lasers and Electro-Optics - European Quantum Electronics Conference* p. 13 (2015).

[94] R. S. Tucker and K. Hinton, "Energy Consumption and Energy Density in Optical and Electronic Signal Processing," IEEE Photonics Journal **3**, 820–833 (2011).

[95] O. Bishop, *Electronic: Circuits and Systems, Fourth Edition* (Routledge, 2011).